



THE UNIVERSITY *of* EDINBURGH

Edinburgh Research Explorer

A WDR35-dependent coat protein complex transports ciliary membrane cargo vesicles to cilia

Citation for published version:

Quidwai, T, Wang, J, Hall, EA, Petriman, NA, Leng, W, Kiesel, P, Wells, JN, Murphy, LC, Keighren, MA, A Marsh, J, Lorentzen, E, Pigino, G & Mill, P 2021, 'A WDR35-dependent coat protein complex transports ciliary membrane cargo vesicles to cilia', *eLIFE*, vol. 10. <https://doi.org/10.7554/eLife.69786>

Digital Object Identifier (DOI):

[10.7554/eLife.69786](https://doi.org/10.7554/eLife.69786)

Link:

[Link to publication record in Edinburgh Research Explorer](#)

Document Version:

Peer reviewed version

Published In:

eLIFE

Publisher Rights Statement:

This article is distributed under the terms of the Creative Commons Attribution License permitting unrestricted use and redistribution provided that the original author and source are credited.

General rights

Copyright for the publications made accessible via the Edinburgh Research Explorer is retained by the author(s) and / or other copyright owners and it is a condition of accessing these publications that users recognise and abide by the legal requirements associated with these rights.

Take down policy

The University of Edinburgh has made every reasonable effort to ensure that Edinburgh Research Explorer content complies with UK legislation. If you believe that the public display of this file breaches copyright please contact openaccess@ed.ac.uk providing details, and we will remove access to the work immediately and investigate your claim.



1 **A WDR35-dependent coat protein complex**
2 **transports ciliary membrane cargo vesicles to cilia**

3 **Tooba Quidwai¹, Jiaolong Wang², Emma A. Hall¹, Narcis Adrian Petriman²,**
4 **Weihua Leng³, Petra Kiesel³, Jonathan N. Wells¹, Laura Murphy¹, Margaret A.**
5 **Keighren¹, Joseph A. Marsh¹, Esben Lorentzen², Gaia Pigo^{3,4} and Pleasantine**
6 **Mill^{1*}**

7 ¹ MRC Human Genetics Unit, Institute of Genetics and Cancer, University of Edinburgh,
8 Edinburgh EH4 2XU, UK

9 ² Department of Molecular Biology and Genetics, Aarhus University, Gustav Wieds Vej 10c,
10 DK-8000 Aarhus C, Denmark

11 ³ Max Planck Institute of Molecular Cell Biology and Genetics, Pfotenhauerstraße 108, 01307
12 Dresden, Germany

13 ⁴ Human Technopole, Viale Rita Levi-Montalcini, 1, 20157 Milano MI, Italy

14 *For correspondence: pleasantine.mill@ed.ac.uk

15 **Running title: IFTA-dependent coat complex for transport into cilia**
16

17 **[Keywords:** cilia; intraflagellar transport (IFT); ciliary pocket; vesicular traffic; COPI;
18 coatomer; transmission electron microscopy (TEM); correlative light and electron
19 microscopy (CLEM); membrane cargos]

20

21 **Impact statement:** Electron-tomography and biochemical approaches demonstrate a
22 direct role for WDR35, beyond integrity of the IFT-A holocomplex, in formation and fusion of
23 electron-dense coated vesicles to the ciliary sheath and pocket for delivery of cargos
24 necessary for axoneme elongation.

25 **Abstract**

26 Intraflagellar transport (IFT) is a highly conserved mechanism for motor-driven transport of
27 cargo within cilia, but how this cargo is selectively transported to cilia is unclear.
28 WDR35/IFT121 is a component of the IFT-A complex best known for its role in ciliary
29 retrograde transport. In the absence of WDR35, small mutant cilia form but fail to enrich in
30 diverse classes of ciliary membrane proteins. In *Wdr35* mouse mutants, the non-core IFT-A
31 components are degraded and core components accumulate at the ciliary base. We reveal
32 deep sequence homology of WDR35 and other IFT-A subunits to α and β' COPI coatomer
33 subunits, and demonstrate an accumulation of 'coat-less' vesicles which fail to fuse
34 with *Wdr35* mutant cilia. We determine that recombinant non-core IFT-As can bind directly
35 to lipids and provide the first *in-situ* evidence of a novel coat function for WDR35, likely with
36 other IFT-A proteins, in delivering ciliary membrane cargo necessary for cilia elongation.

37

38 Introduction

39

40 The primary cilium is a highly specialized sensory organelle and signaling hub
41 compartmentalized from the rest of the cell and positioned with a unique interface towards
42 the extracellular environment. Analogous to a cell's antenna, many roles for cilia have
43 emerged in development, disease and homeostasis (Reiter and Leroux, 2017). Enrichment of
44 signaling receptors and effectors in ciliary membranes is critical for cilia function, yet all
45 biosynthesis of cilia-localised membrane proteins occurs in the endoplasmic reticulum and is
46 sorted by the Golgi and vesicular membrane traffic system to efficiently route cargo-laden
47 vesicles for incorporation into the elongating ciliary membrane. The details of this highly
48 efficient, directed transport process for the delivery of diverse cargos to cilia remains unclear.

49 In mammalian cells, electron microscopy (EM) studies reveal the Golgi stacks closely
50 apposed to the mother centriole (Sorokin, 1962; Wheatley, 1969). During intracellular
51 ciliogenesis, small vesicles are recruited, most likely from the Golgi, to the mother centriole,
52 where they fuse to form a large preciliary vesicle (PCV) attached at the distal appendages
53 (Yee and Reiter, 2015). More secondary vesicles later fuse with the PCV, allowing elongation
54 of cilia. Interestingly, the Golgi remains close to mature cilia, suggesting a continuous
55 exchange of materials, enabling cilia maintenance (Sorokin, 1962; Wheatley, 1969). Several
56 proteins essential for ciliogenesis localize to both the Golgi and the mother centriole and are
57 implicated in this early stage of ciliogenesis including CCDC41 (CEP83), IFT20, HOOK2, and
58 CEP164 (Baron Gaillard et al., 2011; Follit et al., 2006; Graser et al., 2007; Joo et al., 2013;
59 Schmidt et al., 2012; Tanos et al., 2013). In some cases, including HOOK2 and CEP164, these
60 components recruit Rab8a and Rabin-8, which facilitate membrane transport to cilia (Baron
61 Gaillard et al., 2011; Moritz et al., 2001; Nachury et al., 2007). For some specific ciliary cargos,
62 including rhodopsin (Wang and Deretic, 2014) and PKD2 (Follit et al., 2008, 2006; Hoffmeister
63 et al., 2011; Kim et al., 2014; Noda et al., 2016), Golgi-to-cilia transport mechanisms have
64 been described. However, these processes seem to involve cargo-specific traffic modules. A
65 more universal Golgi-to-cilia transport machinery, if one exists, has yet to be identified.

66 In contrast to traffic to cilia, movement of cargos within cilia requires highly
67 conserved motor-driven macromolecular cargo binding complexes that traffic along
68 axonemal microtubules closely apposed against the ciliary membrane, in a process known as
69 intraflagellar transport (IFT) (Cole, 2009; Kozminski et al., 1993; Pazour et al., 1998; Pigino et
70 al., 2009; Rogowski et al., 2013; Rosenbaum and Witman, 2002). Bidirectional movement of

71 IFT complexes regulates cilia content; the IFT-B complex aids in kinesin-dependent
72 anterograde transport of cargo, whilst the IFT-A complex is required for retrograde transport
73 driven by dynein motors (Blacque et al., 2006; Efimenko et al., 2006; Jonassen et al., 2012;
74 Lee et al., 2008; Piperno et al., 1998; Tran et al., 2008; Tsao and Gorovsky, 2008). The IFT-A
75 complex is composed of three core (IFT144/WDR19, IFT140/WDR35, IFT122/WDR10) and
76 three non-core proteins (IFT139/TTC21B/THM1, IFT121/WDR35, and IFT43)(Behal et al.,
77 2012; Hirano et al., 2017; Piperno et al., 1998). However, beyond classical retrograde ciliary
78 traffic defects (an inappropriate accumulation of cargos within the cilium) mutations in
79 *IFT144*, *IFT140*, *IFT122*, *IFT121/WDR35*, and *IFT43* result in either severe reduction in cilia
80 length or complete loss of cilia, implying they also have critical roles in transport of cargo to
81 cilia (Avidor-Reiss et al., 2004; Caparrós-Martín et al., 2015; Duran et al., 2017; Hirano et al.,
82 2017; Liem et al., 2012; Mill et al., 2011; Takahara et al., 2018; Zhu et al., 2017). Indeed,
83 several IFT-A mutants fail to localize a range of ciliary membrane proteins including EVC1/2,
84 SMO, ARL13B, INPP5E, and SSTR3 to cilia (Brear et al., 2014; Caparrós-Martín et al., 2015; Fu
85 et al., 2016; Hirano et al., 2017; Jensen et al., 2010; Lee et al., 2008; Liem et al., 2012;
86 Mukhopadhyay et al., 2010; Takahara et al., 2018). However, the mechanism of transport
87 and the location of any IFT-A extra-ciliary function remains unclear.

88 The movement of cargos between membranes of spatially separated organelles in the
89 cytoplasm involves vesicular traffic. Indeed, IFT proteins have been observed to localize to
90 various endomembranes and vesicular compartments outside cilia. For example, the IFT-B
91 protein IFT20 localizes to the Golgi (Follit et al., 2006; Noda et al., 2016), whereas both IFT-B
92 (IFT20, IFT27, IFT46, IFT52, IFT57, IFT88 and IFT172) and IFT-A proteins (IFT139, IFT140)
93 cluster around periciliary vesicles, shown by immuno-EM and light microscopy (Sedmak and
94 Wolfrum, 2010; Wood et al., 2012; Wood and Rosenbaum, 2014). Direct interaction of IFTs
95 with membranes *in vitro* has also been described where the adaptor TULP3 and
96 phosphoinositides mediate the membrane association of IFT-As (Mukhopadhyay et al., 2010).
97 More recently, purified IFT172 was shown to bind to lipids and pinch off smaller vesicles,
98 similar in size to classic COPI vesicles (Wang et al., 2018). It has been postulated that IFT
99 proteins have evolved from membrane traffic coat complexes: soluble multimeric protein
100 complexes which 'coat' donor membranes, facilitating cargo enrichment and membrane
101 remodeling prior to traffic and fusion with target membranes (Jékely and Arendt, 2006; van
102 Dam et al., 2013). Nonetheless, a functional requirement for an IFT-dependent vesicle-to-cilia
103 traffic module and what its dynamic architecture may resemble is currently unknown.

104 To dissect how traffic of newly synthesized ciliary membrane proteins to the cilium
105 occurs, we undertook a series of biochemical and imaging experiments in *Wdr35* null mouse
106 embryonic fibroblasts (MEFs) (Caparrós-Martín et al., 2015; Mill et al., 2011). To distinguish
107 extra-ciliary functions from canonical retrograde traffic defects, we compared *Wdr35*^{-/-}
108 phenotypes with those of the retrograde IFT dynein *Dync2h1*^{-/-} (Criswell et al., 1996; Huangfu
109 and Anderson, 2005; Porter et al., 1999; Signor et al., 1999). Whilst accumulations of intact
110 IFT-B proteins were observed inside cilia in both mutants, only in the absence of WDR35 does
111 the IFT-A holocomplex fragment and fail to enter *Wdr35*^{-/-} cilia. Without intact IFT-A, we
112 observe broad defects in the ciliary import of diverse membrane and lipidated proteins, as
113 well an accumulation of ‘coat-less’ vesicles around the base of *Wdr35* mutants, which fail to
114 fuse with the ciliary sheath. We demonstrate that together recombinant non-core IFT-A
115 proteins (WDR35, IFT43 and IFT139) are sufficient to specifically bind lipids *in vitro*. Together
116 with our localization data, our results provide the first *in situ* evidence of a WDR35-
117 dependent coat required to deliver essential cargo from vesicles to cilia.

118 Results

119 ***Wdr35* null cells have rudimentary, short cilia with intact transition zones**

120 We utilized primary MEFs carrying null mutations in two components of the retrograde IFT
121 machinery (**Figure 1E**), one part of the motor complex that moves cargos (the retrograde dynein
122 heavy chain *Dync2h1*), and the non-core IFT-A component *Wdr35*, in order to dissect the stage at
123 which ciliogenesis defects occurred (Caparrós-Martín et al., 2015; Mill et al., 2011). Cilia length
124 measured by acetylated α tubulin staining was drastically reduced in both *Wdr35*^{-/-} (0.48 μ m mean \pm
125 0.35 SD) and *Dync2h1*^{-/-} (0.76 μ m mean \pm 0.35 SD) mutants, compared to wild type (WT) (2 μ m mean \pm
126 0.45 SD) MEFs (**Figure 1A, B**). Given there was no reduction in cilia number (**Figure 1C**), as previously
127 shown (Fu et al., 2016; Liem et al., 2012; Mukhopadhyay et al., 2010), our results suggest that
128 DYNC2H1 and WDR35 are needed for cilia elongation at later stages of ciliogenesis. Defects in
129 centriolar satellite traffic, implicated in ciliogenesis, were previously reported for *WDR35* mutant RPE-
130 1 cells (Fu et al., 2016), however we saw no difference in levels or localization of endogenously tagged
131 PCM1 protein (PCM1-SNAP) which marks centriolar satellites in MEFs (**Figure 1- figure supplement 1**).
132 In *C. elegans* non-core IFT-A mutants, extension of the MKS module into the axoneme from the
133 transition zone due to failure of cargo retrieval had been reported (Scheidel and Blacque, 2018).
134 However, we observed intact transition zone modules as shown by NPHP1 and MKS1 localization in
135 both mammalian mutants (**Figure 1D, E**). We noted that *Wdr35*^{-/-} axonemes, while acetylated, were
136 not polyglutamylated suggesting differences in tubulin post-translational modifications (PTMs) and
137 stability (**Figure 1D**). Together these data suggest that the initial steps of ciliogenesis occur in both
138 *Dync2h1*^{-/-} and *Wdr35*^{-/-} mutants, however, subsequent axoneme elongation may be differentially
139 affected.

140

141 ***Wdr35* null cells have intact IFT-B complexes with a retrograde defect and** 142 **unstable IFT-A holocomplexes which fail to enter cilia**

143 Axoneme elongation during cilia assembly requires the import of key building blocks
144 from their place of synthesis in the cell body into the cilium across the transition zone via IFT.
145 We focused first on the anterograde, IFT-B machinery, monitoring two subunits IFT81 and
146 IFT88. We found that IFT-B complex proteins have similar retrograde traffic defects in both
147 *Wdr35*^{-/-} and *Dync2h1*^{-/-} cells (**Figure 2A, B**), accumulating beyond the length of the acetylated
148 axoneme. We next looked to see if IFT-B complex assembly is disturbed in the absence of
149 WDR35 by immunoprecipitation (IP) of endogenous IFT88, followed by mass spectrometry
150 (MS) to identify co-purifying subunits. IFT88 is the link between IFT-B1 and IFT-B2 complexes

151 (**Figure 1E**), interacting with IFT38 on the IFT-B2 side and IFT52 on the IFT-B1 side (Katoh et
152 al., 2016; Mourão et al., 2016; Taschner et al., 2016). MS analysis of immunoprecipitates
153 from E11.5 *Wdr35^{+/+}* and *Wdr35^{-/-}* embryo lysates revealed no statistically significant
154 differences in stoichiometric composition of IFT-B complexes (**Figure 2C, D**). We were able to
155 isolate almost the entire IFT-B complex (14 out of 16 IFT-B components) aside from IFT70,
156 which is not yet reported in mouse as well as IFT25, which binds IFT27 to form a heterodimer
157 (Bhogaraju et al., 2011; Funabashi et al., 2017; Katoh et al., 2016; Wang et al., 2009) and is
158 necessary for Hh signaling (Keady et al., 2012). Because the composition of the IFT-B complex
159 and its ability to enter cilia each appear unaltered, we conclude that exit from cilia is
160 impaired in the absence of WDR35.

161 We next examined the composition of the IFT-A holocomplex in WT vs *Wdr35^{-/-}*
162 embryos by immunoprecipitation of endogenous IFT-A core protein IFT-140 and its
163 interactors. Whilst IFT140 immunoprecipitated all six components of the IFT-A complex from
164 *Wdr35^{+/+}* embryo lysates, in *Wdr35^{-/-}* samples both non-core components IFT139 and IFT43
165 were missing from our MS datasets (**Figure 3A**). Their absence was confirmed by
166 immunoblotting (**Figure 3B**). Moreover, core components IFT122 and IFT144 were also
167 significantly reduced in the purified mutant complex (**Figure 3A**), suggesting that WDR35 is
168 critical for the stability of the IFT-A complex and its components. We also compared total
169 cellular levels of IFT-A component proteins and found IFT139 and IFT43 levels were also
170 undetectable on blots with lysates from both *Wdr35^{-/-}* embryos (**Figure 3C, D**) and MEFs
171 (**Figure 3- figure supplement 1A, B**). This suggests WDR35 is not only critical for the
172 formation of stable IFT-A holocomplex but is also required for stability of its non-core
173 components.

174 In contrast, the individual core components of the IFT-A complex were nearly equally
175 expressed in WT and *Wdr35^{-/-}* lysates, except for IFT122 which had higher expression levels in
176 *Wdr35^{-/-}* MEFs (**Figure 3C, D** and **Figure 3- figure supplement 1A, B**). Other core components
177 have been shown to have higher levels in the absence of WDR35 in human fibroblasts (Duran
178 et al., 2017). Thus, our work also supports previous studies demonstrating a level of
179 interdependence in the levels of IFT-A subunits, which might be required for their
180 coordinated function (Behal and Cole, 2013; Duran et al., 2017; Fu et al., 2016; Picariello et
181 al., 2019; Zhu et al., 2017).

182 These results suggest WDR35 might be a link between IFT-A core and non-core
183 proteins, that when absent results in the decreased abundance of IFT-A non-core subunits.

184 To further distinguish between increased protein degradation from transcriptional changes,
185 control and mutant MEFs were treated with the proteasome inhibitor MG-132 (20 μ M)
186 (**Figure 3E**). Treated cells displayed increased levels of IFT43, which suggests that in the
187 absence of WDR35, non-core proteins may be targeted by the proteasomal degradation
188 pathway. Interestingly IFT139 and IFT121 are degraded in *IFT43* null cells and both are
189 rescued similarly by MG-132 treatment (Zhu et al., 2017), confirming that the stability of IFT-
190 A complex proteins is interdependent.

191 We next looked at the localization and levels of the IFT-A components by
192 immunofluorescence. IFT-A components were present in *Dync2h1*^{-/-} cilia suggesting entry of
193 IFT-A holocomplexes is not affected, but return from the distal tip is compromised in the
194 absence of the dynein motor (**Figure 3F, Figure 3- figure supplement 1C**). In contrast, in
195 *Wdr35*^{-/-} MEFs, IFT-A core components fail to enter cilia and remain restricted at the ciliary
196 base (**Figure 3F**), as shown by the difference in length covered by IFT-A components relative
197 to cilia length measured by acetylated tubulin staining (**Figure 3- figure supplement 1C**),
198 whereas non-core proteins were undetectable, consistent with degradation (**Figure 3C-F**).
199 These results are consistent with previous reports of the inter-dependence of IFT-A
200 components for ciliary localization. IFT140 is decreased in cilia of *IFT122* mutants in mouse
201 and fly (Lee et al., 2008; Qin et al., 2011), IFT139 is reduced in the flagella of *Chlamydomonas*
202 with *IFT144* mutation (Iomini et al., 2009), and IFT144 fails to get recruited into cilia in
203 *WDR35*^{-/-} RPE cells (Fu et al., 2016). IFT-A proteins require CPLANE chaperones for
204 holocomplex assembly and cilia entry (Toriyama et al., 2016). In all cases, failure of IFT-A
205 holocomplex integrity impairs its recruitment into the cilia axoneme. Recent cryo-EM work
206 had suggested IFT-A is being carried by IFT-B trains inside the *Chlamydomonas* flagella in WT
207 cells and these structures are missing in the *IFT139* mutant (Jordan et al., 2018). Our work in
208 the mammalian system in the absence of WDR35 has a similar effect with IFT-B proteins
209 accumulating inside the cilium whilst IFT-A core proteins accumulate proximal to the cilia
210 base, and the non-core components are degraded.

211

212 **Membrane proteins fail to be recruited into *Wdr35*^{-/-} cilia**

213 Cilia membrane protein cargos are synthesized in the cell body (rough ER) and traffic
214 into cilia through a variety of direct and indirect routes. These include lateral diffusion from
215 the plasma membrane (Leaf and Von Zastrow, 2015; Milenkovic et al., 2009), recycling of

216 plasma membrane proteins via the endocytic pathway (Boehlke et al., 2010) as well as more
217 directly from Golgi-derived vesicles (Follit et al., 2008, 2006; Kim et al., 2014; Witzgall, 2018).
218 Moreover, ciliary membrane content is dynamically regulated in response to external signals.
219 First, we tested appropriate dynamic localization of the GPCR Smoothed (SMO), which is
220 recruited to the cilia in response to Hh ligand (**Figure 4A**). SMO is already present in *Dync2h1*^{-/-}
221 mutant cilia, even in the absence of Hh. In contrast, even in the presence of Hh activation,
222 SMO fails to enter *Wdr35*^{-/-} cilia. We investigated endogenous levels and localizations of
223 membrane associated GTPases ARL13B and ARL3, which are enriched in cilia in control cells
224 (**Figure 4A**). We saw that while they accumulate in excess in *Dync2h1*^{-/-} mutants as per a
225 retrograde defect, strikingly they fail to be recruited into *Wdr35*^{-/-} cilia. Detecting low levels
226 of endogenous protein localization and their mislocalization in *Wdr35* mutants by
227 immunofluorescence can be challenging. To overcome this, we transiently expressed
228 membrane cargos, including fluorescently-tagged SMO and ARL13B (**Figure 4B and Video 2**),
229 which effectively traffic into the cilia of WT cells. However, they fail to localize to *Wdr35*^{-/-}
230 cilia, with some accumulation at the cilia base. Interestingly, in our *Wdr35*^{-/-} cells, SMO was
231 predominantly localized to vesicles in the cytoplasm of mutant cells, whereas overexpressed
232 ARL13B when not transported into cilia, is concentrated on other membranes, particularly
233 the plasma membrane and pericentrosomal vesicles (**Figure 4B and Video 2**).

234 In trypanosomes, localization of flagellar membrane proteins was shown to be
235 dependent on lipid rafts highly enriched in axonemes (Tyler et al., 2009). Here, dual acylation
236 was shown to direct potential association with lipid rafts, membrane microdomains that
237 function as specialized platforms for protein/lipid transport and signaling. Indeed, ARL13B
238 requires palmitoylation for its cilia membrane targeting and ciliogenesis in worms and
239 mammals (Cevik et al., 2010; Li et al., 2010; Roy et al., 2017), where it acts as the cilia-
240 localized GEF for ARL3 driving it to release lipid modified cargos from carriers UNC119 and
241 PDE6 δ within cilia membranes (Gotthardt et al., 2015; Kapoor et al., 2015). As ARL13B and
242 ARL3 fail to localize to mutant cilia, we next asked about the ability to recruit general
243 lipidated cargo in *Wdr35*^{-/-} MEFs. We examined the localization of lipidated motifs tagged to
244 EGFP (Williams et al., 2014) to look at specialized membrane microdomains. In WT MEFs,
245 untagged EGFP is present in the cell, but not in the cilium. When tagged with either
246 myristoylation and palmitoylation (MyrPalm) or dual palmitoylation (PalmPalm) motifs, EGFP
247 robustly enriches within cilia (**Figure 4C**). We observed no enrichment of dual geranylation
248 (GerGer) modified EGFP within control fibroblast primary cilia (data not shown), in contrast

249 to the low level expression previously reported in the most proximal portions of highly
250 specialized olfactory sensory cilia (Williams et al., 2014). This suggests that cell-type and cilia-
251 specific differences exist. In marked contrast to WT cells, in *Wdr35*^{-/-} MEFs, both the
252 myristoylation and palmitoylation (MyrPalm) or dual palmitoylation (PalmPalm) EGFP failed
253 to concentrate in mutant cilia (**Figure 4C**). This failure to recruit lipidated cargoes into *Wdr35*
254 mutant cilia is consistent with a more general traffic disruption of ciliary-destined membrane-
255 microdomains, containing broad categories of the membrane and membrane-associated
256 cargos.

257

258 **WDR35 and other IFT-A complex proteins share close sequence and structural** 259 **similarity to COPI complex proteins α and β '**

260 It has previously been suggested that IFTs evolved from a protocoatmer (Jékely and
261 Arendt, 2006; Taschner et al., 2012; van Dam et al., 2013). Three classic coat complexes
262 (COPI, COPII and clathrin) exist and perform similar functions but on different membranes
263 and follow different routes through the cell. They are made of different protein components,
264 which share a similar division of labour, characterized functionally as either adaptors or cage
265 forming proteins. Although components like the cage proteins share significant structural
266 homology in organization of protein domains, they do not share detectable sequence
267 homology (Field et al., 2011). Given the defects in ciliary membrane content observed in the
268 *Wdr35* mutant cilia, we hypothesized that WDR35, in collaboration with other IFT-A complex
269 proteins, may be required for moving ciliary membrane cargos between donor membranes,
270 such as the Golgi or endosomes, to their destination ciliary membrane, in a manner
271 comparable to coat complexes. WD40 repeat (WDR) and tetratricopeptide repeat (TPR)
272 motifs are common throughout cellular proteomes and are involved in a wide range of
273 biological processes. Agnostic of structure, we used deep sequence analysis of the whole
274 human proteome and homology modeling to ask which proteins were most similar to IFT-A
275 components. Simple alignment strategies with proteins such as IFT subunits, which contain
276 tandem repeat motifs, could erroneously align with other repeat proteins to suggest a close
277 evolutionary relationship where none exists (i.e., false positives). To address this, we used
278 four IFT-A subunits (IFT144, IFT140, IFT122 and IFT121) and two of IFT-B (IFT80 and IFT172) as
279 seed sequences for multiple iterative rounds of homology searches via profile-HMM
280 alignment (Remmert et al., 2011). We then clustered the resulting proteins based on

281 sequence similarity, as previously described (Wells et al., 2017; Wells and Marsh, 2019). This
282 was repeated using the COP protein subunits as seeds for reverse analysis. Together, these
283 reciprocal analyses revealed that out of the entire proteome, COPI α and β' cluster most
284 closely with 6 IFT proteins (two IFT-B and four IFT-A components), both having TPR and
285 WD40 repeats (**Figure 5A**). In contrast, homology searches with COPI β and COPI γ 1/2, which
286 have HEAT/ARM repeats, did not yield any hits with IFT components, as was the case with
287 COPI ϵ , which has TPR repeats but no WD40 domains. COPI δ and COPI ζ 1/2, which have no
288 identifiable repeat domains, are most closely related to adaptor protein complex subunits
289 AP2 and AP3. In summary, using multiple rounds of sequence homology searches, we
290 generated a broad set of putatively related repeat proteins, clustering of which reveals clear
291 relationships between coatomers and IFT-A/B complex components.

292 Next, we used SWISS-MODEL (Waterhouse et al., 2018) to predict the structures of
293 IFT-A proteins. COPI α (COPA) and β' (COPB2) structures were top hits with 12 %-15 %
294 sequence identity and 26 %-27 % sequence similarity to four IFT-A complex proteins (IFT144,
295 IFT140, IFT122, and WDR35). Based on the target-template alignment models, built using
296 ProMod3, ribbon diagrams of all 4 IFT-A subunits modeled structures with two N-terminal
297 seven-bladed WD40 β propellers and C-terminal extended TPR repeats, also found in α and β'
298 COPI proteins (**Figure 5 - figure supplement 1A**), as previously modeled for WDR35 (Mill et
299 al., 2011). The remaining 2 IFT-A subunits were not possible to model accurately. IFT139
300 contains only TPR repeats with limited sequence similarity to the ϵ subunit of COPI coatomer
301 (van Dam et al., 2013). IFT43 is the smallest and unstructured protein and could not be
302 modeled and is presumed to be made of α -helices (Taschner et al., 2012). While undertaking
303 this work, a crystal structure for IFT80 was published, highlighting that despite the same
304 domain organization IFT80 adopted a distinctive 3D conformation of the second β -propeller
305 domain from β' -COP and also formed a dimer unlike the triskelion COPI cage (Taschner et al.,
306 2018). However, purified IFT172 adopted two configurations by negative stain electron
307 microscopy (EM) when incubated with and without lipids (Wang et al., 2018). Thus,
308 respecting the limitations of homology modeling without solved structures, we found 4 IFT-A
309 proteins (IFT144, IFT140, IFT122, and IFT121) to have very high sequence and structural
310 similarities to COPI α and β' subunits with N-terminal WD40 repeats and C-terminal TPR
311 region (**Figure 5 - figure supplement 1A**). Given the structural homology of WDR35 and IFT-
312 As to COPI proteins, which derive vesicles from the Golgi, we asked whether WDR35 and IFT-
313 As were sufficient to directly bind membranes.

314

315 **Purified non-core IFT-A can bind directly to specific lipids *in vitro***

316 To test if the IFT-A complex directly associates with lipids *in vitro*, we purified recombinantly
317 expressed IFT-A non-core complex (IFT139/121/43) as well as the dimeric IFT121/43 and the
318 isolated IFT43 subunit of the unicellular organisms *Chlamydomonas reinhardtii* (Cr) using
319 eukaryotic expression systems (**Figure 5B, C** and **Figure 5- figure supplement 1B-D**). All three
320 samples were soluble, eluted as stoichiometric proteins from size-exclusion chromatography
321 and were positively identified by mass-spectrometry. The hetero-trimeric IFT-A complex
322 purified from mammalian cells was assessed for lipid-binding using membrane lipid strips,
323 detecting any bound protein complex using antibodies against the His-Tag on IFT43. From the
324 protein-lipid overlay results in **Figure 5C**, the His-GFP tagged IFT-A trimeric complex displays
325 strong binding to phosphatidic acid (PA) as well as weaker binding to phosphatidylserine (PS).
326 Thus the IFT-A trimeric complex binds to these negatively charged (anionic)
327 phosphoglycerates exclusively, without binding to neutral or inositol-based lipids as had been
328 reported for the IFT-A adaptor TULP3 (Mukhopadhyay et al., 2010). Although there are no
329 reports that PA is a constitutive phospholipid of Golgi apparatus in *Chlamydomonas*
330 *reinhardtii*, it was shown to be the third most abundant phospholipid in cilia (Lehtreck et al.,
331 2013). As a low abundance phospholipid, PA is known to play both important structural roles
332 facilitating membrane curvature during vesicle fusion and fission events (Arisz and Munnik,
333 2011; Zhukovsky et al., 2019) as well signaling functions such as flagellar excision in response
334 to environmental stresses (Goedhart and Gadella, 2004; Lehtreck et al., 2013; Quarmby et
335 al., 1992). To further investigate which subunit of the IFT-A non-core complex is responsible
336 for lipid binding, His-tagged IFT121/43 and IFT43 were also tested in the lipid-strip
337 assay (**Figure 5 - figure supplement 1B-D**). Neither the IFT121/43 dimer nor IFT43 alone
338 showed detectable lipid binding demonstrating that the IFT139 subunit is essential for lipid
339 interaction by the non-core IFT-A complex. In order to further test whether the trimeric IFT-A
340 complex was capable of specifically bind to PA-containing liposomes, we performed negative
341 stain electron microscopy of purified proteins incubated with liposomes composed of
342 PE/PG/PA or POPC (control) (**Figure 5D**). The IFT-A trimer was observed to associate with
343 PE/PG/PA liposomes but not to control liposomes (**Figure 5D**). Consistent with the lipid
344 overlay assay (**Figure 5 - figure supplement 1B-D**), the IFT121/IFT43 dimer display only weak
345 association with PE/PG/PA liposomes (**Figure 5D**). The structural homology of IFT-As to COPI
346 proteins and the ability of the non-core IFT-A complex to bind directly to lipids *in vitro* led us

347 to ask whether IFT-A complex may function similarly to COPI vesicle coats assisting vesicular
348 transport between the Golgi and cilia *in vivo*.

349

350 **Distinct ultrastructural ciliary defects are observed between disruption of IFT-** 351 **A versus the retrograde IFT motor**

352 We undertook ultrastructural studies to examine traffic phenotypes with higher
353 resolution around cilia in MEFs. In all genotypes, ciliation was observed to start very close to
354 the nucleus and remain close to the Golgi stacks throughout cilia elongation (*Figure 6A*,
355 *Video 3; Figure 6B, Video 4; Figure 6C, Video 5; Figure 6 - figure supplement 2, Video 6*). In
356 control MEFs, even after 24 h of serum starvation, very few (~1 %) cilia were observed to
357 emerge from the cell, highlighting the deep-seated ciliary pocket in MEFs (*Figure 6B, Video 4;*
358 *Figure 6 - figure supplement 1 and 4A*), and as described for RPE-1 cells (Molla-Herman et al.,
359 2010). In control MEFs, polymerised microtubules formed a well-structured axoneme (*Figure*
360 *6B, Video 4; Figure 6 - figure supplement 1 and 4A*) as previously described in MEFs
361 (Rogowski et al., 2013) and reported in other primary cilia (Kiesel et al., 2020; Molla-Herman
362 et al., 2010). Additionally, microtubules can be seen attached at the cilia base and radiating in
363 different directions in the cell (*Figure 6 - figure supplement 1*). In contrast to the well-defined
364 ciliary membrane and well polymerized microtubules of the control axoneme, *Wdr35*^{-/-} cilia
365 have ‘wavy’ membranes and disorganized microtubules (*Figure 6C, Video 5 and Figure 6 -*
366 *figure supplement 4B*). Mammalian *Dync2h1*^{-/-} mutants retained a well-defined ciliary
367 membrane and an apparently well-structured axoneme present throughout (*Figure 6 - figure*
368 *supplement 4C, Video 7*), similar to previous reports of the *fla14* dynein mutant in
369 *Chlamydomonas* (Pigino et al., 2009). Stacked standing trains with a periodicity of 40 nm
370 were reported in *fla-14* mutants (Pigino et al., 2009; Stepanek and Pigino, 2016) and in our
371 *Dync2h1*^{-/-} mutant axonemes, we observed similar stacking of stalled IFT trains with a
372 periodicity of 40 nm, irrespective of the length of mutant cilia (*Figure 6 - figure supplement*
373 *4C, Video 7* and (Liem et al., 2012)). Although IFT-Bs also accumulated in *Wdr35*^{-/-} cilia (*Figure*
374 *2A, B*), these stripes were not observed (*Figure 6C, Video 5; Figure 6 - figure supplement 4B*)
375 suggesting that both IFT-B and IFT-A are required to form the higher ordered IFT trains which
376 stall in *Dync2h1* mutants.

377

378 **WDR35 facilitates formation of coated vesicles containing membrane proteins**

379 **destined for cilia**

380 We further tested our hypothesis that IFT-A acts as a coat-like complex for vesicles
381 targeted to cilia by transmission electron microscopy (TEM) analysis of ciliated MEFs. We
382 observed electron-dense coated vesicles between the Golgi and cilia in WT MEFs (**Figure 6A,**
383 **Video 3**). We also observed these coated vesicles clustering at the cilia base (**Figure 6B, Video**
384 **4**) and bulging from ciliary pockets and ciliary sheaths in WT MEFs (**Figure 6 - figure**
385 **supplement 1**). These electron-dense vesicles around control cilia were more prominent at
386 the early stage of ciliogenesis in EM (**Figure 6A, Video 3**).

387 In contrast, in *Wdr35*^{-/-} mutant cells, there is a ten-fold increase in the average
388 number of vesicles around the ciliary base (**Figure 6C, Video 5; Figure 6 - figure supplement**
389 **2, Video 6; Figure 6 - figure supplement 4B; Figure 7 - figure supplement 1A**; quantified in
390 **Figure 7B**). Importantly, virtually all of these mutant vesicles lack the electron-dense coats
391 observed in control cells (**Figure 6C, Video 5; Figure 6 - figure supplement 2, Video 6; Figure**
392 **6 - figure supplement 4B; Figure 7E; Figure 7 - figure supplement 1B**; quantified in **Figure**
393 **7D**). Notably, we did observe other electron-dense coats, likely clathrin, on budding vesicles
394 at the plasma membrane in these same *Wdr35* mutant cells, emphasizing that other coats
395 are preserved in these conditions (**Figure 6 - figure supplement 2, Video 6; Figure 7E**).
396 Moreover, no difference in the density or distribution of periciliary clathrin-positive vesicles is
397 observed around the base of *Wdr35*^{-/-} mutant cilia (**Figure 7 - figure supplement 1C, D**). In
398 contrast, the accumulation of coatless vesicles spreads in a volume $\sim 2 \mu\text{m}^3$ around the
399 *Wdr35*^{-/-} ciliary base (**Figure 6C, Video 5, Figure 6- figure supplement 2, Video 6**, quantified in
400 **Figure 7B, Figure 7 - figure supplement 1A**). In spite of their proximity to the ciliary sheath
401 and their abundance, fusion events were not observed in *Wdr35*^{-/-} mutants (**Figure 6C, Video**
402 **5; Figure 6 - figure supplement 2, Video 6**; quantified in **Figure 8D**). We do not believe this
403 periciliary vesicle accumulation phenotype is a general defect in global membrane traffic as
404 the accumulation of vesicles lacking electron densities occurs specifically around mutant cilia,
405 and not at other regions of *Wdr35* mutant cells (**Figure 6 - figure supplement 3, Video 7**).

406 Clathrin-mediated endocytosis at the ciliary pocket is proposed to regulate
407 internalization of ligand/receptor complexes or membrane content at the base of cilia (Molla-
408 Herman et al., 2010). To test whether these vesicles might be important for the import or
409 export of cargo directed to cilia, we analyzed *Dync2h1*^{-/-} cilia, which we showed to contain
410 increases in IFTs (**Figure 2 and Figure 3**) and membrane protein cargo (**Figure 4**) in the
411 absence of retrograde transport. Consistent with the redistribution of IFT pools from the base

412 into the ciliary compartment (*Figure 2A, and Figure 3F*), we observed no vesicles at the base
413 of *Dync2h1*^{-/-} cilia (*Figure 7A and Video 8*; quantified in *Figure 8D*). Interestingly ectosomes,
414 which are previously reported to regulate the content of cilia in a variety of systems (Cao et
415 al., 2015; Nager et al., 2017; Wood and Rosenbaum, 2014), budding from the tip were much
416 more prevalent in *Dync2h1*^{-/-} cilia than in WT cells (*Figure 6 – figure supplement 4C, Video 8*).
417 We interpret these data as evidence that the coated vesicles around the WT cilia function to
418 transport cargo possibly from the Golgi or via an endosomal intermediate to the cilia. In the
419 absence of WDR35, non-coated vesicles accumulate around the ciliary base marking a failure
420 in this process in either the formation and/or maintenance of this coat and subsequent
421 fusion at the target ciliary pocket.

422 To further confirm our hypothesis that these electron dense vesicles directed to cilia
423 contain WDR35 and IFT-A proteins, we performed correlative light and electron microscopy
424 (CLEM) imaging in *Wdr35*^{-/-} MEFs expressing WDR35-EmGFP, which we had previously shown
425 to completely rescue cilia phenotypes (*Figure 1A, B; Figure 8A*). Expressing WDR35-EmGFP in
426 *Wdr35*^{-/-} ensures that every WDR35 particle was labelled with EmGFP, minimizing
427 competition with non-labeled species. Using Airyscan confocal imaging of WDR35-EmGFP
428 MEFs grown on grids for subsequent TEM, we saw WDR35-EmGFP enriched at the ciliary base
429 of rescued mutant cilia. Moreover, we observed that this signal coincided with the re-
430 appearance of electron-dense vesicles in the TEM images (*Figure 8A, B*). We also observed
431 recovery of fusion events of coated vesicles at the cilia base in cells expressing Wdr35-EmGFP
432 as well as rescue of the periciliary vesicle accumulation phenotype (*Figure 8B, C*, quantified in
433 *Figure 8D, Figure 8 - figure supplement 1, Video 9*). Next, we performed immunogold
434 labelling directly on 70 nm sections and observed sparse but specific labelling of GFP-positive
435 particles at the cilia base, within the axoneme and around putative vesicles at the cilia base
436 and ciliary sheath (*Figure 8 - figure supplement 2, 3*). Together, these results demonstrate
437 that WDR35 is required for the formation of these coated vesicles and that these coated
438 vesicles coincided with WDR35-EmGFP signal, confirming WDR35 supports the assembly of a
439 novel coat on vesicles destined to deliver membrane cargos to cilia.

440

441 Discussion

442 **WDR35 is a component of a novel coat-like complex required for entry of**
443 **cargos into cilia**

444 Vesicle coat proteins, with the archetypal members clathrin and the coat protein
445 complexes I and II (COPI and COPII, respectively), are macromolecular machines that play two
446 central roles in the homeostasis of the cell's endomembrane system. They enable vesicle
447 formation and select protein and lipid cargo packaged for delivery from a specific donor to
448 functionally segregated compartments. Given the deep sequence structural similarities
449 between IFT-A and COPI subunits and the ability of the non-core IFT-A to bind directly to
450 lipids *in vitro*, coupled to the phenotypic defects in *Wdr35*^{-/-} cells (including lack of ciliary
451 enrichment of a broad range of membrane cargos and the absence of electron-densities on
452 accumulated periciliary vesicles), we propose a novel function for WDR35 and other IFT-A
453 proteins to act as a coat-like complex that is critical for the transport of ciliary membrane
454 cargo into cilia. Two other macromolecular complexes have been proposed to form vesicle
455 associated coats involved in ciliary traffic: clathrin (Kaplan et al., 2010; Molla-Herman et al.,
456 2010) and the BBSome complex (Jin et al., 2010).

457 Clathrin is a classical vesicle coating protein with some documented activity at the
458 ciliary pocket (Clement et al., 2013; Pedersen et al., 2016). From static images, the
459 directionality of events is difficult to resolve: fission (endocytosis) or fusion (exocytosis).
460 Clathrin vesicles can be both endocytic, where they concentrate cargos and curve off donor
461 membranes for selective transport into the cytoplasm, or exocytic where they can use fuse to
462 release their contents. For example, a subset of AP-1 clathrin vesicles were shown to traffic
463 between the trans Golgi and basolateral membranes of polarized epithelial cells (Fölsch et al.,
464 1999), via the recycling endosome compartment (Futter et al., 1998). Indeed, in both *C.*
465 *elegans* (Bae et al., 2006; Dwyer et al., 1998; Kaplan et al., 2010; Ou et al., 2007) and
466 trypanosomes (Vince et al., 2008) deletion or depletion of AP-1 leads to defects in cilia
467 assembly and protein traffic into cilia. However, in mammalian cells, depletion of clathrin and
468 clathrin-associated proteins results in a normal number of cilia with normal lengths (Kaplan
469 et al., 2010; Molla-Herman et al., 2010), as opposed to the drastically reduced size of *Wdr35*^{-/-}
470 cilia (Caparrós-Martín et al., 2015; Fu et al., 2016; Mill et al., 2011). This suggests that
471 clathrin is dispensable for vesicular transport into mammalian cilia. Although electron-dense
472 vesicles were observed invaginating from the mammalian ciliary pocket, the electron-density
473 on these vesicular invaginations was unchanged in the absence of clathrin (Molla-Herman et
474 al., 2010). Using live cell-imaging, the directionality of clathrin-mediated traffic was reported
475 to be largely away from cilia (Molla-Herman et al., 2010). Importantly, we still observe
476 clathrin-coated endocytic structures on the plasma membrane of *Wdr35*^{-/-} cells (**Figure 6-**

477 **figure supplement 2; Video 6**), and we found no difference in the distribution of clathrin
478 intensity in a volume of $\sim 2 \mu\text{m}^3$ around the ciliary base in *Wdr35*^{-/-} cilia compared to controls
479 (**Figure 7- figure supplement 1 C,D**). Moreover, studies on clathrin-mediated exocytosis
480 demonstrated that depletion of human clathrin heavy or light chains results in increased total
481 fusion events with complete release of membrane cargos from vesicles in fibrosarcoma cells
482 (Jaiswal et al., 2009), the opposite to what is observed in *Wdr35* mutants where vesicles stack
483 up adjacent to the ciliary sheath but do not fuse.

484 The BBSome is a macromolecular machine of Bardet-Biedl syndrome (BBS) proteins
485 which is also postulated to have evolved from an early ancestral coat complex (Jékely and
486 Arendt, 2006; van Dam et al., 2013). The BBSome shares similar structural elements to the
487 archetypal coats and plays a role in cilia function (Nachury, 2018). In contrast to IFT,
488 mutations in BBSome components, including ARL6/BBS3, do not affect cilia assembly and
489 length regulation (Domire et al., 2011; Eguether et al., 2014; Lechtreck et al., 2013, 2009;
490 Liew et al., 2014; Nager et al., 2017; Shinde et al., 2020; Xu et al., 2015; Ye et al., 2018).
491 Instead, they generally are required for regulating cilia content, mostly for the export of
492 ciliary membrane proteins. Although this suggests that BBSomes regulate movement of
493 ciliary components between compartments, endogenous localization of the BBSome remains
494 unclear, without evidence supporting endomembrane or plasma membrane localization. In
495 contrast, IFT20 localizes to the Golgi (Follit et al., 2006; Noda et al., 2016). Moreover, whilst
496 there is *in vitro* evidence that BBSomes can cluster on liposomes, they do not deform
497 membranes, a key step in vesicle formation by coatomers (Jin et al., 2010). In contrast,
498 purified IFT172, an IFT-B component that is also homologous to COPI α and β' like WDR35,
499 can not only assemble on liposomes with high affinity but can also bud 50 nm vesicles
500 consistent with coatomer sized products (Wang et al., 2018). We report here that the
501 purified trimer of non-core IFT-A (WDR35, IFT43 and IFT139) can also directly and specifically
502 bind to lipids, notably phosphatidic acid (PA) which is involved in membrane deformation in
503 COPI maturation and exocytosis (Yang et al., 2008; Zeniou-Meyer et al., 2007). We are
504 currently testing whether non-core IFT-A can also pinch off vesicles. Together the evidence,
505 including its evolutionary conservation of the BBSome with more classical coat proteins
506 (Jékely and Arendt, 2006; van Dam et al., 2013), interaction with *in vitro* membranes in
507 presence of the ARF-like GTPase ARL-6, interaction with phospholipids (Jin et al., 2010;
508 Nachury et al., 2007) and recent cryo-EM structures of the complex (Chou et al., 2019; Klink
509 et al., 2020; Singh et al., 2020; Yang et al., 2020), suggests the BBSome may be working as an

510 adaptor for IFT-A mediated cage formation, similar to other coat adaptors for clathrin (i.e.,
511 AP1/AP2) or COP (i.e. β -, γ -, δ -, and ζ -COP for COPI). Our data suggests that the electron
512 density observed on vesicles around the ciliary base in control cells is neither clathrin nor
513 BBSome in nature, and is likely composed of WDR35/IFT-A.

514

515 **Mechanism of WDR35/IFT-A-assisted vesicle coat function; regulators of** 516 **vesicular fusion and fission**

517 Our study demonstrates a requirement for IFT-A to deliver ciliary membrane cargo
518 into cilia, potentially by acting as a vesicle coat operating between the Golgi and the ciliary
519 base. Archetypal coatomer protein complexes, including COPII, COPI, and clathrin,
520 concentrate cargo within donor membranes and pinch off vesicles (fission), which then travel
521 to their target organelle membranes, where SNARE and Rab GTPases assist their fusion
522 (Bonifacino and Glick, 2004). In these cases, the electron-dense coats are progressively
523 dismantled such that uncoated vesicles can fuse with acceptor membranes, presumably to
524 facilitate access to the fusion machinery, such as SNAREs, on the surface of the vesicle. As a
525 result of interactions with cargo and lipids with the vesicles, there is evidence that the COPI
526 coat can remain stable on membranes after fission. Moreover, this suggests that COPI vesicle
527 uncoating may be incomplete, such that residual COPI on the vesicle surface enables vesicle
528 recognition and tethering necessary for fusion to the correct acceptor membrane (Orci et al.,
529 1998). In contrast to the trail of electron-dense vesicles between the Golgi and the base of
530 cilia in control cells, we observed ten times more vesicles stalled around the cilia base of
531 *Wdr35*^{-/-} MEFs. These all lack an electron-dense coat suggesting that these transport vesicles
532 are formed but fail to fuse at the ciliary target membrane in the absence of WDR35.

533 This raises a question as to why a protein like WDR35, which shares structural
534 homology to fission-inducing proteins, gives phenotypes consistent with a fusion-facilitating
535 protein. One possibility is that while *Wdr35*^{-/-} MEFs are missing one COPI α/β' - homolog, the
536 other three core IFT-As (IFT144, IFT140, and IFT122) may be sufficient to compensate by
537 providing interaction motifs necessary for the fission of vesicles from donor membranes such
538 as the Golgi. Indeed, we show IFT122 to be upregulated in *Wdr35*^{-/-} mutant cells, similar to
539 previous reports in *WDR35* patient cells (Duran et al., 2017). However, we and others have
540 demonstrated that in the absence of WDR35, the IFT-A complex is unstable (Zhu et al., 2017)
541 such that any core IFT-A coat on the vesicles from donor membranes such as the Golgi may

542 be easily disassembled. It is interesting to note that non-core IFT139 and IFT43 are helical
543 (Taschner et al., 2012) similar to SNARE proteins that mediate vesicle fusion with target
544 membranes. Importantly, we show here that these components, which are degraded in the
545 absence of WDR35, could help mediate the fusion of vesicles with the ciliary pocket or base
546 to transfer membrane cargos into the growing cilia sheath. Indeed, we show that purified
547 non-core IFT-A complex is sufficient to specifically bind phosphatidic acid (PA), which is
548 present in ciliary membranes, as well the Golgi and the recycling endosome compartment
549 (Farmer et al., 2020; Lechtreck et al., 2013; Yang et al., 2008). The lipid composition of
550 membranes is known to determine their curvature (McMahon and Boucrot, 2015); PA being
551 conical in shape, concentrates on more curved regions of membranes resulting in nanoscopic
552 negative curvature such is found in the ciliary pocket (Zhukovsky et al., 2019). Moreover, with
553 a small head group, negative charge, and a phosphomonoester group, PA interacts with
554 proteins and lipids in several subcellular compartments that facilitate fission and fusion of
555 membranes (Zhukovsky et al., 2019). From our liposome assay, we speculate that IFT139
556 binding to the IFT121/43 dimer increases the binding affinity to lipids. Indeed, on its own, the
557 IFT-A dimer signal is below the threshold of detection in the protein-lipid overlay assays but
558 observed to weakly associate to PA-containing liposomes. In our purification of the non-core
559 IFT-A complex with the affinity tag on IFT43, only IFT43/121, rather than IFT43/139, was co-
560 purified together with the trimeric complex, indicating that IFT121 interacts with both IFT43
561 and IFT139, and is responsible for mediating the interactions between IFT43 and IFT139,
562 which is consistent with what has been previously reported (Behal et al., 2012; Zhu et al.,
563 2017). In the *Wdr35*^{-/-} mutant, and likely IFT139 or IFT43 KO strains, the non-core IFT-A
564 complex will not form, which leads to non-coated vesicles (**Figure 9**). Important next steps
565 will be to systematically investigate vesicular traffic defects in other IFT-A mutants, as well as
566 identify the GTPase which acts to drive formation, uncoating and fusion of these vesicles.

567 Recruitment, remodeling, and regulation of protein coats involve cycles of GTP
568 hydrolysis, for example ARF1 regulates recruitment to membranes of the COPI coatomer
569 (Dodonova et al., 2017). It is interesting to note that we and others have been unable to
570 purify IFT-A complex with any GTPases (Mukhopadhyay et al., 2010), suggesting that any
571 interaction is transient. This is even in conditions where we can purify endogenous IFT-B
572 complexes with its associated GTPases IFT22/RABL5 and IFT27/RABL4. In COPI, recruitment
573 of coat components to donor membranes starts with the insertion of small GTPase ARF1 into
574 membranes (Dodonova et al., 2017). So far only one ARF, ARF4 acting at the TGN (Mazelova

575 et al., 2009; Wang et al., 2017) has been implicated in ciliary traffic. However, it plays non-
576 ciliary roles, and shows early lethality in mouse knock-outs without affecting cilia assembly
577 (Follit et al., 2014). Mutations in several related ARLs have defects in cilia structure and/or
578 content, including ARL3, ARL6 and ARL13B (Alkanderi et al., 2018; Cantagrel et al., 2008; Fan
579 et al., 2004). At least in the case of ARL13B and ARL3, they fail to accumulate and/or enter
580 mutant cilia, even when overexpressed in the absence of WDR35, although periciliary
581 vesicular staining can be observed. Rab GTPases have been implicated in the ciliary targeting
582 of vesicular cargos (Blacque et al., 2018). Notably, expression of dominant negative RAB8 in
583 *Xenopus* photoreceptors (Moritz et al., 2001) results in a strikingly similar accumulation of
584 vesicles to our *Wdr35* mutants which fail to fuse with the ciliary base. Similarly, in RPE-1 cells,
585 dominant negative RAB8 impairs traffic of ciliary membrane cargos (Nachury et al., 2007).
586 However, functional redundancy between RABs may exist as neither single nor *Rab8a;Rab8b*
587 double mutant mice have defects in cilia formation. On the other hand, defects in ciliation
588 were observed when *Rab10* was additionally knocked down in *Rab8a;Rab8b* double mutant
589 cells (Sato et al., 2014). Excitingly, our work demonstrates IFT-As to be important for the later
590 stage of ciliogenesis, similar to GTPases like RAB23 (Gerondopoulos et al., 2019) or RSG-1
591 (Agbu et al., 2018; Toriyama et al., 2016). Given that these GTPases have also been shown to
592 sequentially interact with CPLANE subunits INTU and FUZ, which are also required for IFT-A
593 holocomplex assembly (Gerondopoulos et al., 2019; Toriyama et al., 2016), they will be
594 priorities for future investigations.

595 We have demonstrated that an IFT-A-dependent coat for membrane vesicles exists
596 and is necessary for their fusion with the ciliary sheath and ciliary pocket, which is continuous
597 with the ciliary membrane. We also showed that this coat is necessary to efficiently deliver
598 cilia-destined signaling molecules into the elongating axoneme of the cilium. This raises the
599 possibility that some of this IFT-A dependent coat may remain upon vesicle fusion as a now
600 linear 'train' carrying membrane cargos to be picked up by cytosolically assembling IFT-B
601 particles allowing import across the transition zone and then anterograde IFT within the
602 cilium (**Figure 9, insert B**). Excitingly, we show that purified non-core IFT-A including WDR35
603 is sufficient to bind selectively to phosphatidic acid (PA). This low abundance signalling lipid
604 has well-described roles in vesicle traffic through where it promotes COPI vesicle fission in
605 the Golgi (Yang et al., 2008), maintenance of the endosome recycling compartment (ERC)
606 (Farmer et al., 2020) as well as promoting exocytosis through formation of fusion competent
607 granules (Zeniou-Meyer et al., 2007). Defining at which points in vesicular traffic IFT-A

608 dependent coats act, both fission and fusion, within cells as well as the biochemical nature of
609 lipids and cargos these vesicles carry will be required. Given its efficacy, this IFT-dependent
610 ‘targeted delivery’ module may also be repurposed for other non-ciliary membrane targeting
611 events via polarized exocytosis. Notably in the immune synapse of T cells, where IFT20 is
612 required for rapid clustering of TCRs necessary for T cell activation (Finetti et al., 2009) as well
613 as photoreceptor dendrites in which IFT localization to vesicles tracking towards the
614 postsynaptic membranes was observed (Sedmak and Wolfrum, 2010), where dendritic
615 exocytosis is implicated synaptic plasticity and neuronal morphology (Kennedy and Ehlers,
616 2011). Future studies into this IFT-dependent coat complex and the membrane traffic
617 processes it controls may expand our phenotypic understanding of the ciliopathies beyond
618 the cilium.

619

620 **Material and Methods**

621 **Preparation of primary MEFs, cell culture, ciliation and genotyping**

622 Primary MEFs were harvested from E11.5 embryos and cultured in complete media [Opti
623 MEM-I (Gibco, 31985-047) supplemented with 10 % foetal calf serum (FCS) and 1 % penicillin-
624 streptomycin (P/S) and 0.026 μ l β -mercaptoethanol] and incubated at 37 °C in a hypoxic
625 incubator (3 % O₂ and 5 % CO₂). To induce ciliogenesis, 70-80 % confluent cells were serum-
626 starved for 24 h. Genotyping was done as described before for the *Wdr35* line (Mill et al.,
627 2011) and *Dync2h1* line (Caparrós-Martín et al., 2015). *Pcm1-SNAP* mouse line was made by
628 Dr. Emma Hall (Hall E. et al., unpublished) by endogenous tagging of PCM1 by CRISPR.
629 *Pcm1*^{SNAP} mouse line was crossed with *Wdr35*^{-/+} and genotyped to screen E11.5 embryos
630 homozygous for both *Wdr35*^{-/-} and *Pcm1*^{SNAP/SNAP}. MEFs prepared from these embryos were
631 used to image PCM1 localization in WT and *Wdr35*^{-/-} using antibodies and other reagents
632 listed in **Table 1**.

633

634 **Electroporation of MEFs**

635 Cells were trypsinized to a single-cell suspension and resuspended in 10 μ l Resuspension
636 Buffer R per 0.5 x 10⁵ cells/transfection reaction, mixed with plasmid DNA (0.75
637 μ g/transfection) **Table 3** and electroporated (voltage 1350 V, width 30 ms, one pulse) using a
638 Neon Nucleofection kit (Thermo Fisher Scientific MPK-1096), according to the manufacturer’s
639 protocol. Transfected cells are harvested or visualized 24-48 h post electroporation.

640

641 **Live Cell Imaging**

642 Primary MEFs (0.5×10^5 cells/transfection) were electroporated with *ARL13B-EGFP* or
643 *Smoothed-GFP* using the Neon™ Transfection System, 10 μ L Kit (Thermo Fisher Scientific,
644 MPK-1096) and seeded in 24 well glass-bottomed plates (Greiner Sensoplates, 662892) with
645 pre-warmed media (Opti-MEMI® (1X) (Gibco, [31985-047](#)), 10 % foetal calf serum (FCS) and
646 0.026 μ l β -mercaptoethanol). Samples were incubated in antibiotic-free media 37 °C/ 5% CO₂
647 / 3% O₂ overnight and then serum-starved for 24 h. SiR-tubulin kit (Spirochrome, SC002), a 1
648 mM stock solution, was prepared in anhydrous DMSO and stored at -20 °C, without
649 aliquoting. For staining, 1:5000 (200 nmol) of SiR-tubulin stock was diluted in serum-free
650 media, and added to cells for 1 h in the hypoxic incubator, then live imaged without washing.
651 For live-cell PCM1 imaging, MEFs electroporated with *ARL13B-EGFP* were incubated with
652 1:1500 TMR-SNAP (New England BioLabs, S9105S, stock 30 nmol) in low serum media in the
653 hypoxic incubator for 30 min. Cells were washed twice with low serum media for 1 h each in
654 the incubator. Samples were then incubated for 1 h in 1:5000 SiR-tubulin (200 nmol). Hoechst
655 344442 (Thermo Fisher Scientific, H1399) was added 10 min before imaging. Plates were
656 allowed to equilibrate in the Okolabs stage top incubator before confocal imaging on the
657 Leica SP5 using the LAS-AF software, 405 nm diode, Argon and 561 and 648 nm laser lines,
658 three Photomultiplier tubes, and one HyD GaSP detector, as per the requirement of the
659 experiment. Images were scanned using a 63X 1.4 NA oil immersion objective and processed
660 using ImageJ and Imaris software.

661

662

663 **Endogenous IFT IPs**

664 Embryos were lysed and homogenized in IP lysis buffer (10 μ l/mg) at 4 °C on a rotator for 30
665 min. Composition of IP lysis buffer is (50 mM Tris-HCl (pH 7.5), 100 mM NaCl, 10 % glycerol,
666 0.5 mM EDTA, 0.5 % IGEPAL, and 1/100 Halt protease and phosphatase inhibitor (Thermo
667 Fisher Scientific, 78443) and a tablet of protease inhibitor tablet - 1 tablet per 10 ml
668 (Complete Mini, Roche, 11836170001). The lysate was cleared by spinning at 4 °C, 14,000
669 rpm, for 20 min. The protein concentration was determined using the BCA Protein Assay Kit
670 as per manufacturer's instruction (Thermo Fisher Scientific, 23225). For each IP, 500 μ g of
671 protein was incubated with 3 μ g of each antibody overnight at 4 °C (**Table 1**) with mild
672 agitation (side-to-side). Immunoprecipitation of immunocomplexes was done using

673 PureProteome™ Protein G magnetic beads (Millipore LSKMAGG10). 30 µl beads/IP were
674 equilibrated with 500 µl IP lysis buffer by gentle agitation for 5 min at 4 °C. Tubes were
675 placed on a magnet for 2 min, and the buffer was aspirated off with the fine pipette. 200 µl
676 antibody-lysate mix was added to each tube of 30 µl equilibrated beads and incubated for 45
677 min with agitation, to concentrate immunoglobulin complexes on beads at 4 °C. Washes (8
678 times) were performed, each lasting 5 min. Washes were as follows: 2x washes in Wash
679 Buffer-1 (same as IP lysis buffer), followed by 2x washes with Wash Buffer-2 (IP lysis buffer
680 with reduced 0.2 % IGEPAL), finally 4x washes with Wash Buffer-3 (IP lysis buffer without any
681 IGEPAL detergent). All wash buffer is aspirated, and dry beads were stored at -80 °C, or
682 samples were sent immediately for mass spec.

683

684 **Mass spectrometry**

685 All mass spectrometry experiments were done at the IGMM Mass Spectrometry facility, as
686 per their published protocol (Turriziani et al., 2014). Briefly, the immunocomplexes collected
687 on magnetic beads were processed to generate tryptic peptides. Proteins were eluted from
688 beads by incubating at 27 °C for 30 min in elution buffer (2 M urea, 50 mM Tris-HCl pH 7.5
689 and 5 µg/mL trypsin). The sample was centrifuged, bead pellets washed twice and the
690 supernatant from samples digested overnight at room temperature. Iodoacetamide was
691 added to the samples to inhibit disulfide bond formation and incubated for 30 min in the
692 dark. Followed this, trifluoroacetic acid (TFA) was added to stop tryptic digestion. Desalting
693 and pre-fractionation of the digested peptides were done by manually using C18 pipette
694 stage-tips filled with 3M Empore disc activated with 50 % acetonitrile and 0.1 % TFA and then
695 washed once with 0.1 % TFA. The peptide mixtures were passed manually along to the
696 column with a syringe to concentrate and purify the analytes. Peptides were subsequently
697 eluted twice in 50 % acetonitrile and 0.1 % TFA and both eluates were combined. Samples
698 were concentrated and resuspended in 0.1 % TFA. This was followed by chromatographic
699 separation on a Reprosil column along a 3-32 % acetonitrile gradient. The LC setup was
700 attached to a Q-Exactive mass spectrometer, and ion mass spectra were obtained following
701 HPLC during a tandem MS run. Mass spectra were analyzed using MaxQuant software. Label-
702 free quantification intensity (LFQ) values were obtained for analysis by identifying
703 mass/charge ratio, and their intensities at a specific elution time for individual peptides. The
704 data was collected for both control (GFP) and specific proteins IPs (i.e., IFT88, IFT140 - **Table**
705 **1**). LFQ values for the proteins were obtained by summing the ion intensities corresponding

706 to peptides after assigning the unique peptides to proteins. The ratio of LFQ intensities of
707 test: control was taken, where higher the ratio better corresponds to a better enrichment of
708 protein in complex. Complete mass spec data is available on ProteomeXchange (*identifier*
709 *PXD022652*). The relative concentration of IFTs was calculated after normalizing the
710 individual test values with respective GFP- LFQs, as shown in the figures.

711

712 **Western Blots**

713 Cells or tissues were lysed in 1X Cell Lysis Buffer with the addition of 1/100 Halt protease and
714 phosphatase inhibitor (Thermo Fisher Scientific, 78443) and a Complete protease inhibitor
715 tablet, 1 tablet per 10 ml (Complete Mini, Roche, 11836170001). Prepare 1X Cell Lysis Buffer
716 by diluting 10X stock in ddH₂O (Cell Signalling Technology (10x #9803): 20 mM Tris-HCl (pH
717 7.5), 150 mM NaCl, 1 mM Na₂ EDTA, 1 mM EGTA, 1 % Triton-X100, 2.5 mM sodium
718 pyrophosphate, 1 mM β-glycerophosphate, 1 mM Na₃VO₄, 1 μg/ml leupeptin). The lysate
719 from embryos was homogenized at 4 °C for 30 min and from cells was sonicated briefly (5x,
720 10-sec pulses, Bioruptor Diagenode) to lyse the tissue or cells. The lysate was centrifuged at
721 14,000 g at 4 °C for 30 min and the supernatant transferred to a fresh tube. Ready-to-use
722 SDS-PAGE gels (NuPage Novex precast gels, Thermo Fisher Scientific) were used to separate
723 proteins.

724 The resolved proteins on the gel were transferred to PVDF (Hybond P, GE HealthCare) using
725 the XCell II Blot module as per manufacturer's instruction. The membrane was then blocked
726 with a 10 % solution of dried skimmed milk (Marvel Premier Foods) made in 1X TBST (0.05 %
727 Tween-20 in TBS) for 1 h RT, washed with PBS and incubated with primary antibody (**Table 1**)
728 diluted in 1 % skimmed milk solution in 1X TBST overnight at 4 °C on shaker/roller.
729 Membranes were washed in 1X TBST 3X, 10 min followed by a 1X wash with PBS, and
730 incubated in HRP-conjugated secondary antibody from appropriate species (**Table 2**) for 1 h
731 at RT, diluted in a solution of 1X TBST and 1 % milk. Blot was then washed with 1X TBST, three
732 times and with PBS twice. After the washes, signals were detected by the Super Signal ELISA
733 Femto kit (Thermo Fisher Scientific, 37074) or Super Signal ELISA Pico kit (Thermo Fisher
734 Scientific, 37069). Protein bands were visualized digitally by transmission light imaging on
735 ImageQuant LAS 4000 (GE HealthCare) and analyzed using ImageQuant TL software. Protein
736 bands on blots were quantified with ImageJ/FIJI software by measuring individual bands
737 intensity and normalizing intensities with loading control bands on the same blot.

738

739 Immunofluorescence

740 Cells were washed two times with warm PBS, then fixed in either 4 % PFA in 1X PHEM/PBS 15
741 min at room temperature, 2 % fresh glutaraldehyde in 1X PHEM for 15 min, or pre-extracted
742 for 30 s on ice in PEM (0.1 M PIPES pH 6.8, 2 mM EGTA, 1 mM MgSO₄) prior to fixing in ice
743 cold methanol on ice for 10 minutes according to **Table 1**, then washed twice with PBS. 1X
744 PHEM (pH 6.9) contains: 60 mM PIPES, 25 mM HEPES, 10 mM EGTA, and 4 mM MgSO₄·7H₂O).
745 The cells were treated twice with 50 mM NH₃Cl for 15 min each for PFA fixed cells, or 0.01 mg
746 of NaBH₄ in 1X PBS for 7 min for glutaraldehyde fixed cells to quench autofluorescence. Cells
747 were then washed twice with PBS. Cells were permeabilized with 0.25 % Triton-X 100/TBS for
748 10 min at room temperature. Cells were rinsed twice in 1X TBS for 5 min. Blocking for non-
749 specific binding was done by incubating samples in 10 % donkey serum in 0.2 % Tween-
750 20/TBS for 60 min at room temperature. Samples were washed twice with PBS. Primary
751 antibodies (**Table 1**) were added to samples and incubated for 60 min at room temperature
752 or 4 °C overnight, in dilutant made of 1 % donkey serum in 0.025 % Triton X-100/TBS.
753 Samples were washed in 0.25 % Triton-X 100/TBS 4-6 times, 10 min each. Secondary
754 antibodies diluted in 1 % donkey serum and 0.025 % Triton X-100/TBS were incubated on
755 samples for 60 min room temperature. Samples were washed with 0.25 % Triton-X 100/TBS
756 4-6 times 10 min, stained with DAPI (1:1000) in PBS for 5 min at room temperature, again
757 washed with PBS and directly imaged or coverslips were added on slides using ProLong Gold
758 antifade (ThermoFisher Scientific), according to the manufacturer's instructions. Confocal
759 imaging for was done on a Leica SP5 using the LAS-AF software, 405 nm diode, Argon and 561
760 and 648 nm laser lines, three Photomultiplier tubes, and one HyD GaSP detector, as per the
761 requirement of the experiment. Images were scanned using a 63X 1.4NA oil immersion
762 objective and latter processed using ImageJ and Imaris software.

763

764 IFT-A sequence homology search and structural modelling

765 The sequence match of IFT-A proteins was found by iterative rounds of homology searches
766 via alignment for sequence proximity-based clustering as described before (Wells et al., 2017;
767 Wells and Marsh, 2019). Further Swiss Model server was used to model IFT-A complex
768 protein structures as described on the server (Waterhouse et al., 2018). Briefly, a template
769 search with BLAST and HHblits was performed against the SWISS-MODEL template library.
770 The target sequence was searched with BLAST against the primary amino acid sequence
771 contained in the SMTL. An initial HHblits profile, followed by one iteration of HHblits against

772 NR20, was run and the obtained profile then searched against all profiles of the SMTL. The
773 top hit in all of IFTA searches was 3mkqA (Lee and Goldberg, 2010), a coatomer β' subunit 2.5
774 Å X-ray structure with 14 % - 20 % sequence identity and 25 % - 30 % sequence similarity with
775 different IFT-A proteins. A coatomer α subunit was also found within these top matches.
776 Models were built on the target-template alignment using ProMod3. Coordinates that are
777 conserved between the target and the template were copied from the template to the
778 model. Insertions and deletions were remodelled using a fragment library. Side chains were
779 then rebuilt. Finally, the geometry of the resulting model was regularized by using a force
780 field. In case loop modeling with ProMod3 fails, an alternative model was built with
781 PROMOD-II. The global and per-residue model quality has been assessed using the QMEAN
782 scoring function. The obtained model was processed later in Pymol software for structural
783 analysis.

784

785 **Cloning, expression and purification of the *Cr* IFT-A trimeric (IFT139/121/43)** 786 **complex from mammalian cells**

787 The codon-optimized sequences for *Chlamydomonas reinhardtii* IFT-A trimeric complex
788 (UniProt accession codes: IFT43_A8HYP5, IFT121_A8JFR3 and IFT139_A9XPA6) were
789 assembled into a single construct for expression in mammalian cells. The *IFT43* gene was
790 fused to TEV cleavable His-GFP-tag at the N-terminus for affinity purification and inserted
791 into pAceCMV vector while the *IFT139* and *IFT121* subunits were untagged. The
792 pAceCMV_His-GFP-IFT43, pIDC_IFT121 and pIDK_IFT139 were fused using an *in vitro* Cre
793 recombinase (New England Biolabs) by the LoxP sites in the vectors to form the IFT-A trimer
794 construction.

795

796 Large-scale transient expression of the IFT-A trimeric complex in mammalian HEK293S cells
797 was carried out by transfection of the IFT-A trimer construct using PEI (40 kDa linear
798 polyethylenimine, 1 mg/ml stock in water). Before transfection, sterile and high-quality DNA
799 was prepared using a NucleoBond Maxiprep Kit (MACHEREY-NAGEL) with 200 ml overnight
800 culture of DH5 α cells containing the construct. HEK293S cells were cultivated one day before
801 the transfection in medium (FreeStyle™ 293 Expression Medium, Thermo-Fisher) with 1 %
802 FBS and 1 % penicillin/streptomycin. Cultures were incubated in a humidified incubator with
803 5 % CO₂ at 37 °C with 130 rpm shaking to let the cells grow. The cells were diluted to 1.1 x 10⁶
804 cells/ml before transfection with fresh and warm medium. The transfection mixtures were

805 prepared using a sterile flow bench. For expression in 1 L of HEK293S cells, 1000 µg IFT-A
806 trimer DNA were diluted into 25 ml medium without antibiotics or FBS. In another tube, 3000
807 µg PEI were diluted in 20 ml medium and added to the diluted DNA dropwise. The mixture
808 was incubated at room temperature for 5 min to let the PEI-DNA transfection complex form.
809 The mixture was added dropwise to cells and mixed gently by swirling the flask. Cells were
810 incubated at 37 °C in a CO₂ incubator for 48 h. The cells were harvested by centrifugation at
811 800 x g for 10 min at 4 °C, and the cell pellet was flash-frozen in liquid nitrogen and stored at
812 -80 °C until use.

813
814 The IFT-A trimeric complex was purified using the His-tag on the IFT43 for affinity
815 chromatography. Briefly, a frozen pellet from 1.5 L of HEK293S cell culture was thawed on ice
816 and resuspended in lysis buffer (50 mM HEPES pH 7.4, 250 mM NaCl, 2 mM MgCl₂, 10 % (v/v)
817 glycerol and 5 mM β-mercaptoethanol) supplemented with 1 µl DNase and one Complete
818 Protease Inhibitor tablet (Complete-EDTA Free Protease Inhibitor tablet, Roche Applied
819 Science) to a final volume of 20 ml. Cells were lysed in a dounce-type tissue grinder
820 (Wheaton) using 30 strokes. The cell lysate was cleared by centrifugation at 48,000 x g for 45
821 min at 4 °C. The clarified supernatant was loaded onto a 1 ml TALON column (HiTrap, Cytiva)
822 pre-equilibrated with lysis buffer at 4 °C. The bound protein was washed with 15 mM
823 imidazole in Q_A buffer (20 mM Tris-HCl pH 7.5, 10 % glycerol, 50 mM NaCl and 5 mM β-
824 mercaptoethanol), followed by elution with 150 mM imidazole in Q_A buffer. The elution
825 containing the IFT-A proteins was loaded onto a 5 ml Q column (HiTrap Q FF, Merck-
826 Millipore), and the bound IFT-A proteins were eluted in Q_A buffer with a 50-500 mM gradient
827 of NaCl. The elution fractions containing the IFT-A proteins were concentrated to 500 µl in a
828 100 kDa molecular weight cut-off concentrator (Amicon Ultracel, Merck-Millipore) for
829 subsequent Size Exclusion Chromatography (SEC) on a pre-equilibrated Superose 6 Increase
830 column (10/300 GL, Merck-Millipore) in SEC Buffer (10 mM HEPES pH 7.5, 150 mM NaCl, 2
831 mM MgCl₂, 1 mM DTT, 5 % glycerol). The SEC peak fractions were analyzed by SDS-PAGE and
832 resulted in the sample used in **Figure 5B** and **C**.

833

834 **Cloning, expression, and purification of *Cr* His-IFT43, His-IFT43/121 and His-** 835 **IFT43/121/139 from insect cells**

836 DNA sequences encoding for the *IFT43* with an N-terminal TEV cleavable hexa-histidine tag
837 and untagged *IFT121* were cloned into the two expression cassettes of the pFL vector. The

838 gene encoding for *IFT139* was cloned in another pFL vector.

839

840 The expression and purification of His-IFT43, His-IFT43/121 complex and His-IFT43/121/139
841 complex was performed as previously described for the CrODA16 protein (Taschner et al.,
842 2017) with the following modifications. Two recombinant baculoviruses for IFT139 and
843 IFT43/121 were generated from separate constructs. The expression was carried out in sf21
844 suspension cells by co-infection with these two recombinant baculoviruses. After 3 days of
845 incubation at 27 °C, the cells were harvested by centrifugation.

846

847 The His-43, His-IFT43/121 and His-IFT43/121/139 were purified using a similar purification
848 procedure to that for the His-GFP-tagged IFT-A trimer describe above, and were purified by
849 Ni-NTA affinity, ion-exchange and size exclusion chromatography. The SEC fractions
850 containing His-tagged IFT-A proteins were used for the lipid overlay assays in **Figure 5- figure**
851 **supplement 1B-D**.

852

853 The purified His-IFT43/121 and His-IFT43/121/139 were digested overnight using TEV
854 protease for removal of His-tag. The resulting IFT-A proteins was loaded onto SEC, and
855 fractions containing untagged IFT-A proteins were further used for the binding assay with
856 liposomes in **Figure 5D**.

857

858 **Lipid overlay assay**

859 To detect the direct binding between non-core IFT-A complexes and lipids, the His-GFP
860 tagged IFT-A trimeric complex or His-tagged proteins purified from insect cells and
861 Membrane Lipid Strips (Echelon Biosciences, P-6002) with 100 pmol of fifteen different lipids
862 were used following the manufacturer's protocol. The strips were blocked in 3 % (w/v) BSA in
863 TBS-T buffer (50 mM Tris (pH 7.4), 150 mM NaCl, and 0.1 % (v/v) Tween 20) at 4 °C overnight
864 in dark with gentle agitation. After blocking, they were washed in TBS-T buffer three times
865 and 5 min each, followed by incubation at room temperature for 1 h with IFT-A proteins in
866 SEC buffer supplemented with 3 % (w/v) BSA. The strips were washed three times in TBS-T as
867 before and soaked in 3 % (w/v) BSA in TBS-T with primary antibody against His-tag (THE His
868 Tag Antibody, Mouse, GenScript) at a 1: 2,500 dilution for 1 h at room temperature. Strips
869 were washed three times and incubated with Horseradish peroxidase (HRP)-conjugated
870 polyclonal rabbit anti-mouse immunoglobulins (1: 1,000 dilution, Dako) for 1 h followed by

871 three TBS-T washes. An ECL Prime Western Blotting reagent (Amersham) was used as the
872 substrate for the horseradish peroxidase, and the binding of IFT-A proteins onto spotted
873 lipids was recorded with the ChemiDoc imaging system (BioRAD).

874

875 **Negative stain EM**

876 The POPC-liposomes and PA containing liposomes (PE/PG/PA) were purchased from T&T
877 SCIENTIFIC CORP. The liposomes (PE/PG/PA) have a similar phospholipids composition to that
878 of *Chlamydomonas* ciliary membrane as reported previously (Lechtreck et al., 2013). The
879 percentage of PA was 11.36 % while the ratios of PE and PG as the framework of liposomes
880 were re-quantified to 63.18 % and 25.46 % respectively.

881

882 To observe the binding between IFT-A complexes with liposomes, the liposomes (PE/PG/PA,
883 0.20 mM) were applied to homemade carbon grids directly or after incubation with IFT-A
884 complexes (untagged IFT139/121/43 trimer or IFT121/43 dimer, 0.25 μ M) at 25 °C for 10 min.
885 3 μ l of the sample were applied to the plasma-cleaned grids for 30 sec before it was blotted,
886 and the sample was stained with 2 % (w/v) uranyl-format staining by applying 3 μ l of stain
887 three times on the grids. The negative stain grids were imaged on an FEI Tecnai G2 Spirit
888 Transmission Electron Microscope (TEM) operated at 120 kV with a 67,000 X nominal
889 magnification corresponding to the digital pixel size of 1.59 Å/pixel. The electron micrographs
890 were recorded on a water-cooling 4k CMOS CaMeRa (TemCam-F416). The mixture of IFT-A
891 trimer (0.10 μ M) with POPC liposomes (0.20 mM), as a negative control, was checked using
892 negative staining EM by following the same procedure.

893

894 **Transmission electron microscopy**

895 TEM sample preparation: 24 h serum-starved MEFs were chemically fixed for flat embedding
896 using the following protocol: (1) Cells were grown on 60 mm dishes, and ciliogenesis was
897 induced by serum starvation for 24 h. (2) For prefixation under culture conditions, 25 %
898 glutaraldehyde was added to the growth medium to a final concentration of 1 %, mixed
899 gently, and incubated for a few min at 37 °C. (3) The growth medium (containing the
900 glutaraldehyde) was replaced with a sample buffer (0.1 M HEPES, 4 mM CaCl₂, pH 7.2)
901 containing 2 % glutaraldehyde and incubated 1 h at room temperature (replacing the fixation
902 buffer with fresh one after 20 min). All prefixation solutions were pre-warmed to 37 °C, and
903 all steps were done at 37 °C, to preserve the cytoskeleton. (4) The fixation buffer was

904 replaced with fresh fixation buffer and incubated for 4 h at 4 °C. (5) After that, the sample
905 was washed once in sample buffer and 2–3 times in distilled water, each for 5–10 min, gently
906 removing and replacing the buffer. (6) Samples were incubated in 1 % OsO₄ (EMS) (in distilled
907 water) for 1 h at 4 °C, (7) washed 3–4 times for 10 min each in distilled water, and (8)
908 incubated in 1 % uranyl acetate (EMS) in distilled water overnight at 4 °C. (9) Then, samples
909 were rinsed 3–4 times for 10 min each in distilled water and (10) dehydrated using a
910 graduated series of ethanol: 30 %, 50 %, 70 %, 80 %, 90 %, 96 % ethanol, 5 min each step at 4
911 °C, followed by twice rinsed in anhydrous 100 % ethanol 10 min each at RT. (11) Infiltration
912 was performed using a 1:1 mixture of LX112 (Ladd Research, USA; EMS) and ethanol 2 h,
913 followed by pure LX112 overnight and another 2 h pure LX112, where all steps were
914 performed at room temperature. (12) Flat embedding: For flat embedding, the caps of the
915 BEEM embedding capsule (size, #3, EMS) were cut off and capsules filled with LX112. The
916 capsules were inverted over a selected area of the cell monolayer in the dish, and the resin
917 cured at 60 °C oven for 48 h. The capsule was then removed by breaking off from the dish,
918 leaving the monolayer cells embedded in the surface of the block. (13) Sectioning and post-
919 staining: For sectioning and post-staining, 300 nm thick serial sections were cut by Leica
920 Ultracut UCT (Leica microsystem, Wetzlar, Germany) with a diamond knife and sections
921 picked up with a Formvar (EMS) coated 1x2 mm slot copper grid (EMS). Sections were post-
922 stained with 2 % uranyl acetate for 10 min, then with lead citrate for 5 min. Imaging: Sections
923 were stained on the grid with fiducials (15 nm gold nanoparticles, Sigma-Aldrich). 70 nm thick
924 sections were cut for regular TEM imaging, and 300 nm thick sections were prepared for
925 tomographic acquisition.

926 Tilt series were acquired on a Tecnai F30 (FEI) transmission electron microscope, operated at
927 300 kV, and equipped with 2048x2048 Gatan CCD camera and FEI Titan Halo transmission
928 electron microscope operated at 300 kV equipped with a field emission gun (FEG) and a
929 Gatan K2 direct detector. The SerialEM software (Mastronarde, 2005) was used for automatic
930 acquisition of double tilt series. Tomographic tilt series were recorded with a pixel size of
931 1.235 nm on Titan Halo and 1.178 nm on F30, a maximum tilt range of about 60°, and tilt
932 steps of 1°. Tomographic reconstruction, joining of tomograms from consecutive sections,
933 segmentation, and visualization of the tomograms was done using the IMOD software
934 package (Kremer et al., 1996). In wild type cells, very few vesicles are observed around the
935 base of the cilia which mostly have electron-dense coats with a range of intensities, including
936 those observed fusing with the ciliary pocket or sheath. For simplicity, we have labeled these
937 as 'coated' and coloured them magenta. By comparison, the accumulation of vesicles around

938 the base of *Wdr35* mutant cilia generally lack prominent densities around them. For
939 simplicity, we have labeled these as 'coatless' and coloured them cyan, as whether coats
940 previously existed but disassembled or whether they failed to form in the first place is not
941 clear from our study.

942 24 h serum-starved WT, *Wdr35*^{-/-}, and *Dync2h1*^{-/-} cells were serially sectioned parallel
943 to the adherent surface. Two to four 300nm parallel serial sections are required to get the
944 whole 3D volume ultrastructural view covering full cilia and their cellular surroundings. We
945 reconstructed 45 tomograms to get a minimum of 3-4 whole cell volumes for each genotype.
946 We took micrographs of 30 WT, 20 *Wdr35*^{-/-}, and 30 *Dync2h1*^{-/-} cells for this study.

947

948 **CLEM (correlative light and electron microscopy)**

949 WDR35-EmGFP and ARL13B-mKate expressing *Wdr35*^{-/-} MEFs were serum-starved for 24 h,
950 stained with Hoechst 33342 (R37605) for 10 min in culture condition, fixed with 4 % PFA and
951 0.1 % GA in 1X PHEM and imaged on Zeiss LSM 880 upright single photon point scanning
952 confocal system with Quasar detector (32 spectral detection channels in the GaAsP detector
953 plus 2PMTs) and transmitted light detector, Airy scan detector for high-resolution imaging.
954 Cells were grown on 35mm glass bottom dishes with grids (Cat. No. P35G-1.5- 1.4-C- GRID)
955 and firstly brightfield images were made with Plan-Apochromat 10X/0.45 M27 objective to
956 save the coordinates of cells needed for the correlation with the respective TEM data.
957 Confocal and airy scan imaging was done using Plan-Apochromat 63x/1.4 oil DMC M27
958 objective, 405 nm laser diode, 458, 477, 488, 514 nm multiline integrated Argon laser and
959 594 nm integrated HeNe laser. Z-stack was acquired sequentially to get the whole 3D volume
960 of the cell and the image was further deconvolved using the inbuilt software. After Airy scan
961 imaging the sample was processed for TEM as described above. 70 nm sections were made
962 for the regions of saved coordinates from brightfield imaging, mounted on grids and imaged
963 on FEI Morgagni TEM (100kV) microscope.

964

965 **Immunogold labeling**

966 *Wdr35*^{-/-} MEFs expressing WDR35-EmGFP and ARL13B-mKate2 (**Table 2**) were serum-starved
967 for 4 h. MEF cells were grown on 6 mm sapphire disks (Wohlwend GmbH, Switzerland, 1292)
968 and high pressure frozen (EM ICE, Leica Microsystems, Germany). The frozen samples were
969 processed by freeze substitution in a Leica AFS2 temperature-controlling machine (Leica
970 Microsystems) using 0.01 % uranyl acetate (Polyscience Europe GmbH, 21446) and 4 % water

971 in glass distilled acetone (EMS, E10015) as freeze substitution medium and then embedded in
972 Lowicryl HM-20(Polysciences, 15924-1). 70 nm thick serial sections were sectioned on a Leica
973 Ultracut UCT ultramicrotome (Leica Microscopy systems). Sections were labelled with anti
974 GFP antibody, 1:20 (Abcam, ab6556- **Table 1**) followed by secondary goat anti rabbit
975 antibody coupled to 10-nm gold, 1:30 (BBI Solutions, Batch 008721 -Table 2). Before antibody
976 staining, grids were incubated twice section side for 10 min each on blocking buffer PBG (0.5
977 % BSA/ 0.1 % fish skin gelatin in PBS). Following blocking, grids were incubated for 1 h in
978 primary-Ab/PBG in a wet chamber, given five 2 min washes with PBG and incubate for 1 h in
979 secondary-Ab/PBG. Grids were washed five times for 2 min with PBG, followed by five 2 min
980 washes with PBS. Antibodies were subsequently fixed for 1 min 0.1 % glutaraldehyde/PBS,
981 followed by five 2 min washes with PBS and five 2 min washes with H₂O. After immunogold
982 labelling, the sections were stained with 1 % uranyl acetate (Polyscience Europe GmbH,
983 21446) in water for 8 min and 0.04 % lead citrate (EMS, 17800) for 5 min. The sections were
984 imaged using Tecnai 12 (Thermo Fisher Scientific, formerly FEI/ Philips) at 100kV with TVIPS
985 F214 and F416 cameras (TVIPS, Gauting, Germany).

986

987 **Image analysis and measurements**

988 All image processing was performed using FIJI (Schindelin et al., 2012). Macros for
989 quantification of PCM1 (RadialIntensityFromCentrosomes.ijm) and clathrin
990 (3DMeanIntensityfromUserDirectedPoints.ijm) can be found on GitHub
991 (https://github.com/IGMM-ImagingFacility/Quidwai2020_WDR35paper). To measure PCM1
992 intensity radially from the centrosomes, an average intensity projection of the z-stack was
993 obtained, and the gamma-tubulin signal was segmented using RenyiEntropy threshold and
994 the Analyze Particles tool to obtain masks of the centrosomes. The selections obtained from
995 the masks were enlarged using the "Make Band" function to create a band region of interest
996 (ROI). This was done by increasing in 1 μm increments until there were five bands. The
997 centrosome masks and the surrounding bands were measured on the PCM1 channel of the
998 average intensity projection image. To quantify clathrin intensity around the cilia base, a
999 point was manually selected as the center of the basal point. The user was blinded to file
1000 name and condition while quantification took place. This point was expanded 1 μm in each
1001 direction to create a shell of 2 μm diameter in x,y, and z. This shell was then measured using
1002 the 3D image suite in ImageJ (Ollion et al., 2013). Etomo and IMOD (Kremer et al., 1996) were
1003 used to reconstruct tomograms and manually segment tomograms respectively. These

1004 segmentations were used to create objects using the 3D Image suite in FIJI. The 3D centroids
1005 were obtained and the manually segmented ROI on the 2D slice that the 3D centroid was on
1006 was selected to move forward with. A 20 nm width band around this ROI was measured using
1007 the “Make Band” function. The integrated density of this band ROI was quantified as an
1008 indication of how electron dense the region around the user segmented vesicle is. 3D objects
1009 were measured using the 3D Image Suite. Statistical analyses were carried out in GraphPad
1010 Prism8.
1011

1012 **Table 1. List of primary antibodies**

1013

Antibody	Species	Source	Dilution	Fixation
ARL3	Rabbit	Proteintech 10961-1-AP	1:100 IF	PFA
ARL13B	Rabbit	Proteintech 17711-1-AP	1:100 IF	PFA
Ac α -tubulin	Mouse	Sigma T6793	1:1000 IF	PFA/GA
Ac α -tubulin	Rabbit	Abcam ab179484	1:1000 IF	PFA/GA
γ -tubulin	Mouse	Sigma T6557	1:100 IF	PFA
γ -tubulin	Rabbit	Abcam ab11317	1:100 IF	PFA
GFP	Mouse	Roche 11814460001	1:1000 IF 1:1000 WB	PFA
GFP	Rabbit	Abcam ab6556	1:1000 WB 1:20 ImEM	PFA
GFP	Rabbit	Santa Cruz sc-8334	1:5000 WB	-
His-tag	Mouse	GenScript A00186	3 μ g IP 1:2500 WB	-
IFT43	Rabbit	From Victor L. Ruiz-Perez, University of Madrid, Spain	1:200 IF 1:2000 WB	PFA
IFT81	Rabbit	Proteintech 11744-1-AP	1:200 IF 1:1000 WB	PFA
IFT88	Rabbit	Proteintech 13967-1AP Stock 0.23 μ g/ μ l	1:200 IF 1:1000 WB 3 μ g IP	PFA
IFT121	Rabbit	Custom made from Proteintech	1:50 WB Not for IF	-
IFT122	Rabbit	Proteintech 19304-1-AP	1:200 IF 1:1000 WB	PFA
IFT122	Rabbit	Aviva ARP 53817_P050	Not for IF 1:1000 WB	-
IFT139	Rabbit	Novus-NBP1-90416	1:1000 WB 1:200 IF	PFA
IFT140	Rabbit	Proteintech 17460-1-AP	1:200 IF 1:1000 WB 3 μ g IP	PFA
IFT144	Rabbit	Proteintech 13647-1-AP	1:200 IF 1:1000WB	PFA
MKS1	Rabbit	Proteintech 16206-1-AP	1:100 IF	MeOH
NPHP1	Mouse	640 from Greg Pazour, University of Massachusetts	1:100 IF	MeOH
PCM1	Rabbit	Proteintech 19856-1-AP	1:100 IF	MeOH
Rootletin	Goat	Santa Cruz sc-67828	1:100	MeOH
SNAP	Rabbit	New England Biolabs P9310S	1:300 IF	MeOH
Other reagents				
SiR-Tubulin	-	Spirochrome (SC002)	200 nM	Live cell imaging
SNAP-TMR	-	New England Biolabs SNAP- Cell TMR-STAR (S9105S)	1 μ M	Live cell imaging

1014 **PFA: Paraformaldehyde, GA: Glutaraldehyde, ImEM: Immuno Electron Microscopy, IF:**

1015 **Immunofluorescence, WB: Western Blot, IP: Immunoprecipitation, MeOH: Methanol.**

1016

1017 **Table 2. List of secondary antibodies**

1018

Antibody	Host	Source	Dilution	Application
ECL α -Mouse IgG, HRP-conjugated	Sheep	GE Healthcare NA931-1ML	1:10000	WB
ECL α -Mouse IgG, HRP-conjugated	Rabbit	Dako P0260	1:1000	SO
ECL α -Rabbit IgG, HRP-conjugated	Goat	GE Healthcare RPN4301	1:10000	WB
α -Rabbit Light-Chain specific HRP conjugated	Mouse	Millipore MAB201P	1:10000	WB
α -Rabbit IgG Light-Chain Specific mAb	Mouse	Cell Signalling Technology L57A3	1:10000	WB
Alexa 488, 594, 647 conjugated- α -Mouse	Donkey	Molecular Probes	1:500	IF
Alexa 488, 594, 647 conjugated- α -Rabbit	Donkey	Molecular Probes	1:500	IF
Alexa 488, 594, 647 conjugated- α -Goat	Donkey	Molecular Probes	1:500	IF
10nm gold conjugated- α -Rabbit (Batch 008721)	Goat	BBI Solutions EM GAR10/0.25	1:30	ImEM

1019 **ImEM: Immuno Electron Microscopy, IF: Immunofluorescence, SO: Lipid Strip Overlay WB:**
1020 **Western Blot,**

1021

1022

1023 **Table 3. List of plasmids**

1024

Plasmid	Source
Arl13b-mKate2	(Diggle et al., 2014)
ARL13B-EGFP	(Hori et al., 2008)
pEGFP-N1	Clontech 6085-1
Ift122-EGFP	(Qin et al., 2011)
PalmPalm-EGFP	(Williams et al., 2014)
MyrPalm-EGFP	(Williams et al., 2014)
pEGFP-mSmo	(Chen et al., 2002)
Wdr35-EmGFP	(Mill et al., 2011)

1025

1026 **Figure Legends**

1027

1028 **Figure 1. *Wdr35*^{-/-} and *Dync2h1*^{-/-} mutant cells have a drastic reduction in cilia length but have no**
 1029 **difference in the number of cilia.** (A) WT and mutant MEFs and those rescued by transiently
 1030 expressing WDR35-EmGFP serum starved for 24 h, fixed and stained with acetylated α tubulin (green)
 1031 and γ tubulin (magenta), nuclei (blue). Boxed regions are enlarged below, and arrows point at ciliary
 1032 axoneme stained for acetylated α tubulin. (B) Quantification of cilia length for acetylated α tubulin. n=
 1033 total number of cells from three different biological replicates (represented by different shapes).
 1034 Asterisk denotes significant p-value from t-test: (*, P < 0.05), (**, P < 0.01), (***, P < 0.001). (C)
 1035 Percentage of acetylated α tubulin positive ciliated cells. (D) 24 h serum starved WT and mutant MEFs
 1036 stained for nuclei (blue), acetylated α tubulin/ polyglutamylated tubulin (green), rootletin (cyan) and
 1037 transition zone proteins MKS1/NPHP-1 (magenta) show no difference in the localization of transition
 1038 zone protein MKS1 and NPHP-1. Grey scale enlarged regions are labeled green (G), magenta (M), and
 1039 cyan (C). (E) Schematic of intraflagellar transport (IFT) pathway in cilia.

1040

1041 **Figure 1- figure supplement 1. The organisation of centriolar satellites (CS) around *Wdr35*^{-/-} cilia is**
 1042 **not changed.** CS marker PCM1 intensity and localisation are unchanged in *Wdr35*^{+/+} and *Wdr35*^{-/-}
 1043 MEFs serum starved for 24 h to induce ciliogenesis and imaged (A) fixed after staining with
 1044 antibodies; PCM1 (magenta) and γ -tubulin (green). Nuclei are in blue. (B) Quantification of PCM1
 1045 intensity around the centrosome in concentric rings of 1 μ m around the basal body (γ -tubulin). n=50
 1046 cells (3 biological replicates each). (C) Imaged live after staining with SNAP-TMR dye for endogenous
 1047 SNAP tagged PCM1 (magenta) and microtubule marker SiR-tubulin (grey). These cells are also
 1048 expressing ARL13B-EGFP (green) (*Video 1*).

1049

1050 **Figure 2. *Wdr35*^{-/-} cilia exhibit retrograde transport defects of IFT-B, similar to *Dync2h1*^{-/-}, although**
 1051 **IFT-B complex assembly is unaffected.** (A) IFT-B (green) accumulates beyond the axoneme (Ac- α
 1052 tubulin, magenta) in *Wdr35* and *Dync2h1* mutant cilia from 24 h serum-starved and fixed MEFs. (B)
 1053 Length quantification shows IFT-B accumulates beyond acetylated α tubulin in significantly shorter
 1054 mutant cilia. n= total number of cells from three different biological replicates represented by
 1055 different shapes. Asterisk denotes significant p-value from t-test: (*, P < 0.05), (**, P < 0.01), (***, P <
 1056 0.001). Scale bars = 5 μ m. (C-D) Despite differences in localization, IFT88-IP/MS analysis of E11.5 WT
 1057 and *Wdr35*^{-/-} littermate embryos reveal no difference in the composition of the IFT-B complex.
 1058 Antibody highlights bait (IFT88) for IP. (C) Normalized LFQs to IFT88 intensity reveals no difference
 1059 between WT and *Wdr35*^{-/-} IFT-B complex composition. N= 4 embryos/genotype. (D) The number of
 1060 unique peptides identified in IP/MS.

1061

1062 **Figure 3. WDR35 is essential for the stability and recruitment of the IFT-A complex into cilia.** (A)
 1063 IP/MS data shows the stability of the IFT-A complex is disrupted in *Wdr35*^{-/-} lysates. N= 6

1064 embryos/genotype. Antibody highlights bait (IFT140) for IP. (B) Immunoblots confirm the non-core
 1065 IFT-A complex is unstable in *Wdr35* mutants. IFT43 runs close to the molecular weight of IgG, is shown
 1066 by an arrow as IFT43 band over the IgG band from IFT140 IP in WT. The corresponding band is absent
 1067 in *Wdr35* null samples. (C-D) Immunoblots for the total level of IFT-A subunits in E11.5 embryo lysates
 1068 show non-core components IFT139 and IFT43 to be missing in *Wdr35* mutants (C), quantified by
 1069 densitometry (D). N= biological replicates. Asterisk denotes significant p-value from t-test: (*, P <
 1070 0.05), (**, P < 0.01), (***, P < 0.001). (E) Inhibition of the proteasome by treatment with MG-132
 1071 rescues IFT43 stability in *Wdr35*^{-/-} MEFs. (F) MEFs serum starved for 24 h reveal a retrograde transport
 1072 defect in *Dync2h1*^{-/-} versus a failed recruitment of IFT-A proteins into *Wdr35*^{-/-} cilia. Cells are fixed and
 1073 stained for respective IFT-A (green) and γ and acetylated α tubulin (magenta). Arrowheads point at
 1074 cilia. Scale bars = 5 μ m. Due to a lack of specific immunoreagents, IFT122 signal is from transiently
 1075 expressed Ift122-GFP. All other panels represent endogenous signal detected by IF.

1076

1077 **Figure 3- figure supplement 1. WDR35 is essential for the stability and recruitment of the IFT-A**
 1078 **complex into cilia.** (A,B) Immunoblots for the total level of IFT-A subunits in MEF lysates show non-
 1079 core components IFT139 and IFT43 to be missing in *Wdr35* mutant cells (A), quantified by
 1080 densitometry (B). N= biological replicates. Asterisk denotes significant p-value from t-test: (*, P <
 1081 0.05), (**, P < 0.01), (***, P < 0.001). (C) Quantification of cilia length for acetylated α tubulin, and
 1082 IFT-As. n= total number of cells from three different biological replicates (represented by different
 1083 shapes). Asterisk denotes significant p-value from t-test: (*, P < 0.05), (**, P < 0.01), (***, P < 0.001).

1084

1085 **Figure 4. Membrane proteins fail to localise to *Wdr35*^{-/-} cilia.** (A) 24 h serum-starved WT, *Wdr35*^{-/-}
 1086 and *Dync2h1*^{-/-} MEFs stained for Smoothened (SMO), ARL13B and ARL3 (green), and acetylated α
 1087 tubulin (magenta) show failed localization of membrane proteins in *Wdr35*^{-/-} and retrograde transport
 1088 defect in *Dync2h1*^{-/-}. (B) Smoothened-EGFP and ARL13B-EGFP (green) expressing ciliated cells stained
 1089 with SiR-tubulin (magenta) show failed localization of exogenously expressed membrane proteins
 1090 inside mutant cilia (**Video 2**). Dashed arrows point at the enrichment of ARL13B on the membrane in
 1091 the mutant. (C) 24 h serum-starved cells expressing respective general lipidated GFP cargos (green)
 1092 and stained for SiR-tubulin show enrichment of lipidated GFP in WT cilia and failed localization in the
 1093 mutant. Arrowheads point at cilia in all the images. Scale bars = 5 μ m.

1094

1095 **Figure 5. IFT-A subunits have close sequence and structural similarity to α and β' COPI subunits and**
 1096 **can directly bind to phosphatidic acid *in vitro*.** (A) Clusters of IFT and COPI subunits generated from
 1097 the results of reciprocal sequence similarity searches with HHBlits using IFT144, IF140, IF122, and
 1098 WDR35 as initial search queries, suggest a very close similarity between a subset of IFT proteins and
 1099 the COPI α (COPA) and β' (COPB2) subunits. Clusters are color-coded according to protein structural
 1100 motifs with TPR repeat proteins (blue) and dual WD40 repeat and TPR repeat-containing proteins

1101 (magenta). Lines between clusters indicate sequence-based proximity. (B) The SDS-PAGE analysis of
 1102 the purified IFT139/121/His-GFP-43 after purification by Size Exclusion Chromatography (SEC). (C)
 1103 Lipid-strip overlay assay to detect binding between the IFT-A trimer shown in panel A and various
 1104 lipids as indicated in the schematics on the left-hand side of panel C. The IFT-A trimer displays strong
 1105 binding to phosphatidic acid (PA) and weaker binding to phosphatidylserine (PS) in the protein-lipid
 1106 overlay assay. Both are negatively charged (anionic) phosphoglycerates, whereas the trimer shows no
 1107 binding to neutral or inositol-based lipids. (D) Negative stain micrographs show that the IFT-A trimer
 1108 (IFT139/121/43) complex associates with liposomes (PE/PG/PA) but not with POPC-liposomes lacking
 1109 PA. The IFT121/43 dimer associates weakly with liposomes (PE/PG/PA). The particles of liposomes
 1110 with smooth surfaces are highlighted in black arrows, and liposomes with rough surface displaying
 1111 protein binding are highlighted in magenta arrows. Scale bar: 100 nm.

1112

1113 **Figure 5- figure supplement 1. IFT-A subunits have close sequence and structural similarity to α and**
 1114 **β' COPI subunits and can directly bind to phosphatidic acid *in vitro*.** (A) Structure prediction showed
 1115 IFT144, IFT140, IFT122, and WDR35 to have close structural similarity to COPI complex proteins α and
 1116 β' . 2.5 Å X-ray structure of β' (PDB:3mkq) and IFT-A proteins are shown with N-terminal WD40 repeat
 1117 (blue) and C-terminal TPR repeats (magenta). Sequence identity, similarity, and coverage between
 1118 COPI - β' and respective IFT-A proteins are shown in the table below. (B, C) Purified His-IFT43 or
 1119 hetero-dimeric His-IFT43/121 (right hand side) show no binding to any of the lipids spotted on the
 1120 strips (left hand side). Schematic (left panel B) outlines distribution of different lipids as indicated. As
 1121 a positive control, 1 μ l of His-IFT43 was spotted directly on the dry membranes presented in panels B
 1122 and C before blocking in 3 % BSA solution. (D) IFT-A trimer (His-IFT43/121/139) display binding to PA
 1123 demonstrating the requirement of IFT139 for lipid binding. IFT139 on its own is unstable *in vitro*.

1124

1125

1126 **Figure 6. Electron-dense vesicles are observed tracking between the Golgi and cilia base**
 1127 **in WT fibroblasts whereas a 'coat-less' vesicles accumulate around *Wdr35* mutant cilia.** The tilt
 1128 series of TEM samples were made from 24 h serum starved MEFs. Reconstructed tomograms are
 1129 color-coded to highlight the ciliary membrane (brown), ciliary sheath (orange), ciliary pocket (yellow),
 1130 basal body (purple), Golgi (green), electron-dense coated vesicles (magenta), and vesicles lacking
 1131 electron cloud (cyan). (A) Z-projections from 600 nm TEM serial tomograms of WT MEFs show a track
 1132 of electron-dense vesicles between the Golgi and cilia (**Video 3**). Arrows point at the path of vesicles
 1133 between the Golgi and cilia. The image in the left panel is segmented in the right panel. (B) Z-
 1134 projections from 300 nm tomograms from WT MEFs show electron-dense coated vesicles close to the
 1135 cilia base and along the length of the cilium (**Video 4**). Arrows point at coated vesicles near the cilium.
 1136 (C) Z-projections from 600 nm serial tomogram from *Wdr35*^{-/-} MEFs has a massive accumulation of
 1137 vesicles in a 2 μ m radius of the cilia base (cyan), and these vesicles lack a visible coat, or electron-
 dense cloud on them (**Video 5**). The length of cilia is drastically reduced, the ciliary membrane is

1138 wavy, and axoneme microtubules are broken in the mutant. (B and C) On left is the same Z-projection
 1139 in the upper panel segmented in the lower panel, and on the right is another Z-projection from the
 1140 same tomogram. Asterisk shows a coatless vesicle which fails to fuse with the ciliary sheath (see lower
 1141 left panel, 6C). Scale bars = 1 μm .

1142
 1143 **Figure 6- figure supplement 1. Vesicles with electron-dense coats are observed protruding/fusing**
 1144 **with the ciliary sheath in WT MEFs.** 24 h serum-starved WT MEFs are processed for TEM imaging.
 1145 TEM micrographs of 70 nm sections show vesicles fusing with or protruding from the ciliary sheath,
 1146 mostly at the ciliary pocket and less along the length. Vesicles are enlarged in the middle panel. Other
 1147 structures pointed by straight lines are actin filaments (Ac), microtubules (Mt), axoneme (Ax), ciliary
 1148 sheath (csh), ciliary membrane (cm), ciliary pocket (cp), basal body (bb), daughter centriole (dc). Scale
 1149 bars = 1 μm in the side panels and 100 nm in the middle panel.

1150
 1151 **Figure 6- figure supplement 2. Vesicles around cilia in *Wdr35*^{-/-} MEFs fail to fuse with ciliary pocket**
 1152 **or ciliary sheath.** After 24 h of serum starvation, the tilt series was made for 300 nm *Wdr35*^{-/-} TEM
 1153 samples. Z-projection from 900 nm serial tomograms is color-coded, highlighting the daughter
 1154 centriole (dark blue), basal body (purple), ciliary membrane (brown), ciliary sheath (orange), ciliary
 1155 pocket (yellow), basal foot (red), transition fibres (periwinkle), Y-links (white), axonemal microtubules
 1156 (magenta), Golgi (green), and vesicles around the cilia (cyan) (**Video 6**). Images in the left panel are
 1157 segmented in the right panel. Coatless vesicles (cyan) accumulate around mutant cilia but fail to fuse
 1158 with it. Transition zone (TZ) appeared intact in *Wdr35* mutants. Enlarged TZ in the last panel show no
 1159 disturbance in (9+0) microtubule doublet arrangement and Y-links connecting axoneme to cilia
 1160 membrane. The clathrin-coated vesicles that can be seen invaginating from the plasma membrane are
 1161 shown by arrows in the upper two left panels. Asterisk shows coatless vesicle which fails to fuse with
 1162 ciliary sheath. Scale bars = 1 μm .

1163
 1164 **Figure 6- figure supplement 3. Vesicle accumulation/fusion defect around cilia in *Wdr35*^{-/-} MEFs is**
 1165 **observed focally suggesting it is not a global membrane traffic defect.** Zoomed-out field of view (9.3
 1166 μm x 9.3 μm x 900 nm XYZ – **Video 7**) centered on the ciliated cell in the *Wdr35*^{-/-} TEM sample shown
 1167 in **Figure 6- figure supplement 2, Video 6-**, which also captures two adjacent *Wdr35*^{-/-} MEFs (yellow
 1168 and cyan). In all three cells, clathrin-like densely coated vesicles can be seen invaginating from the
 1169 plasma membrane are shown by arrows in **Video 7** (white arrows (central cell), black arrows (yellow
 1170 cell), cyan arrows (cyan cell)). In contrast, vesicles accumulating around mutant cilia are largely
 1171 coatless. Importantly, accumulation of coatless vesicles is not observed at a distance beyond 2 μm
 1172 from mutant cilia or close to or budding from cell membranes, suggesting this is not a defect in global
 1173 membrane traffic. Scale bars = 1 μm

1174
 1175

1176 **Figure 6- figure supplement 4. Retrograde dynein motor mutant has a different ciliary structure**
 1177 **defect than *Wdr35* mutants.** (A) 70 nm (cell 1) TEM micrograph and a Z-projection from a tomogram
 1178 of 300 nm WT MEF showing cilia ultrastructure; basal body (BB), transition zone (TZ), axoneme (Ax),
 1179 transition fibres (TF), and basal foot (BF). The arrowhead points at the IFT train entering cilia at the
 1180 ciliary pocket stacked between the axoneme and the ciliary membrane. (B) Z-projection from a serial
 1181 tomogram reconstructed from 600 nm thick section of *Wdr35*^{-/-} MEFs, the ciliary membrane is less
 1182 well-defined, and microtubules in the axoneme are disrupted, and periciliary vesicles accumulate
 1183 around cilia. (C) Z-projection from a serial tomogram of a 900 nm thick section (cell 1-**Video 8**) and
 1184 TEM micrograph of 70 nm section (cell 2) of *Dync2h1*^{-/-} MEFs has a striped pattern with a periodicity
 1185 of 40 nm apparent throughout the length of the cilium. Cell 2 is enlarged to show the same striped
 1186 pattern (magenta lines). The arrowhead points at the exosome budding from the tip of *Dync2h1*^{-/-}
 1187 cilium in cell1 (**Video 8**). Scale bars= 250 nm, except the bottom panel which is 500 nm.

1188

1189 **Figure 7. Vesicles clustering around *Wdr35*^{-/-} cilia lack electron dense decorations although electron-**
 1190 **dense clathrin coated vesicles are still observed budding from the mutant plasma membrane.** (A)
 1191 Zoomed-in views of periciliary vesicles observed in WT (zoomed- **Figure 7B, Video 4**), *Wdr35*^{-/-}
 1192 (zoomed- **Figure 7C, Video 5**), *Dync2h1*^{-/-} MEFs 24 h post-serum starvation show vesicles around WT
 1193 cilia are coated (magenta) and around *Wdr35*^{-/-} are coatless (blue). Very rare vesicles are observed
 1194 surrounding *Dync2h1*^{-/-} mutant cilia. (B) The average number of vesicles around cilia in control and
 1195 *Wdr35*^{-/-} cells, counted in a volume of 2 μm radius around cilia in TEM tomograms show ten times
 1196 more vesicles in *Wdr35*^{-/-} cells. N= number of whole-cell volume tomograms per genotype. (C) The
 1197 diameter of the periciliary vesicles shows a small, but significant increase in size between control and
 1198 *Wdr35*^{-/-}. n= number of vesicles. The paucity of vesicles around *Dync2h1*^{-/-} cilia prohibited
 1199 quantification. (D) 2D quantification of electron density around vesicles shows signal for control
 1200 vesicles is lower (darker) than mutant median (lighter) as determined by 20 nm ring outside all
 1201 annotated objects. (E) Zoomed-in images to highlight the difference in the electron dense cloud
 1202 surrounding periciliary vesicles in WT (**Video 4**) which are largely missing in *Wdr35*^{-/-} (**Video 6, 7**)
 1203 MEFs. Clathrin vesicles from the same mutant (**Video 6**) maintain their coat confirming missing
 1204 electron density on *Wdr35*^{-/-} periciliary vesicles is not a fixation artefact. Scale bars, A= 1 μm and E =
 1205 50 nm. N= number of cells examined. n= number of vesicles scored. Asterisk denotes significant p-
 1206 value from t-test: (*, P < 0.05), (**, P < 0.001), (***, P < 0.0001).

1207

1208 **Figure 7- figure supplement 1. Increased periciliary vesicles in *Wdr35* mutant cells are unlikely to be**
 1209 **clathrin-based as number and distribution of clathrin-positive foci remains unchanged.**

1210 (A) 3D projections of segmented vesicles from tomograms (top and side views) highlights the
 1211 accumulation of vesicles in mutants. (B) Examples of automated 20 nm band around segmented
 1212 objects for quantification in Figure 7D. (C) 24 h serum-starved cells stained for clathrin antibody

1213 (green) and acetylated α tubulin (left panel) and γ -tubulin (right panel) antibodies (magenta) do not
 1214 show any difference in the distribution of clathrin around cilia. Scale bars = 5 μ m. (D) No difference in
 1215 the mean intensity of clathrin foci quantified in a volume of 2 μ m radius around the base of cilia. n=
 1216 30 cells (3 biological replicates shown by different shapes each). Asterisk denotes significant p-value
 1217 from t-test: (*, $P < 0.05$), (**, $P < 0.001$), (***, $P < 0.0001$).

1218

1219 **Figure 8. WDR35 is sufficient to rescue cilia elongation and restore traffic of coated vesicles, which**
 1220 **are GFP-positive by correlative light and electron microscopy.** 4 h serum-starved *Wdr35*^{-/-} cells
 1221 rescued for ciliogenesis by expressing WDR35-EmGFP (green) and imaged first with Airyscan confocal
 1222 imaging followed by TEM imaging. ARL13B-mKATE (magenta) is used as a cilia marker. A1 and A2
 1223 represent two sequential Z-stacks from Airyscan confocal imaging. B1 and B2 represent TEM
 1224 sequential images of 70 nm sections of the same cell. Arrows point at WDR35 localizing close to the
 1225 cilia base, as shown by LM imaging, whilst arrowheads correspond to electron-dense vesicles shown
 1226 in Z=9 and Z=10 TEM images (B) The same two sections Z = 9 and Z = 10 enlarged in the last panel
 1227 show two rescued coated vesicles close to cilia. (C) Zoomed-out Z-section from 1200 nm thick TEM
 1228 tomogram of a different cell expressing *Wdr35*-EmGFP showing coated vesicle fusing with ciliary
 1229 pocket (arrowhead) left. Bottom, zoomed in view of two sections showing electron density on the
 1230 fusing vesicle (full series shown in **Figure 8 – figure supplement 1, Video 9**). (D) Quantification of
 1231 fusion figures observed between genotypes. N= number of cells. See **Figure 8- figure supplement 1,**
 1232 **Video 9**. Scale bars: A2 and B1 are 5 μ m, B2 and B are 500 nm and C is 500 nm (upper panel) and 100
 1233 nm (lower panel).

1234

1235 **Figure 8- figure supplement 1. WDR35 is sufficient to rescue cilia elongation and restore coated**
 1236 **vesicles fusion with the ciliary pocket.** (A) Zoomed out and (B) zoomed in select sections from 4 h
 1237 serum-starved *Wdr35*^{-/-} cell rescued for ciliogenesis by expressing WDR35-EmGFP and ARL13B-
 1238 mKATE, and processed for TEM. Arrowheads correspond to electron-dense vesicle fusing with the
 1239 ciliary pocket. Sections from 1200 nm thick TEM tomogram created from stitching together 300 nm
 1240 serial sections. Restoring WDR35 to mutant cells rescues ciliogenesis and the electron density on
 1241 vesicles in the periciliary region, and restores the fusion of these coated vesicles to the ciliary pocket
 1242 (arrowhead). See **Figure 8C** which illustrate sections and **Video 9** showing the tomogram through the
 1243 entire cilia, quantified in **Figure 8D**. Scale bars: A, B = 500 nm.

1244

1245 **Figure 8- figure supplement 2. WDR35 localizes on vesicles around the cilia and concentrates at the**
 1246 **ciliary pocket before entering the cilia by immunogold EM labeling.** (A, B) *Wdr35*^{-/-} cells transfected
 1247 with WDR35-EmGFP and *Arl13b*-mKate2, then serum starved for 4 h and processed for TEM. 70 nm
 1248 serial sections were subsequently stained with immunogold-tagged antibodies against GFP (anti-GFP).
 1249 Snapshots from 70 nm serial sections show WDR35 accumulating at the ciliary pocket (A''', B''''').

1250 Staining is also seen along the axoneme (A'', B'''), at the vesicles at the ciliary base (B') and what looks
 1251 like fusing or in close proximity to the ciliary sheath (A', B'', B'''). WDR35 epitopes were exposed to
 1252 antibodies directly on the surface 70 nm thick sections, which results in sparse but specific labeling of
 1253 GFP. Arrows point to GFP-gold particles. Magenta outline ROIs highlight putative vesicles. ImmunoEM
 1254 control shown in **Figure 8- figure supplement 3**. Scale bars = 500 nm.

1255
 1256 **Figure 8- figure supplement 3. WDR35 localization to vesicles around the cilia and ciliary pocket by**
 1257 **immunogold EM labelling is specific.** ImmunoEM control for **Figure 8- figure supplement 2** using two
 1258 controls. (A) Internal control for adjacent non-transfected control *Wdr35* mutant cell from the same
 1259 field of view as **Figure 8- figure supplement 2B**. In the absence of WDR35-EmGFP, *Wdr35* mutant cells
 1260 have rudimentary cilia (white arrowhead), coatless vesicles around cilia (magenta outlines), and no
 1261 anti-GFP immunogold labeling (black arrow). (B) Negative secondary only control. *Wdr35*-EmGFP
 1262 transfected mutant cells were grown under identical conditions and processed in parallel for
 1263 immunoEM as cells in **Figure 8- figure supplement 2** without addition of primary anti-GFP antibodies
 1264 demonstrating lack of immunogold labeling on any ciliary structures. Scale bars are 500 nm.

1265
 1266
 1267 **Figure 9. WDR35 and likely other IFT-As assist cargo transport of vesicles between the Golgi into**
 1268 **cilia at the stage of cilia elongation.** Diagrammatic representation of the TEM data showing vesicles
 1269 (green) with the WDR35-dependent coat (magenta halo) fusing and localizing around cilia in wild type
 1270 cells (insert A) and coatless vesicles clustering around cilia in *Wdr35*^{-/-} MEFs (insert C). Vesicles follow
 1271 a track between the Golgi and ciliary base in the WT cells but accumulate without fusing around cilia
 1272 in *Wdr35*^{-/-} cells. Upon fusion, any remnant IFT-A dependent coat would become a linear 'train' which
 1273 could assemble with cytosolic motors and IFT-B particles for ciliary import across the transition zone
 1274 (insert B). Without non-core IFT-As, IFT-A core components are restricted at the base of *Wdr35*^{-/-} cilia
 1275 whilst IFT-B proteins accumulate in short mutant cilia, without any enrichment of ciliary membrane
 1276 proteins indicating an arrest at the later stages of ciliogenesis during cilia elongation.

1277

1278 Video Legends

1279

1280 **Video 1. The organization of centriolar satellites is not disrupted in *Wdr35*^{-/-} mutants.**

1281 *Wdr35*^{+/+}; *Pcm1*^{SNAP/SNAP} and *Wdr35*^{-/-}; *Pcm1*^{SNAP/SNAP} MEFs electroporated with ARL13B-EGFP (green),
 1282 serum-starved for 24 h and stained for SiR-tubulin (grey) and SNAP-TMR (magenta) and imaged live
 1283 on LEICA SP5 microscope using a 63X, 1.4 oil immersion objective. The video is compiled as 5 fps.
 1284 PCM-1 density around cilia is not altered in the absence of WDR35. (**Related to Figure 1- figure**
 1285 **supplement 1C**).

1286

1287 **Video 2. Cilia specific membrane-associated cargo (A) ARL13B, and membrane-integrated cargo (B)**
1288 **SMO fail to localize in *Wdr35*^{-/-} cilia.** WT and *Wdr35*^{-/-} MEFs expressing ARL13B-EGFP (green) and
1289 Smoothed-EGFP (green), serum-starved for 24 h, stained with SiR-tubulin and imaged live on LEICA
1290 SP5 microscope using a 63X, 1.4 oil immersion objective. The video is compiled as 5 fps. **(Related to**
1291 **Figure 4).**

1292
1293 **Video 3. Track of electron-dense vesicles are present between Golgi and cilia in control mouse**
1294 **fibroblast.** 24 h serum-starved cells are prepared for EM analysis by plastic embedding and making
1295 300 nm thick sections. Tomogram reconstructed from two 300 nm sections stitched together shows
1296 the presence of electron-dense vesicles between the Golgi and cilia. The 3D volume shown in the
1297 upper half is segmented in the lower half of the video. Daughter centriole (blue), basal body (purple),
1298 ciliary membrane (brown), ciliary sheath (orange), ciliary pocket (yellow), Golgi (green), and vesicles
1299 with dense electron clouds are shown in magenta. Arrows are pointing at the track of vesicles
1300 between the Golgi and cilia. **(Related to Figure 6A).**

1301
1302 **Video 4. Electron-dense vesicles are observed around the base of cilia in control mouse fibroblasts.**
1303 24 h serum-starved cells are prepared for EM analysis by plastic embedding and making 300 nm thick
1304 sections. Tomogram reconstructed from the 300 nm thick cell section shows electron-dense vesicles
1305 clustering at the base of cilia. The 3D volume shown in the upper half is segmented in the lower half
1306 of the Video. The basal body (purple), ciliary membrane (brown), ciliary sheath (orange), ciliary pocket
1307 (yellow), Golgi (green), and vesicles with dense electron clouds are shown in magenta. **(Related to**
1308 **Figure 6B).**

1309
1310 **Video 5. In *Wdr35*^{-/-} fibroblasts, an accumulation of small coatless vesicles are present around short**
1311 **cilia.** 24 h serum-starved cells are prepared for EM analysis by plastic embedding and making 300 nm
1312 thick sections. Tomogram reconstructed from tilt series of two 300 nm thick cell sections and stitched
1313 together shows ten times more vesicles randomly clustering around cilia in the mutant. The 3D
1314 volume shown in the upper half is segmented in the lower half of the Video. The basal body (purple),
1315 ciliary membrane (brown), ciliary sheath (orange), ciliary pocket (yellow), Golgi (green), and coatless
1316 vesicles around the cilia is shown in cyan. The ciliary membrane is slack compared to WT MEFs and
1317 axonemal microtubules are poorly polymerized. **(Related to Figure 6C).**

1318
1319 **Video 6. In *Wdr35*^{-/-} fibroblasts, periciliary vesicles fail to fuse with ciliary pocket or ciliary sheath.**
1320 24 h serum-starved cells are prepared for EM analysis by plastic embedding and making 300 nm thick
1321 sections. Tomogram reconstructed from tilt series of three 300 nm thick cell sections and stitched
1322 together shows the transition zone is unaltered in the mutant. Vesicles lacking any electron dense
1323 cloud cluster around mutant cilia, but fail to fuse with ciliary sheath or ciliary pocket. The 3D volume

1324 shown in the upper half is segmented in the lower half of the Video. Daughter centriole (dark blue),
1325 basal body (purple), ciliary membrane (brown), ciliary sheath (orange), ciliary pocket (yellow), basal
1326 foot/ subdistal appendage (red), transition fibres/ distal appendage (orchid), Y-Links (white), Golgi
1327 (green), and vesicles lacking any electron dense cloud present around cilia (cyan). Arrows are pointing
1328 at the clathrin-coated vesicles budding from the cell plasma membrane. (Related to **Figure 6- figure**
1329 **supplement 2**).

1330

1331 **Video 7. In *Wdr35*^{-/-} fibroblasts, preciliary vesicles fail to fuse with ciliary pocket or ciliary sheath.**

1332 Zoomed out view of tomograms from field of view in **Video 6** of 24 h serum-starved cells prepared for
1333 EM analysis by plastic embedding and making 300 nm thick sections, without segmentation. (Related
1334 to **Figure 6- figure supplement 3**). Zoomed out view shows two more mutant neighbouring cells with
1335 clathrin coated vesicles endocytosing from the cell membrane pointed by arrows. Three such vesicles
1336 are present in central cell pointed by white arrow, four in the cell at the top pointed by black arrows,
1337 and one in the cell at the right pointed by cyan arrow. This shows other type of vesicles away from
1338 cilia retain their coats. *Wdr35* mutant cilia have coatless vesicles accumulated close to the
1339 rudimentary cilia and not elsewhere in the cell showing the defect is not in the global membrane
1340 protein transport from the cell membrane.

1341

1342 **Video 8. *Dync2h1*^{-/-} cilia lack both coated as well as coatless vesicles at the cilia base, whilst**

1343 **ectosomes are seen budding from the tip.** 24 h serum-starved *Dync2h1*^{-/-} MEFs are prepared for EM
1344 analysis by plastic embedding and making 300 nm thick sections. Tomogram reconstructed from the
1345 tilt series of three 300 nm sections and stitched together shows a sturdy ciliary membrane, well-
1346 polymerized microtubules in the axoneme, almost no coated or coatless vesicles at the cilia base, and
1347 ectosome vesicles could be seen budding from the tip of cilia. A 40 nm striped pattern could be seen
1348 present throughout the length of cilia. Arrows point at the basal body (purple), cilia (magenta), and
1349 ectosome (green). This is also an example of the rare event of having two cilia in the same ciliary
1350 sheath. (Related to **Figure 6- figure supplement 4C- Cell1**).

1351

1352 **Video 9. WDR35 is sufficient to rescue cilia elongation and restore fusion of coated vesicles.**

1353 Zoomed in and stitched sections from 1200 nm thick TEM tomogram from 300 nm serial sections. 4 h
1354 serum-starved *Wdr35*^{-/-} cell rescued for ciliogenesis by expressing WDR35-EmGFP and processed for
1355 TEM. The cells also express ARL13B-mKATE as a cilia marker to aid identification. Arrowheads
1356 correspond to electron-dense vesicle fusing with the ciliary pocket. Restoring WDR35 to mutant cells
1357 rescues vesicle fusion, electron density on some vesicles in the periciliary region and rescues
1358 ciliogenesis. See **Figure 8C** and **Figure 8- figure supplement 1**, which illustrate these features,
1359 quantified in **Figure 8D**. Scale bars: 500 nm.

1360

1361 Acknowledgements

1362

1363 We thank the IGC Advanced Imaging Resource and the IGC Mass Spectrometry facility (in
 1364 particular Jimi Wills and Alexander von Kriegsheim). We thank the Electron Microscopy
 1365 Facility (in particular Tobias Fürstenhaupt, Michaela Wilsch-Bräuniger and Daniela Vorkel)
 1366 and the Light Microscope Facility from the Services and Facilities of the Max Planck Institute
 1367 of Molecular Cell Biology and Genetics, Dresden (in particular Sebastian Bundschuh). We
 1368 thank Rick Kahn, Toby Hurd, Ian Jackson and Patricia Yeyati for helpful discussions and
 1369 comments on the manuscript. We are grateful to Greg Pazour (UMass) and Victor Ruiz (UAM)
 1370 for sharing custom antibodies. We thank Jonathan Eggenschwiler (UGA) for Ift122::GFP and
 1371 Kenji Kontani (UOT) for the ARL13B-EGFP used in this study, as well Philip Beachy for pEGFP-
 1372 mSmo (Addgene plasmid # 25395 ; <http://n2t.net/addgene:25395> ; RRID:Addgene_25395).

1373

1374 Source Data

1375 **Figure 1- source data 1. Full data points and stats test of cilia length for Figure 1B.**

1376 **Figure 2- source data 1. Full data points and stats test IFT-B and cilia length Figure 2B.**

1377 **Figure 3- source data 1. Full immunoblots labelled and unlabelled for Figure 3B, 3C and 3E.**

1378 **Figure 3- figure supplement 1 source data 1. Full immunoblots labelled and unlabelled for**
 1379 **Figure 3- figure supplement 1A as well as full data points and stats test IFT-A and cilia**
 1380 **length for Figure 3- figure supplement 1B-D.**

1381 **Figure 5- source data 1. Full immunoblots labelled and unlabelled for Figure 5B and Figure**
 1382 **5- figure supplement 1A.**

1383 **Figure 7- source data 1. Full data points and stats test for size of vesicles Figure 7B-C, mean**
 1384 **clathrin intensity for Figure 7- figure supplement 1D, and integrated density Figure 7D as**
 1385 **well as ROI files used for calculations.**

1386

1387 Declaration of interests

1388

1389 The authors have declared no competing interests.

1390

1391 References

1392

1393

1394 Agbu, S.O., Liang, Y., Liu, A., Anderson, K.V., 2018. The small GTPase RSG1 controls a
 1395 final step in primary cilia initiation. *J. Cell Biol.* 217, 413–427.

1396 doi:10.1083/jcb.201604048

1397 Alkanderi, S., Molinari, E., Shaheen, R., Elmaghloob, Y., Stephen, L.A., Sammut, V.,
 1398 Ramsbottom, S.A., Srivastava, S., Cairns, G., Edwards, N., Rice, S.J., Ewida, N.,
 1399 Alhashem, A., White, K., Miles, C.G., Steel, D.H., Alkuraya, F.S., Ismail, S., Sayer,
 1400 J.A., 2018. ARL3 mutations cause joubert syndrome by disrupting ciliary protein
 1401 composition. *Am. J. Hum. Genet.* 103, 612–620. doi:10.1016/j.ajhg.2018.08.015

1402 Arisz, S.A., Munnik, T., 2011. The salt stress-induced LPA response in *Chlamydomonas* is
 1403 produced via PLA2 hydrolysis of DGK-generated phosphatidic acid [S]. *Journal of*

- 1404 lipid research.
- 1405 Avidor-Reiss, T., Maer, A.M., Koundakjian, E., Polyanovsky, A., Keil, T., Subramaniam, S.,
1406 Zuker, C.S., 2004. Decoding cilia function: defining specialized genes required for
1407 compartmentalized cilia biogenesis. *Cell* 117, 527–539. doi:10.1016/s0092-
1408 8674(04)00412-x
- 1409 Bae, Y.-K., Qin, H., Knobel, K.M., Hu, J., Rosenbaum, J.L., Barr, M.M., 2006. General and
1410 cell-type specific mechanisms target TRPP2/PKD-2 to cilia. *Development* 133, 3859–
1411 3870. doi:10.1242/dev.02555
- 1412 Baron Gaillard, C.L., Pallesi-Pocachard, E., Massey-Harroche, D., Richard, F., Arsanto, J.-P.,
1413 Chauvin, J.-P., Lecine, P., Krämer, H., Borg, J.-P., Le Bivic, A., 2011. Hook2 is
1414 involved in the morphogenesis of the primary cilium. *Mol. Biol. Cell* 22, 4549–4562.
1415 doi:10.1091/mbc.E11-05-0405
- 1416 Behal, R.H., Cole, D.G., 2013. Analysis of interactions between intraflagellar transport
1417 proteins. *Meth. Enzymol.* 524, 171–194. doi:10.1016/B978-0-12-397945-2.00010-X
- 1418 Behal, R.H., Miller, M.S., Qin, H., Lucker, B.F., Jones, A., Cole, D.G., 2012. Subunit
1419 interactions and organization of the *Chlamydomonas reinhardtii* intraflagellar transport
1420 complex A proteins. *J. Biol. Chem.* 287, 11689–11703. doi:10.1074/jbc.M111.287102
- 1421 Bhogaraju, S., Taschner, M., Morawetz, M., Basquin, C., Lorentzen, E., 2011. Crystal
1422 structure of the intraflagellar transport complex 25/27. *EMBO J.* 30, 1907–1918.
1423 doi:10.1038/emboj.2011.110
- 1424 Blacque, O.E., Li, C., Inglis, P.N., Esmail, M.A., Ou, G., Mah, A.K., Baillie, D.L., Scholey,
1425 J.M., Leroux, M.R., 2006. The WD repeat-containing protein IFTA-1 is required for
1426 retrograde intraflagellar transport. *Mol. Biol. Cell* 17, 5053–5062.
1427 doi:10.1091/mbc.e06-06-0571
- 1428 Blacque, O.E., Scheidel, N., Kuhns, S., 2018. Rab GTPases in cilium formation and function.
1429 *Small GTPases* 9, 76–94. doi:10.1080/21541248.2017.1353847
- 1430 Boehlke, C., Bashkurov, M., Buescher, A., Krick, T., John, A.-K., Nitschke, R., Walz, G.,
1431 Kuehn, E.W., 2010. Differential role of Rab proteins in ciliary trafficking: Rab23
1432 regulates smoothed levels. *J. Cell Sci.* 123, 1460–1467. doi:10.1242/jcs.058883
- 1433 Bonifacino, J.S., Glick, B.S., 2004. The mechanisms of vesicle budding and fusion. *Cell* 116,
1434 153–166. doi:10.1016/s0092-8674(03)01079-1
- 1435 Brear, A.G., Yoon, J., Wojtyniak, M., Sengupta, P., 2014. Diverse cell type-specific
1436 mechanisms localize G protein-coupled receptors to *Caenorhabditis elegans* sensory
1437 cilia. *Genetics* 197, 667–684. doi:10.1534/genetics.114.161349
- 1438 Cantagrel, V., Silhavy, J.L., Bielas, S.L., Swistun, D., Marsh, S.E., Bertrand, J.Y., Audollent,
1439 S., Attié-Bitach, T., Holden, K.R., Dobyns, W.B., Traver, D., Al-Gazali, L., Ali, B.R.,
1440 Lindner, T.H., Caspary, T., Otto, E.A., Hildebrandt, F., Glass, I.A., Logan, C.V.,
1441 Johnson, C.A., Bennett, C., Brancati, F., International Joubert Syndrome Related
1442 Disorders Study Group, Valente, E.M., Woods, C.G., Gleeson, J.G., 2008. Mutations
1443 in the cilia gene *ARL13B* lead to the classical form of Joubert syndrome. *Am. J. Hum.*
1444 *Genet.* 83, 170–179. doi:10.1016/j.ajhg.2008.06.023
- 1445 Cao, M., Ning, J., Hernandez-Lara, C.I., Belzile, O., Wang, Q., Dutcher, S.K., Liu, Y., Snell,
1446 W.J., 2015. Uni-directional ciliary membrane protein trafficking by a cytoplasmic
1447 retrograde IFT motor and ciliary ectosome shedding. *Elife* 4. doi:10.7554/eLife.05242
- 1448 Caparrós-Martín, J.A., De Luca, A., Cartault, F., Aglan, M., Temtamy, S., Otaify, G.A.,
1449 Mehrez, M., Valencia, M., Vázquez, L., Alessandri, J.-L., Nevado, J., Rueda-Arenas,
1450 I., Heath, K.E., Digilio, M.C., Dallapiccola, B., Goodship, J.A., Mill, P., Lapunzina, P.,
1451 Ruiz-Perez, V.L., 2015. Specific variants in *WDR35* cause a distinctive form of Ellis-
1452 van Creveld syndrome by disrupting the recruitment of the EvC complex and SMO
1453 into the cilium. *Hum. Mol. Genet.* 24, 4126–4137. doi:10.1093/hmg/ddv152
- 1454 Cevik, S., Hori, Y., Kaplan, O.I., Kida, K., Toivenon, T., Foley-Fisher, C., Cottell, D., Katada,
1455 T., Kontani, K., Blacque, O.E., 2010. Joubert syndrome *Arl13b* functions at ciliary
1456 membranes and stabilizes protein transport in *Caenorhabditis elegans*. *J. Cell Biol.* 188,

- 1457 953–969. doi:10.1083/jcb.200908133
- 1458 Chen, J.K., Taipale, J., Cooper, M.K., Beachy, P.A., 2002. Inhibition of Hedgehog signaling
1459 by direct binding of cyclopamine to Smoothened. *Genes Dev.* 16, 2743–2748.
1460 doi:10.1101/gad.1025302
- 1461 Chou, H.-T., Apelt, L., Farrell, D.P., White, S.R., Woodsmith, J., Svetlov, V., Goldstein, J.S.,
1462 Nager, A.R., Li, Z., Muller, J., Dollfus, H., Nudler, E., Stelzl, U., DiMaio, F., Nachury,
1463 M.V., Walz, T., 2019. The molecular architecture of native BBSome obtained by an
1464 integrated structural approach. *Structure* 27, 1384–1394.e4.
1465 doi:10.1016/j.str.2019.06.006
- 1466 Clement, C.A., Ajbro, K.D., Koefoed, K., Vestergaard, M.L., Veland, I.R., Henriques de
1467 Jesus, M.P.R., Pedersen, L.B., Benmerah, A., Andersen, C.Y., Larsen, L.A.,
1468 Christensen, S.T., 2013. TGF- β signaling is associated with endocytosis at the pocket
1469 region of the primary cilium. *Cell Rep.* 3, 1806–1814.
1470 doi:10.1016/j.celrep.2013.05.020
- 1471 Cole, D.G., 2009. Intraflagellar Transport, in: *The Chlamydomonas Sourcebook*. Elsevier, pp.
1472 71–113. doi:10.1016/B978-0-12-370873-1.00041-1
- 1473 Criswell, P.S., Ostrowski, L.E., Asai, D.J., 1996. A novel cytoplasmic dynein heavy chain:
1474 expression of DHC1b in mammalian ciliated epithelial cells. *J. Cell Sci.* 109 (Pt 7),
1475 1891–1898.
- 1476 Diggle, C.P., Moore, D.J., Mali, G., zur Lage, P., Ait-Lounis, A., Schmidts, M., Shoemark, A.,
1477 Garcia Munoz, A., Halachev, M.R., Gautier, P., Yeyati, P.L., Bonthron, D.T., Carr,
1478 I.M., Hayward, B., Markham, A.F., Hope, J.E., von Kriegsheim, A., Mitchison, H.M.,
1479 Jackson, I.J., Durand, B., Reith, W., Sheridan, E., Jarman, A.P., Mill, P., 2014.
1480 HEATR2 plays a conserved role in assembly of the ciliary motile apparatus. *PLoS*
1481 *Genet.* 10, e1004577. doi:10.1371/journal.pgen.1004577
- 1482 Dodonova, S.O., Aderhold, P., Kopp, J., Ganeva, I., Röhling, S., Hagen, W.J.H., Sinning, I.,
1483 Wieland, F., Briggs, J.A.G., 2017. 9Å structure of the COPI coat reveals that the Arf1
1484 GTPase occupies two contrasting molecular environments. *Elife* 6.
1485 doi:10.7554/eLife.26691
- 1486 Domire, J.S., Green, J.A., Lee, K.G., Johnson, A.D., Askwith, C.C., Mykytyn, K., 2011.
1487 Dopamine receptor 1 localizes to neuronal cilia in a dynamic process that requires the
1488 Bardet-Biedl syndrome proteins. *Cell Mol. Life Sci.* 68, 2951–2960.
1489 doi:10.1007/s00018-010-0603-4
- 1490 Duran, I., Taylor, S.P., Zhang, W., Martin, J., Qureshi, F., Jacques, S.M., Wallerstein, R.,
1491 Lachman, R.S., Nickerson, D.A., Bamshad, M., Cohn, D.H., Krakow, D., 2017.
1492 Mutations in IFT-A satellite core component genes IFT43 and IFT121 produce short
1493 rib polydactyly syndrome with distinctive campomelia. *Cilia* 6, 7. doi:10.1186/s13630-
1494 017-0051-y
- 1495 Dwyer, N.D., Troemel, E.R., Sengupta, P., Bargmann, C.I., 1998. Odorant receptor
1496 localization to olfactory cilia is mediated by ODR-4, a novel membrane-associated
1497 protein. *Cell* 93, 455–466. doi:10.1016/s0092-8674(00)81173-3
- 1498 Efimenko, E., Blacque, O.E., Ou, G., Haycraft, C.J., Yoder, B.K., Scholey, J.M., Leroux,
1499 M.R., Swoboda, P., 2006. *Caenorhabditis elegans* DYF-2, an orthologue of human
1500 WDR19, is a component of the intraflagellar transport machinery in sensory cilia. *Mol.*
1501 *Biol. Cell* 17, 4801–4811. doi:10.1091/mbc.e06-04-0260
- 1502 Eguether, T., San Agustin, J.T., Keady, B.T., Jonassen, J.A., Liang, Y., Francis, R., Tobita, K.,
1503 Johnson, C.A., Abdelhamed, Z.A., Lo, C.W., Pazour, G.J., 2014. IFT27 links the
1504 BBSome to IFT for maintenance of the ciliary signaling compartment. *Dev. Cell* 31,
1505 279–290. doi:10.1016/j.devcel.2014.09.011
- 1506 Fan, Y., Esmail, M.A., Ansley, S.J., Blacque, O.E., Boroevich, K., Ross, A.J., Moore, S.J.,
1507 Badano, J.L., May-Simera, H., Compton, D.S., Green, J.S., Lewis, R.A., van Haelst,
1508 M.M., Parfrey, P.S., Baillie, D.L., Beales, P.L., Katsanis, N., Davidson, W.S., Leroux,
1509 M.R., 2004. Mutations in a member of the Ras superfamily of small GTP-binding

- 1510 proteins causes Bardet-Biedl syndrome. *Nat. Genet.* 36, 989–993. doi:10.1038/ng1414
- 1511 Farmer, T., Xie, S., Naslavsky, N., Stöckli, J., James, D.E., Caplan, S., 2020. Defining the
1512 protein and lipid constituents of tubular recycling endosomes. *J. Biol. Chem.*
1513 doi:10.1074/jbc.RA120.015992
- 1514 Field, M.C., Sali, A., Rout, M.P., 2011. Evolution: On a bender--BARs, ESCRTs, COPs, and
1515 finally getting your coat. *J. Cell Biol.* 193, 963–972. doi:10.1083/jcb.201102042
- 1516 Finetti, F., Paccani, S.R., Riparbelli, M.G., Giacomello, E., Perinetti, G., Pazour, G.J.,
1517 Rosenbaum, J.L., Baldari, C.T., 2009. Intraflagellar transport is required for polarized
1518 recycling of the TCR/CD3 complex to the immune synapse. *Nat. Cell Biol.* 11, 1332–
1519 1339. doi:10.1038/ncb1977
- 1520 Follit, J.A., San Agustin, J.T., Jonassen, J.A., Huang, T., Rivera-Perez, J.A., Tremblay, K.D.,
1521 Pazour, G.J., 2014. Arf4 is required for Mammalian development but dispensable for
1522 ciliary assembly. *PLoS Genet.* 10, e1004170. doi:10.1371/journal.pgen.1004170
- 1523 Follit, J.A., San Agustin, J.T., Xu, F., Jonassen, J.A., Samtani, R., Lo, C.W., Pazour, G.J.,
1524 2008. The Golgin GMAP210/TRIP11 anchors IFT20 to the Golgi complex. *PLoS*
1525 *Genet.* 4, e1000315. doi:10.1371/journal.pgen.1000315
- 1526 Follit, J.A., Tuft, R.A., Fogarty, K.E., Pazour, G.J., 2006. The intraflagellar transport protein
1527 IFT20 is associated with the Golgi complex and is required for cilia assembly. *Mol.*
1528 *Biol. Cell* 17, 3781–3792. doi:10.1091/mbc.E06-02-0133
- 1529 Fölsch, H., Ohno, H., Bonifacino, J.S., Mellman, I., 1999. A novel clathrin adaptor complex
1530 mediates basolateral targeting in polarized epithelial cells. *Cell* 99, 189–198.
1531 doi:10.1016/s0092-8674(00)81650-5
- 1532 Fu, W., Wang, L., Kim, S., Li, J., Dynlacht, B.D., 2016. Role for the IFT-A Complex in
1533 Selective Transport to the Primary Cilium. *Cell Rep.* 17, 1505–1517.
1534 doi:10.1016/j.celrep.2016.10.018
- 1535 Funabashi, T., Katoh, Y., Michisaka, S., Terada, M., Sugawa, M., Nakayama, K., 2017.
1536 Ciliary entry of KIF17 is dependent on its binding to the IFT-B complex via IFT46-
1537 IFT56 as well as on its nuclear localization signal. *Mol. Biol. Cell* 28, 624–633.
1538 doi:10.1091/mbc.E16-09-0648
- 1539 Futter, C.E., Gibson, A., Allchin, E.H., Maxwell, S., Ruddock, L.J., Odorizzi, G., Domingo,
1540 D., Trowbridge, I.S., Hopkins, C.R., 1998. In polarized MDCK cells basolateral
1541 vesicles arise from clathrin-gamma-adaptin-coated domains on endosomal tubules. *J.*
1542 *Cell Biol.* 141, 611–623.
- 1543 Gerondopoulos, A., Strutt, H., Stevenson, N.L., Sobajima, T., Levine, T.P., Stephens, D.J.,
1544 Strutt, D., Barr, F.A., 2019. Planar cell polarity effector proteins intuned and fuzzy
1545 form a rab23 GEF complex. *Curr. Biol.* 29, 3323–3330.e8.
1546 doi:10.1016/j.cub.2019.07.090
- 1547 Goedhart, J., Gadella, T.W.J., 2004. Photolysis of caged phosphatidic acid induces flagellar
1548 excision in *Chlamydomonas*. *Biochemistry* 43, 4263–4271. doi:10.1021/bi0351460
- 1549 Gotthardt, K., Lokaj, M., Koerner, C., Falk, N., Gießl, A., Wittinghofer, A., 2015. A G-protein
1550 activation cascade from Arl13B to Arl3 and implications for ciliary targeting of
1551 lipidated proteins. *Elife* 4. doi:10.7554/eLife.11859
- 1552 Graser, S., Stierhof, Y.-D., Lavoie, S.B., Gassner, O.S., Lamla, S., Le Clech, M., Nigg, E.A.,
1553 2007. Cep164, a novel centriole appendage protein required for primary cilium
1554 formation. *J. Cell Biol.* 179, 321–330. doi:10.1083/jcb.200707181
- 1555 Hirano, T., Katoh, Y., Nakayama, K., 2017. Intraflagellar transport-A complex mediates
1556 ciliary entry and retrograde trafficking of ciliary G protein-coupled receptors. *Mol.*
1557 *Biol. Cell* 28, 429–439. doi:10.1091/mbc.E16-11-0813
- 1558 Hoffmeister, H., Babinger, K., Gürster, S., Cedzich, A., Meese, C., Schadendorf, K., Osten, L.,
1559 de Vries, U., Rasclé, A., Witzgall, R., 2011. Polycystin-2 takes different routes to the
1560 somatic and ciliary plasma membrane. *J. Cell Biol.* 192, 631–645.
1561 doi:10.1083/jcb.201007050
- 1562 Hori, Y., Kobayashi, T., Kikko, Y., Kontani, K., Katada, T., 2008. Domain architecture of the

- 1563 atypical Arf-family GTPase Arl13b involved in cilia formation. *Biochem. Biophys.*
 1564 *Res. Commun.* 373, 119–124. doi:10.1016/j.bbrc.2008.06.001
- 1565 Huangfu, D., Anderson, K.V., 2005. Cilia and Hedgehog responsiveness in the mouse. *Proc.*
 1566 *Natl. Acad. Sci. USA* 102, 11325–11330. doi:10.1073/pnas.0505328102
- 1567 Iomini, C., Li, L., Esparza, J.M., Dutcher, S.K., 2009. Retrograde intraflagellar transport
 1568 mutants identify complex A proteins with multiple genetic interactions in
 1569 *Chlamydomonas reinhardtii*. *Genetics* 183, 885–896. doi:10.1534/genetics.109.101915
- 1570 Jaiswal, J.K., Rivera, V.M., Simon, S.M., 2009. Exocytosis of post-Golgi vesicles is regulated
 1571 by components of the endocytic machinery. *Cell* 137, 1308–1319.
 1572 doi:10.1016/j.cell.2009.04.064
- 1573 Jékely, G., Arendt, D., 2006. Evolution of intraflagellar transport from coated vesicles and
 1574 autogenous origin of the eukaryotic cilium. *Bioessays* 28, 191–198.
 1575 doi:10.1002/bies.20369
- 1576 Jensen, V.L., Bialas, N.J., Bishop-Hurley, S.L., Molday, L.L., Kida, K., Nguyen, P.A.T.,
 1577 Blacque, O.E., Molday, R.S., Leroux, M.R., Riddle, D.L., 2010. Localization of a
 1578 guanylyl cyclase to chemosensory cilia requires the novel ciliary MYND domain
 1579 protein DAF-25. *PLoS Genet.* 6, e1001199. doi:10.1371/journal.pgen.1001199
- 1580 Jin, H., White, S.R., Shida, T., Schulz, S., Aguiar, M., Gygi, S.P., Bazan, J.F., Nachury, M.V.,
 1581 2010. The conserved Bardet-Biedl syndrome proteins assemble a coat that traffics
 1582 membrane proteins to cilia. *Cell* 141, 1208–1219. doi:10.1016/j.cell.2010.05.015
- 1583 Jonassen, J.A., SanAgustin, J., Baker, S.P., Pazour, G.J., 2012. Disruption of IFT complex A
 1584 causes cystic kidneys without mitotic spindle misorientation. *J. Am. Soc. Nephrol.* 23,
 1585 641–651. doi:10.1681/ASN.2011080829
- 1586 Joo, K., Kim, C.G., Lee, M.-S., Moon, H.-Y., Lee, S.-H., Kim, M.J., Kweon, H.-S., Park, W.-
 1587 Y., Kim, C.-H., Gleeson, J.G., Kim, J., 2013. CCDC41 is required for ciliary vesicle
 1588 docking to the mother centriole. *Proc. Natl. Acad. Sci. USA* 110, 5987–5992.
 1589 doi:10.1073/pnas.1220927110
- 1590 Jordan, M.A., Diener, D.R., Stepanek, L., Pigino, G., 2018. The cryo-EM structure of
 1591 intraflagellar transport trains reveals how dynein is inactivated to ensure unidirectional
 1592 anterograde movement in cilia. *Nat. Cell Biol.* 20, 1250–1255. doi:10.1038/s41556-
 1593 018-0213-1
- 1594 Kaplan, O.I., Molla-Herman, A., Cevik, S., Ghossoub, R., Kida, K., Kimura, Y., Jenkins, P.,
 1595 Martens, J.R., Setou, M., Benmerah, A., Blacque, O.E., 2010. The AP-1 clathrin
 1596 adaptor facilitates cilium formation and functions with RAB-8 in *C. elegans* ciliary
 1597 membrane transport. *J. Cell Sci.* 123, 3966–3977. doi:10.1242/jcs.073908
- 1598 Kapoor, S., Fansa, E.K., Möbitz, S., Ismail, S.A., Winter, R., Wittinghofer, A., Weise, K.,
 1599 2015. Effect of the N-Terminal Helix and Nucleotide Loading on the Membrane and
 1600 Effector Binding of Arl2/3. *Biophys. J.* 109, 1619–1629. doi:10.1016/j.bpj.2015.08.033
- 1601 Katoh, Y., Terada, M., Nishijima, Y., Takei, R., Nozaki, S., Hamada, H., Nakayama, K., 2016.
 1602 Overall Architecture of the Intraflagellar Transport (IFT)-B Complex Containing
 1603 Cluap1/IFT38 as an Essential Component of the IFT-B Peripheral Subcomplex. *J. Biol.*
 1604 *Chem.* 291, 10962–10975. doi:10.1074/jbc.M116.713883
- 1605 Keady, B.T., Samtani, R., Tobita, K., Tsuchya, M., San Agustin, J.T., Follit, J.A., Jonassen,
 1606 J.A., Subramanian, R., Lo, C.W., Pazour, G.J., 2012. IFT25 links the signal-dependent
 1607 movement of Hedgehog components to intraflagellar transport. *Dev. Cell* 22, 940–951.
 1608 doi:10.1016/j.devcel.2012.04.009
- 1609 Kennedy, M.J., Ehlers, M.D., 2011. Mechanisms and function of dendritic exocytosis. *Neuron*
 1610 69, 856–875. doi:10.1016/j.neuron.2011.02.032
- 1611 Kiesel, P., Alvarez Viar, G., Tsoy, N., Maraspini, R., Gorilak, P., Varga, V., Honigmann, A.,
 1612 Pigino, G., 2020. The molecular structure of mammalian primary cilia revealed by
 1613 cryo-electron tomography. *Nat. Struct. Mol. Biol.* 27, 1115–1124. doi:10.1038/s41594-
 1614 020-0507-4
- 1615 Kim, H., Xu, H., Yao, Q., Li, W., Huang, Q., Outeda, P., Cebotaru, V., Chiaravalli, M.,

- 1616 Boletta, A., Piontek, K., Germino, G.G., Weinman, E.J., Watnick, T., Qian, F., 2014.
 1617 Ciliary membrane proteins traffic through the Golgi via a Rabep1/GGA1/Arl3-
 1618 dependent mechanism. *Nat. Commun.* 5, 5482. doi:10.1038/ncomms6482
- 1619 Klink, B.U., Gatsogiannis, C., Hofnagel, O., Wittinghofer, A., Raunser, S., 2020. Structure of
 1620 the human BBSome core complex. *Elife* 9. doi:10.7554/eLife.53910
- 1621 Kozminski, K.G., Johnson, K.A., Forscher, P., Rosenbaum, J.L., 1993. A motility in the
 1622 eukaryotic flagellum unrelated to flagellar beating. *Proc. Natl. Acad. Sci. USA* 90,
 1623 5519–5523. doi:10.1073/pnas.90.12.5519
- 1624 Kremer, J.R., Mastronarde, D.N., McIntosh, J.R., 1996. Computer visualization of three-
 1625 dimensional image data using IMOD. *J. Struct. Biol.* 116, 71–76.
 1626 doi:10.1006/jsbi.1996.0013
- 1627 Leaf, A., Von Zastrow, M., 2015. Dopamine receptors reveal an essential role of IFT-B,
 1628 KIF17, and Rab23 in delivering specific receptors to primary cilia. *Elife* 4.
 1629 doi:10.7554/eLife.06996
- 1630 Lechtreck, K.F., Brown, J.M., Sampaio, J.L., Craft, J.M., Shevchenko, A., Evans, J.E.,
 1631 Witman, G.B., 2013. Cycling of the signaling protein phospholipase D through cilia
 1632 requires the BBSome only for the export phase. *J. Cell Biol.* 201, 249–261.
 1633 doi:10.1083/jcb.201207139
- 1634 Lechtreck, K.-F., Johnson, E.C., Sakai, T., Cochran, D., Ballif, B.A., Rush, J., Pazour, G.J.,
 1635 Ikebe, M., Witman, G.B., 2009. The *Chlamydomonas reinhardtii* BBSome is an IFT
 1636 cargo required for export of specific signaling proteins from flagella. *J. Cell Biol.* 187,
 1637 1117–1132. doi:10.1083/jcb.200909183
- 1638 Lee, C., Goldberg, J., 2010. Structure of coatamer cage proteins and the relationship among
 1639 COPI, COPII, and clathrin vesicle coats. *Cell* 142, 123–132.
 1640 doi:10.1016/j.cell.2010.05.030
- 1641 Lee, E., Sivan-Loukianova, E., Eberl, D.F., Kernan, M.J., 2008. An IFT-A protein is required
 1642 to delimit functionally distinct zones in mechanosensory cilia. *Curr. Biol.* 18, 1899–
 1643 1906. doi:10.1016/j.cub.2008.11.020
- 1644 Li, Y., Wei, Q., Zhang, Y., Ling, K., Hu, J., 2010. The small GTPases ARL-13 and ARL-3
 1645 coordinate intraflagellar transport and ciliogenesis. *J. Cell Biol.* 189, 1039–1051.
 1646 doi:10.1083/jcb.200912001
- 1647 Liem, K.F., Ashe, A., He, M., Satir, P., Moran, J., Beier, D., Wicking, C., Anderson, K.V.,
 1648 2012. The IFT-A complex regulates Shh signaling through cilia structure and
 1649 membrane protein trafficking. *J. Cell Biol.* 197, 789–800. doi:10.1083/jcb.201110049
- 1650 Liew, G.M., Ye, F., Nager, A.R., Murphy, J.P., Lee, J.S., Aguiar, M., Breslow, D.K., Gygi,
 1651 S.P., Nachury, M.V., 2014. The intraflagellar transport protein IFT27 promotes
 1652 BBSome exit from cilia through the GTPase ARL6/BBS3. *Dev. Cell* 31, 265–278.
 1653 doi:10.1016/j.devcel.2014.09.004
- 1654 Mastronarde, D.N., 2005. Automated electron microscope tomography using robust prediction
 1655 of specimen movements. *J. Struct. Biol.* 152, 36–51. doi:10.1016/j.jsb.2005.07.007
- 1656 Mazelova, J., Astuto-Gribble, L., Inoue, H., Tam, B.M., Schonteich, E., Prekeris, R., Moritz,
 1657 O.L., Randazzo, P.A., Deretic, D., 2009. Ciliary targeting motif VxPx directs assembly
 1658 of a trafficking module through Arf4. *EMBO J.* 28, 183–192.
 1659 doi:10.1038/emboj.2008.267
- 1660 McMahan, H.T., Boucrot, E., 2015. Membrane curvature at a glance. *J. Cell Sci.* 128, 1065–
 1661 1070. doi:10.1242/jcs.114454
- 1662 Milenkovic, L., Scott, M.P., Rohatgi, R., 2009. Lateral transport of Smoothed from the
 1663 plasma membrane to the membrane of the cilium. *J. Cell Biol.* 187, 365–374.
 1664 doi:10.1083/jcb.200907126
- 1665 Mill, P., Lockhart, P.J., Fitzpatrick, E., Mountford, H.S., Hall, E.A., Reijns, M.A.M.,
 1666 Keighren, M., Bahlo, M., Bromhead, C.J., Budd, P., Aftimos, S., Delatycki, M.B.,
 1667 Savarirayan, R., Jackson, I.J., Amor, D.J., 2011. Human and mouse mutations in
 1668 WDR35 cause short-rib polydactyly syndromes due to abnormal ciliogenesis. *Am. J.*

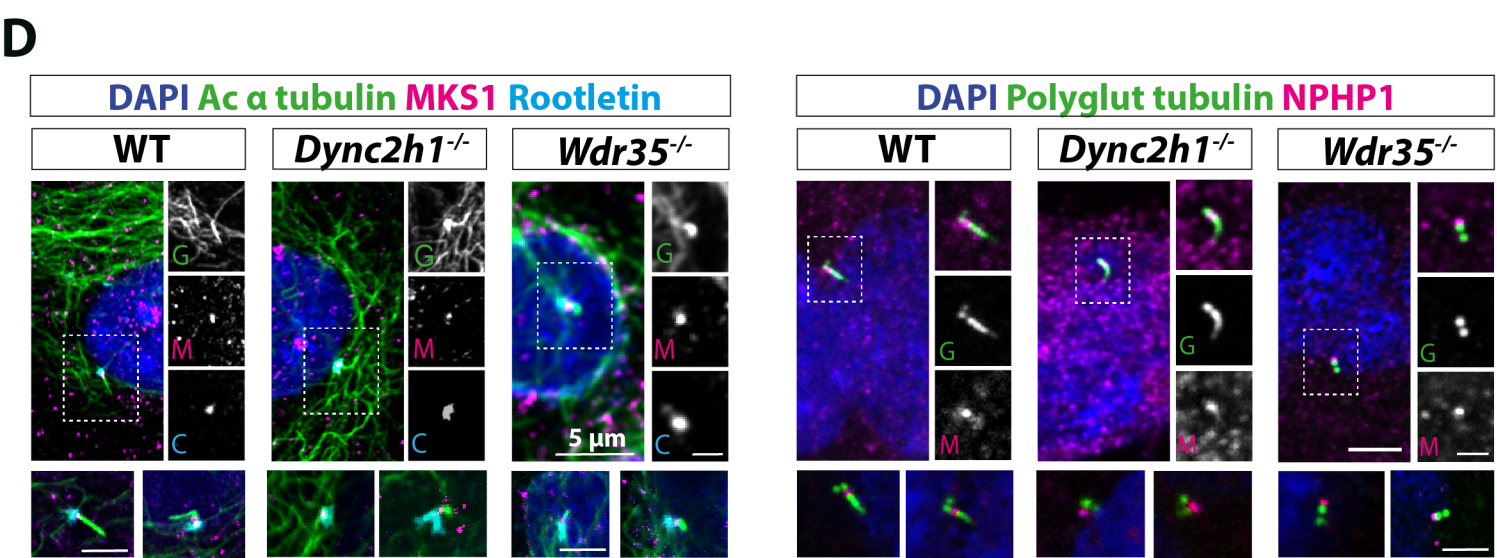
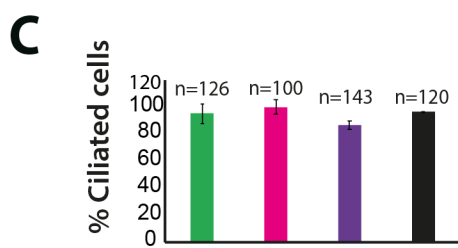
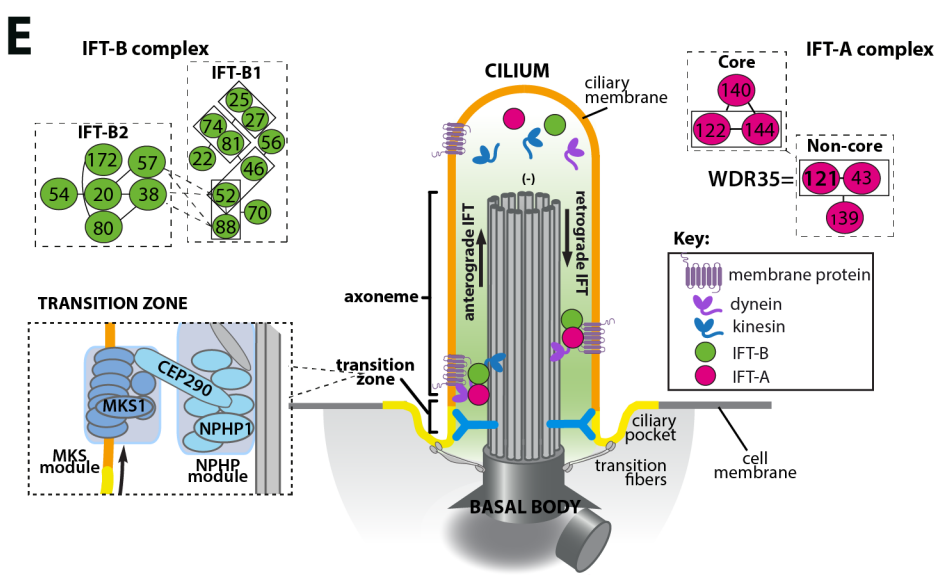
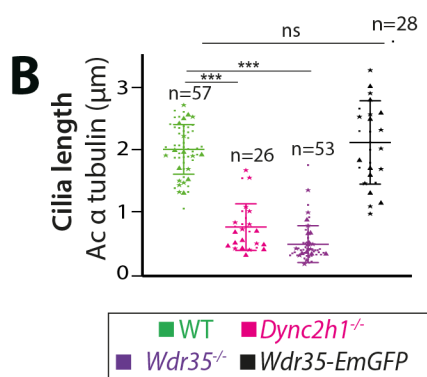
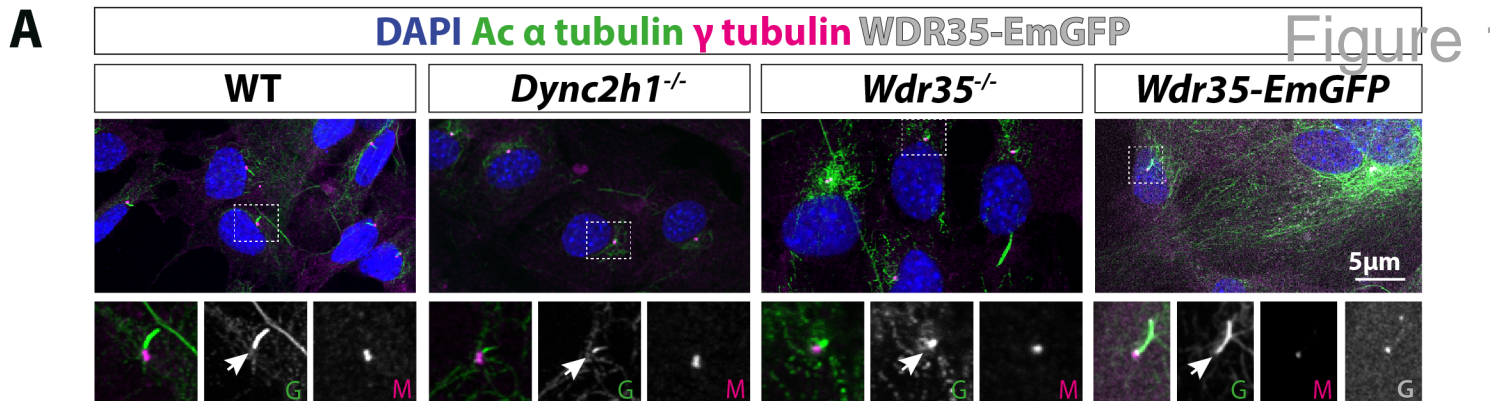
- 1669 Hum. Genet. 88, 508–515. doi:10.1016/j.ajhg.2011.03.015
- 1670 Molla-Herman, A., Ghossoub, R., Blisnick, T., Meunier, A., Serres, C., Silbermann, F.,
1671 Emmerson, C., Romeo, K., Bourdoncle, P., Schmitt, A., Saunier, S., Spassky, N.,
1672 Bastin, P., Benmerah, A., 2010. The ciliary pocket: an endocytic membrane domain at
1673 the base of primary and motile cilia. *J. Cell Sci.* 123, 1785–1795.
1674 doi:10.1242/jcs.059519
- 1675 Moritz, O.L., Tam, B.M., Hurd, L.L., Peränen, J., Deretic, D., Papermaster, D.S., 2001.
1676 Mutant rab8 Impairs docking and fusion of rhodopsin-bearing post-Golgi membranes
1677 and causes cell death of transgenic *Xenopus* rods. *Mol. Biol. Cell* 12, 2341–2351.
1678 doi:10.1091/mbc.12.8.2341
- 1679 Mourão, A., Christensen, S.T., Lorentzen, E., 2016. The intraflagellar transport machinery in
1680 ciliary signaling. *Curr. Opin. Struct. Biol.* 41, 98–108. doi:10.1016/j.sbi.2016.06.009
- 1681 Mukhopadhyay, S., Wen, X., Chih, B., Nelson, C.D., Lane, W.S., Scales, S.J., Jackson, P.K.,
1682 2010. TULP3 bridges the IFT-A complex and membrane phosphoinositides to promote
1683 trafficking of G protein-coupled receptors into primary cilia. *Genes Dev.* 24, 2180–
1684 2193. doi:10.1101/gad.1966210
- 1685 Nachury, M.V., 2018. The molecular machines that traffic signaling receptors into and out of
1686 cilia. *Curr. Opin. Cell Biol.* 51, 124–131. doi:10.1016/j.ceb.2018.03.004
- 1687 Nachury, M.V., Loktev, A.V., Zhang, Q., Westlake, C.J., Peränen, J., Merdes, A., Slusarski,
1688 D.C., Scheller, R.H., Bazan, J.F., Sheffield, V.C., Jackson, P.K., 2007. A core complex
1689 of BBS proteins cooperates with the GTPase Rab8 to promote ciliary membrane
1690 biogenesis. *Cell* 129, 1201–1213. doi:10.1016/j.cell.2007.03.053
- 1691 Nager, A.R., Goldstein, J.S., Herranz-Pérez, V., Portran, D., Ye, F., Garcia-Verdugo, J.M.,
1692 Nachury, M.V., 2017. An Actin Network Dispatches Ciliary GPCRs into Extracellular
1693 Vesicles to Modulate Signaling. *Cell* 168, 252–263.e14. doi:10.1016/j.cell.2016.11.036
- 1694 Noda, K., Kitami, M., Kitami, K., Kaku, M., Komatsu, Y., 2016. Canonical and noncanonical
1695 intraflagellar transport regulates craniofacial skeletal development. *Proc. Natl. Acad.*
1696 *Sci. USA* 113, E2589–97. doi:10.1073/pnas.1519458113
- 1697 Ollion, J., Cochenec, J., Loll, F., Escudé, C., Boudier, T., 2013. TANGO: a generic tool for
1698 high-throughput 3D image analysis for studying nuclear organization. *Bioinformatics*
1699 29, 1840–1841. doi:10.1093/bioinformatics/btt276
- 1700 Orci, L., Perrelet, A., Rothman, J.E., 1998. Vesicles on strings: morphological evidence for
1701 processive transport within the Golgi stack. *Proc. Natl. Acad. Sci. USA* 95, 2279–
1702 2283. doi:10.1073/pnas.95.5.2279
- 1703 Ou, G., Koga, M., Blacque, O.E., Murayama, T., Ohshima, Y., Schafer, J.C., Li, C., Yoder,
1704 B.K., Leroux, M.R., Scholey, J.M., 2007. Sensory ciliogenesis in *Caenorhabditis*
1705 *elegans*: assignment of IFT components into distinct modules based on transport and
1706 phenotypic profiles. *Mol. Biol. Cell* 18, 1554–1569. doi:10.1091/mbc.e06-09-0805
- 1707 Pazour, G.J., Wilkerson, C.G., Witman, G.B., 1998. A dynein light chain is essential for the
1708 retrograde particle movement of intraflagellar transport (IFT). *J. Cell Biol.* 141, 979–
1709 992. doi:10.1083/jcb.141.4.979
- 1710 Pedersen, L.B., Mogensen, J.B., Christensen, S.T., 2016. Endocytic control of cellular
1711 signaling at the primary cilium. *Trends Biochem. Sci.* 41, 784–797.
1712 doi:10.1016/j.tibs.2016.06.002
- 1713 Picariello, T., Brown, J.M., Hou, Y., Swank, G., Cochran, D.A., King, O.D., Lechtreck, K.,
1714 Pazour, G.J., Witman, G.B., 2019. A global analysis of IFT-A function reveals
1715 specialization for transport of membrane-associated proteins into cilia. *J. Cell Sci.* 132.
1716 doi:10.1242/jcs.220749
- 1717 Pigino, G., Geimer, S., Lanzavecchia, S., Paccagnini, E., Cantele, F., Diener, D.R.,
1718 Rosenbaum, J.L., Lupetti, P., 2009. Electron-tomographic analysis of intraflagellar
1719 transport particle trains in situ. *J. Cell Biol.* 187, 135–148. doi:10.1083/jcb.200905103
- 1720 Piperno, G., Siuda, E., Henderson, S., Segil, M., Vaananen, H., Sassaroli, M., 1998. Distinct
1721 mutants of retrograde intraflagellar transport (IFT) share similar morphological and

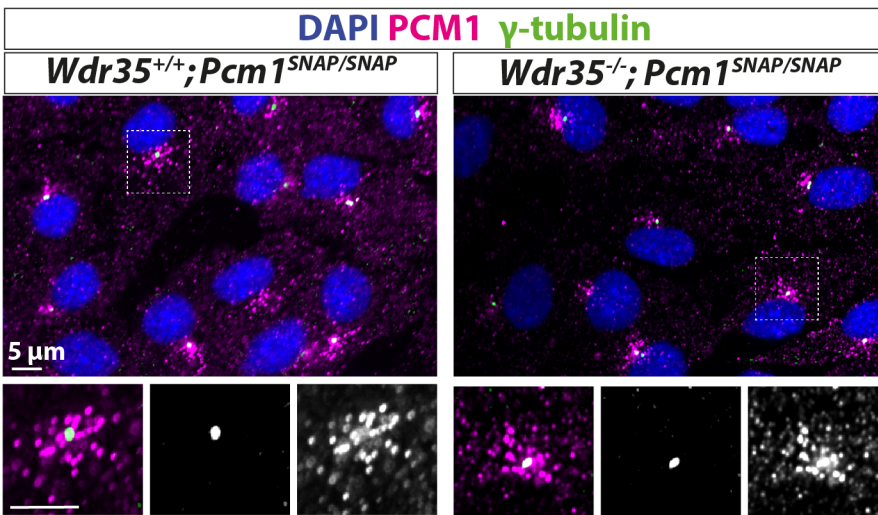
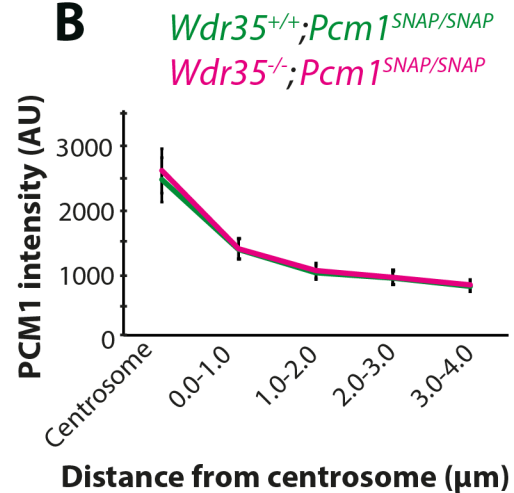
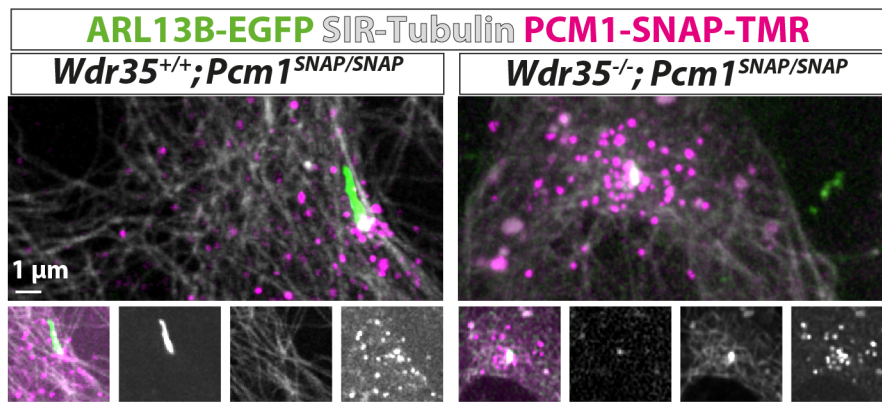
- 1722 molecular defects. *J. Cell Biol.* 143, 1591–1601. doi:10.1083/jcb.143.6.1591
- 1723 Porter, M.E., Bower, R., Knott, J.A., Byrd, P., Dentler, W., 1999. Cytoplasmic dynein heavy
1724 chain 1b is required for flagellar assembly in *Chlamydomonas*. *Mol. Biol. Cell* 10,
1725 693–712. doi:10.1091/mbc.10.3.693
- 1726 Qin, J., Lin, Y., Norman, R.X., Ko, H.W., Eggenschwiler, J.T., 2011. Intraflagellar transport
1727 protein 122 antagonizes Sonic Hedgehog signaling and controls ciliary localization of
1728 pathway components. *Proc. Natl. Acad. Sci. USA* 108, 1456–1461.
1729 doi:10.1073/pnas.1011410108
- 1730 Quarmby, L.M., Yueh, Y.G., Cheshire, J.L., Keller, L.R., Snell, W.J., Crain, R.C., 1992.
1731 Inositol phospholipid metabolism may trigger flagellar excision in *Chlamydomonas*
1732 *reinhardtii*. *J. Cell Biol.* 116, 737–744.
- 1733 Reiter, J.F., Leroux, M.R., 2017. Genes and molecular pathways underpinning ciliopathies.
1734 *Nat. Rev. Mol. Cell Biol.* 18, 533–547. doi:10.1038/nrm.2017.60
- 1735 Remmert, M., Biegert, A., Hauser, A., Söding, J., 2011. HHblits: lightning-fast iterative
1736 protein sequence searching by HMM-HMM alignment. *Nat. Methods* 9, 173–175.
1737 doi:10.1038/nmeth.1818
- 1738 Rogowski, M., Scholz, D., Geimer, S., 2013. Electron microscopy of flagella, primary cilia,
1739 and intraflagellar transport in flat-embedded cells. *Meth. Enzymol.* 524, 243–263.
1740 doi:10.1016/B978-0-12-397945-2.00014-7
- 1741 Rosenbaum, J.L., Witman, G.B., 2002. Intraflagellar transport. *Nat. Rev. Mol. Cell Biol.* 3,
1742 813–825. doi:10.1038/nrm952
- 1743 Roy, K., Jerman, S., Jozsef, L., McNamara, T., Onyekaba, G., Sun, Z., Marin, E.P., 2017.
1744 Palmitoylation of the ciliary GTPase ARL13b is necessary for its stability and its role
1745 in cilia formation. *J. Biol. Chem.* 292, 17703–17717. doi:10.1074/jbc.M117.792937
- 1746 Sato, T., Iwano, T., Kunii, M., Matsuda, S., Mizuguchi, R., Jung, Y., Hagiwara, H., Yoshihara,
1747 Y., Yuzaki, M., Harada, R., Harada, A., 2014. Rab8a and Rab8b are essential for
1748 several apical transport pathways but insufficient for ciliogenesis. *J. Cell Sci.* 127,
1749 422–431. doi:10.1242/jcs.136903
- 1750 Scheidel, N., Blacque, O.E., 2018. Intraflagellar transport complex A genes differentially
1751 regulate cilium formation and transition zone gating. *Curr. Biol.* 28, 3279–3287.e2.
1752 doi:10.1016/j.cub.2018.08.017
- 1753 Schindelin, J., Arganda-Carreras, I., Frise, E., Kaynig, V., Longair, M., Pietzsch, T., Preibisch,
1754 S., Rueden, C., Saalfeld, S., Schmid, B., Tinevez, J.-Y., White, D.J., Hartenstein, V.,
1755 Eliceiri, K., Tomancak, P., Cardona, A., 2012. Fiji: an open-source platform for
1756 biological-image analysis. *Nat. Methods* 9, 676–682. doi:10.1038/nmeth.2019
- 1757 Schmidt, K.N., Kuhns, S., Neuner, A., Hub, B., Zentgraf, H., Pereira, G., 2012. Cep164
1758 mediates vesicular docking to the mother centriole during early steps of ciliogenesis. *J.*
1759 *Cell Biol.* 199, 1083–1101. doi:10.1083/jcb.201202126
- 1760 Sedmak, T., Wolfrum, U., 2010. Intraflagellar transport molecules in ciliary and nonciliary
1761 cells of the retina. *J. Cell Biol.* 189, 171–186. doi:10.1083/jcb.200911095
- 1762 Shinde, S.R., Nager, A.R., Nachury, M.V., 2020. Ubiquitin chains earmark GPCRs for
1763 BBSome-mediated removal from cilia. *J. Cell Biol.* 219. doi:10.1083/jcb.202003020
- 1764 Signor, D., Wedaman, K.P., Orozco, J.T., Dwyer, N.D., Bargmann, C.I., Rose, L.S., Scholey,
1765 J.M., 1999. Role of a class DHC1b dynein in retrograde transport of IFT motors and
1766 IFT raft particles along cilia, but not dendrites, in chemosensory neurons of living
1767 *Caenorhabditis elegans*. *J. Cell Biol.* 147, 519–530. doi:10.1083/jcb.147.3.519
- 1768 Singh, S.K., Gui, M., Koh, F., Yip, M.C., Brown, A., 2020. Structure and activation
1769 mechanism of the BBSome membrane protein trafficking complex. *Elife* 9.
1770 doi:10.7554/eLife.53322
- 1771 Sorokin, S., 1962. Centrioles and the formation of rudimentary cilia by fibroblasts and smooth
1772 muscle cells. *J. Cell Biol.* 15, 363–377. doi:10.1083/jcb.15.2.363
- 1773 Stepanek, L., Pigino, G., 2016. Microtubule doublets are double-track railways for
1774 intraflagellar transport trains. *Science* 352, 721–724. doi:10.1126/science.aaf4594

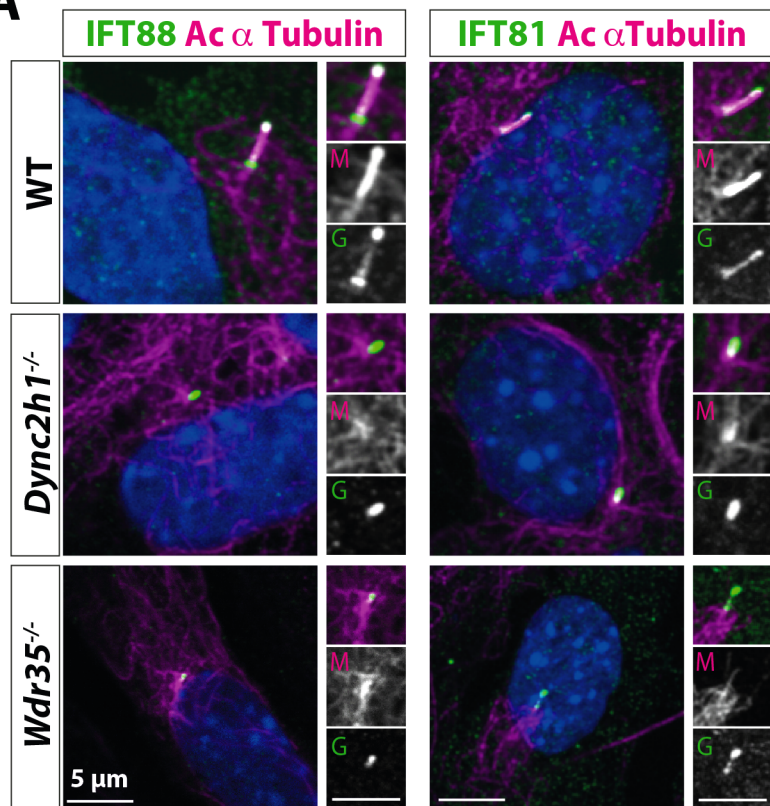
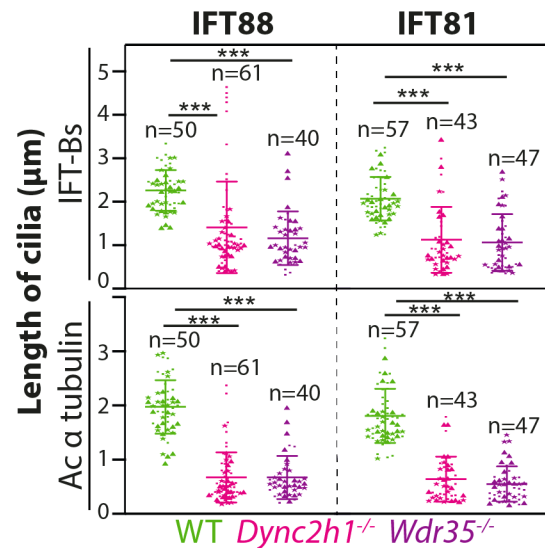
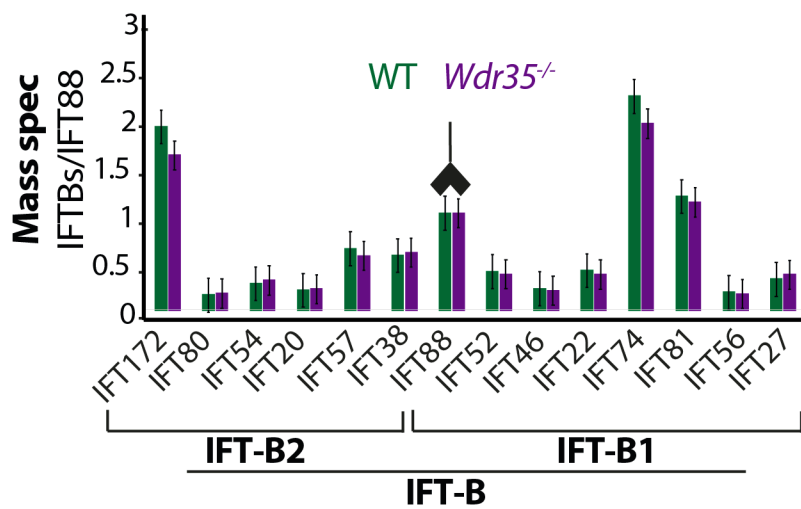
- 1775 Takahara, M., Katoh, Y., Nakamura, K., Hirano, T., Sugawa, M., Tsurumi, Y., Nakayama, K.,
1776 2018. Ciliopathy-associated mutations of IFT122 impair ciliary protein trafficking but
1777 not ciliogenesis. *Hum. Mol. Genet.* 27, 516–528. doi:10.1093/hmg/ddx421
- 1778 Tanos, B.E., Yang, H.-J., Soni, R., Wang, W.-J., Macaluso, F.P., Asara, J.M., Tsou, M.-F.B.,
1779 2013. Centriole distal appendages promote membrane docking, leading to cilia
1780 initiation. *Genes Dev.* 27, 163–168. doi:10.1101/gad.207043.112
- 1781 Taschner, M., Bhogaraju, S., Lorentzen, E., 2012. Architecture and function of IFT complex
1782 proteins in ciliogenesis. *Differentiation.* 83, S12–22. doi:10.1016/j.diff.2011.11.001
- 1783 Taschner, M., Lorentzen, A., Mourão, A., Collins, T., Freke, G.M., Moulding, D., Basquin, J.,
1784 Jenkins, D., Lorentzen, E., 2018. Crystal structure of intraflagellar transport protein 80
1785 reveals a homo-dimer required for ciliogenesis. *Elife* 7. doi:10.7554/eLife.33067
- 1786 Taschner, M., Mourão, A., Awasthi, M., Basquin, J., Lorentzen, E., 2017. Structural basis of
1787 outer dynein arm intraflagellar transport by the transport adaptor protein ODA16 and
1788 the intraflagellar transport protein IFT46. *J. Biol. Chem.* 292, 7462–7473.
1789 doi:10.1074/jbc.M117.780155
- 1790 Taschner, M., Weber, K., Mourão, A., Vetter, M., Awasthi, M., Stiegler, M., Bhogaraju, S.,
1791 Lorentzen, E., 2016. Intraflagellar transport proteins 172, 80, 57, 54, 38, and 20 form a
1792 stable tubulin-binding IFT-B2 complex. *EMBO J.* 35, 773–790.
1793 doi:10.15252/embj.201593164
- 1794 Toriyama, M., Lee, C., Taylor, S.P., Duran, I., Cohn, D.H., Bruel, A.-L., Tabler, J.M., Drew,
1795 K., Kelly, M.R., Kim, S., Park, T.J., Braun, D.A., Pierquin, G., Biver, A., Wagner, K.,
1796 Malfroot, A., Panigrahi, I., Franco, B., Al-Lami, H.A., Yeung, Y., Choi, Y.J.,
1797 University of Washington Center for Mendelian Genomics, Duffourd, Y., Faivre, L.,
1798 Rivière, J.-B., Chen, J., Liu, K.J., Marcotte, E.M., Hildebrandt, F., Thauvin-Robinet,
1799 C., Krakow, D., Jackson, P.K., Wallingford, J.B., 2016. The ciliopathy-associated
1800 CPLANE proteins direct basal body recruitment of intraflagellar transport machinery.
1801 *Nat. Genet.* 48, 648–656. doi:10.1038/ng.3558
- 1802 Tran, P.V., Haycraft, C.J., Besschetnova, T.Y., Turbe-Doan, A., Stottmann, R.W., Herron,
1803 B.J., Chesebro, A.L., Qiu, H., Scherz, P.J., Shah, J.V., Yoder, B.K., Beier, D.R., 2008.
1804 THM1 negatively modulates mouse sonic hedgehog signal transduction and affects
1805 retrograde intraflagellar transport in cilia. *Nat. Genet.* 40, 403–410. doi:10.1038/ng.105
- 1806 Tsao, C.-C., Gorovsky, M.A., 2008. Tetrahymena IFT122A is not essential for cilia assembly
1807 but plays a role in returning IFT proteins from the ciliary tip to the cell body. *J. Cell*
1808 *Sci.* 121, 428–436. doi:10.1242/jcs.015826
- 1809 Turriziani, B., Garcia-Munoz, A., Pilkington, R., Raso, C., Kolch, W., von Kriegsheim, A.,
1810 2014. On-beads digestion in conjunction with data-dependent mass spectrometry: a
1811 shortcut to quantitative and dynamic interaction proteomics. *Biology (Basel)* 3, 320–
1812 332. doi:10.3390/biology3020320
- 1813 Tyler, K.M., Fridberg, A., Toriello, K.M., Olson, C.L., Cieslak, J.A., Hazlett, T.L., Engman,
1814 D.M., 2009. Flagellar membrane localization via association with lipid rafts. *J. Cell*
1815 *Sci.* 122, 859–866. doi:10.1242/jcs.037721
- 1816 van Dam, T.J.P., Townsend, M.J., Turk, M., Schlessinger, A., Sali, A., Field, M.C., Huynen,
1817 M.A., 2013. Evolution of modular intraflagellar transport from a coatomer-like
1818 progenitor. *Proc. Natl. Acad. Sci. USA* 110, 6943–6948. doi:10.1073/pnas.1221011110
- 1819 Vince, J.E., Tull, D.L., Spurck, T., Derby, M.C., McFadden, G.I., Gleeson, P.A., Gokool, S.,
1820 McConville, M.J., 2008. Leishmania adaptor protein-1 subunits are required for normal
1821 lysosome traffic, flagellum biogenesis, lipid homeostasis, and adaptation to
1822 temperatures encountered in the mammalian host. *Eukaryotic Cell* 7, 1256–1267.
1823 doi:10.1128/EC.00090-08
- 1824 Wang, J., Deretic, D., 2014. Molecular complexes that direct rhodopsin transport to primary
1825 cilia. *Prog Retin Eye Res* 38, 1–19. doi:10.1016/j.preteyeres.2013.08.004
- 1826 Wang, J., Fresquez, T., Kandachar, V., Deretic, D., 2017. The Arf GEF GBF1 and Arf4
1827 synergize with the sensory receptor cargo, rhodopsin, to regulate ciliary membrane

- 1828 trafficking. *J. Cell Sci.* 130, 3975–3987. doi:10.1242/jcs.205492
- 1829 Wang, Q., Taschner, M., Ganzinger, K.A., Kelley, C., Villasenor, A., Heymann, M., Schwille,
1830 P., Lorentzen, E., Mizuno, N., 2018. Membrane association and remodeling by
1831 intraflagellar transport protein IFT172. *Nat. Commun.* 9, 4684. doi:10.1038/s41467-
1832 018-07037-9
- 1833 Wang, Z., Fan, Z.-C., Williamson, S.M., Qin, H., 2009. Intraflagellar transport (IFT) protein
1834 IFT25 is a phosphoprotein component of IFT complex B and physically interacts with
1835 IFT27 in *Chlamydomonas*. *PLoS One* 4, e5384. doi:10.1371/journal.pone.0005384
- 1836 Waterhouse, A., Bertoni, M., Bienert, S., Studer, G., Tauriello, G., Gumienny, R., Heer, F.T.,
1837 de Beer, T.A.P., Rempfer, C., Bordoli, L., Lepore, R., Schwede, T., 2018. SWISS-
1838 MODEL: homology modelling of protein structures and complexes. *Nucleic Acids*
1839 *Res.* 46, W296–W303. doi:10.1093/nar/gky427
- 1840 Wells, J.N., Gligoris, T.G., Nasmyth, K.A., Marsh, J.A., 2017. Evolution of condensin and
1841 cohesin complexes driven by replacement of Kite by Hawk proteins. *Curr. Biol.* 27,
1842 R17–R18. doi:10.1016/j.cub.2016.11.050
- 1843 Wells, J.N., Marsh, J.A., 2019. A Graph-Based Approach for Detecting Sequence Homology
1844 in Highly Diverged Repeat Protein Families. *Methods Mol. Biol.* 1851, 251–261.
1845 doi:10.1007/978-1-4939-8736-8_13
- 1846 Wheatley, D.N., 1969. Cilia in cell-cultured fibroblasts. I. On their occurrence and relative
1847 frequencies in primary cultures and established cell lines. *J. Anat.* 105, 351–362.
- 1848 Williams, C.L., McIntyre, J.C., Norris, S.R., Jenkins, P.M., Zhang, L., Pei, Q., Verhey, K.,
1849 Martens, J.R., 2014. Direct evidence for BBSome-associated intraflagellar transport
1850 reveals distinct properties of native mammalian cilia. *Nat. Commun.* 5, 5813.
1851 doi:10.1038/ncomms6813
- 1852 Witzgall, R., 2018. Golgi bypass of ciliary proteins. *Semin. Cell Dev. Biol.* 83, 51–58.
1853 doi:10.1016/j.semcdb.2018.03.010
- 1854 Wood, C.R., Rosenbaum, J.L., 2014. Proteins of the ciliary axoneme are found on cytoplasmic
1855 membrane vesicles during growth of cilia. *Curr. Biol.* 24, 1114–1120.
1856 doi:10.1016/j.cub.2014.03.047
- 1857 Wood, C.R., Wang, Z., Diener, D., Zones, J.M., Rosenbaum, J., Umen, J.G., 2012. IFT
1858 proteins accumulate during cell division and localize to the cleavage furrow in
1859 *Chlamydomonas*. *PLoS One* 7, e30729. doi:10.1371/journal.pone.0030729
- 1860 Xu, Q., Zhang, Y., Wei, Q., Huang, Y., Li, Y., Ling, K., Hu, J., 2015. BBS4 and BBS5 show
1861 functional redundancy in the BBSome to regulate the degradative sorting of ciliary
1862 sensory receptors. *Sci. Rep.* 5, 11855. doi:10.1038/srep11855
- 1863 Yang, J.-S., Gad, H., Lee, S.Y., Mironov, A., Zhang, L., Beznoussenko, G.V., Valente, C.,
1864 Turacchio, G., Bonsra, A.N., Du, G., Baldanzi, G., Graziani, A., Bourgoin, S.,
1865 Frohman, M.A., Luini, A., Hsu, V.W., 2008. A role for phosphatidic acid in COPI
1866 vesicle fission yields insights into Golgi maintenance. *Nat. Cell Biol.* 10, 1146–1153.
1867 doi:10.1038/ncb1774
- 1868 Yang, S., Bahl, K., Chou, H.-T., Woodsmith, J., Stelzl, U., Walz, T., Nachury, M.V., 2020.
1869 Near-atomic structures of the BBSome reveal the basis for BBSome activation and
1870 binding to GPCR cargoes. *Elife* 9. doi:10.7554/eLife.55954
- 1871 Ye, F., Nager, A.R., Nachury, M.V., 2018. BBSome trains remove activated GPCRs from cilia
1872 by enabling passage through the transition zone. *J. Cell Biol.* 217, 1847–1868.
1873 doi:10.1083/jcb.201709041
- 1874 Yee, L.E., Reiter, J.F., 2015. Ciliary vesicle formation: a prelude to ciliogenesis. *Dev. Cell* 32,
1875 665–666. doi:10.1016/j.devcel.2015.03.012
- 1876 Zeniou-Meyer, M., Zabari, N., Ashery, U., Chasserot-Golaz, S., Haeblerlé, A.-M., Demais, V.,
1877 Bailly, Y., Gottfried, I., Nakanishi, H., Neiman, A.M., Du, G., Frohman, M.A., Bader,
1878 M.-F., Vitale, N., 2007. Phospholipase D1 production of phosphatidic acid at the
1879 plasma membrane promotes exocytosis of large dense-core granules at a late stage. *J.*
1880 *Biol. Chem.* 282, 21746–21757. doi:10.1074/jbc.M702968200

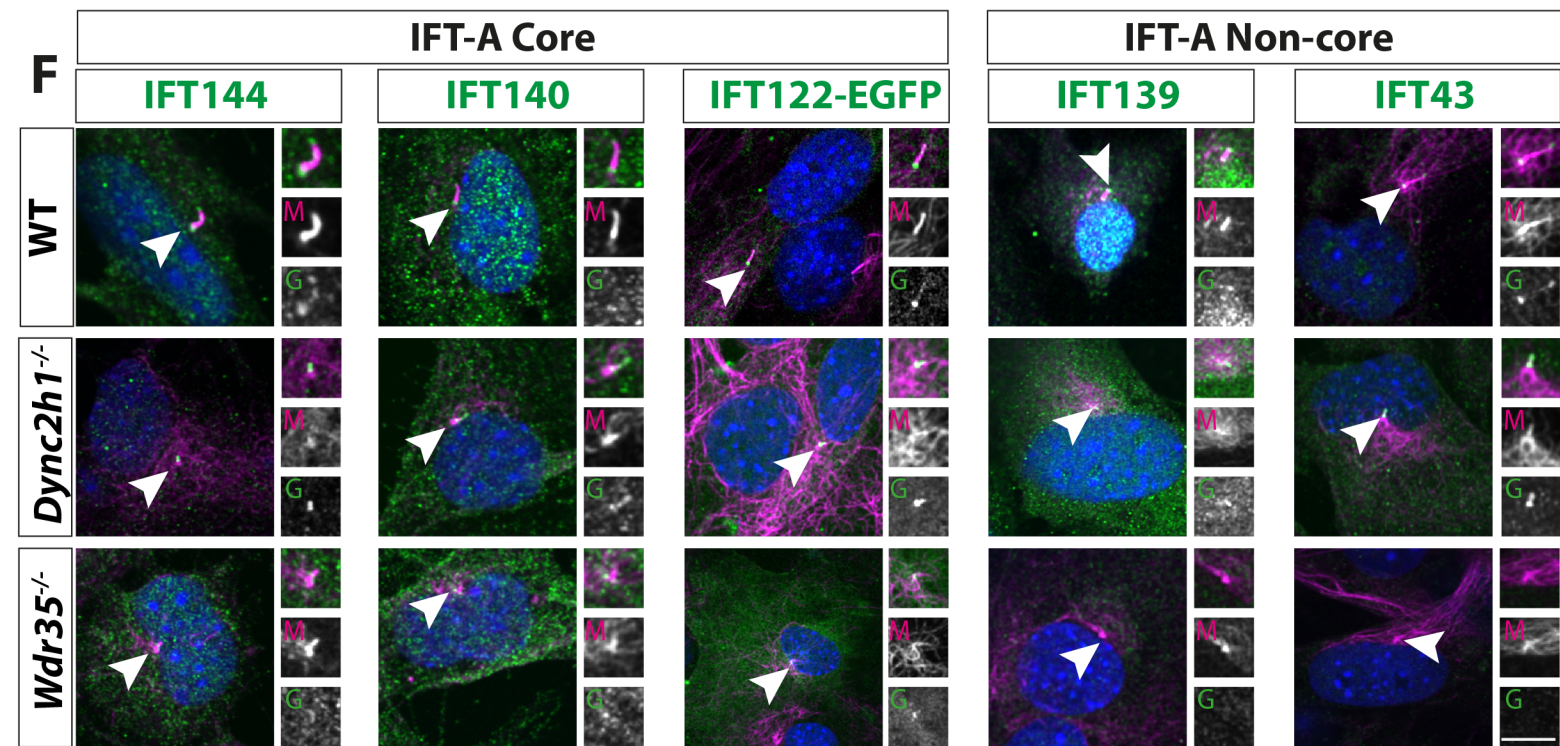
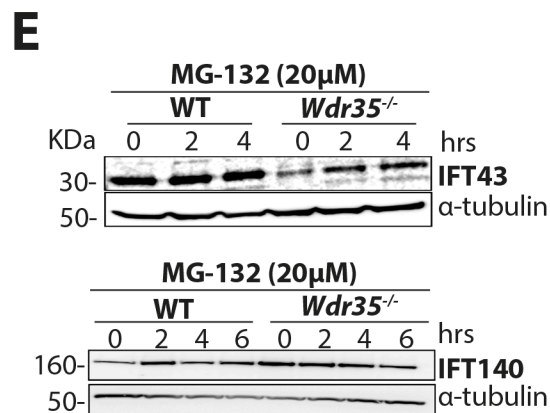
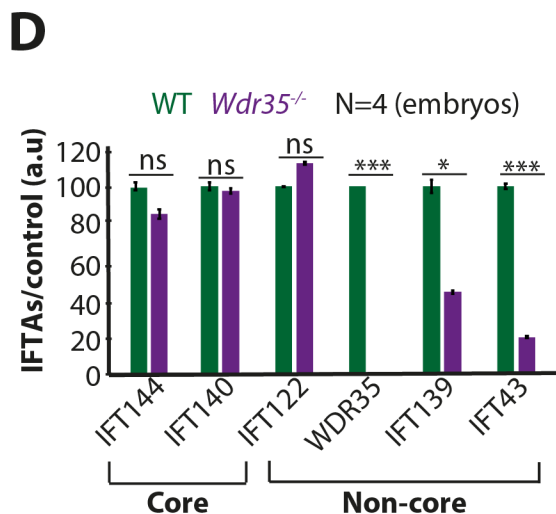
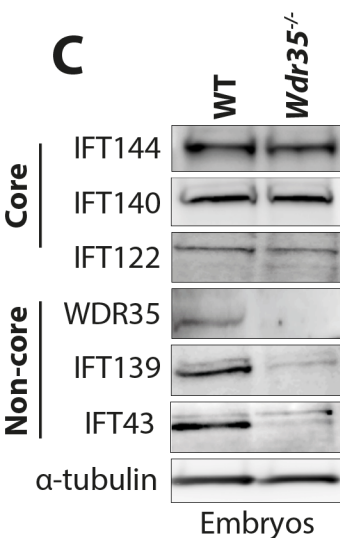
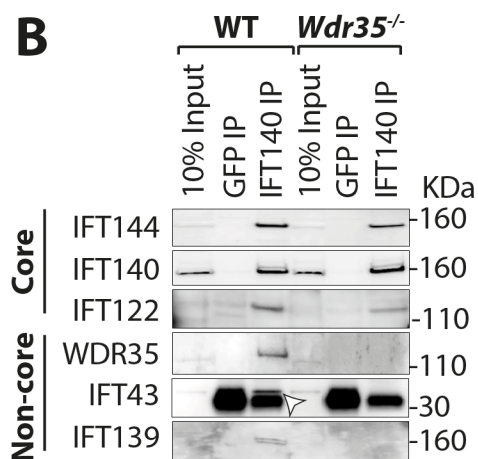
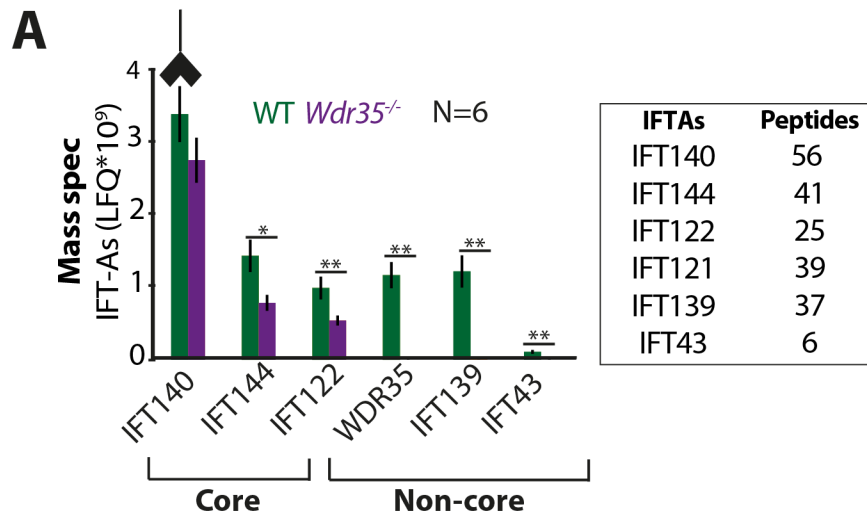
- 1881 Zhu, B., Zhu, X., Wang, L., Liang, Y., Feng, Q., Pan, J., 2017. Functional exploration of the
1882 IFT-A complex in intraflagellar transport and ciliogenesis. *PLoS Genet.* 13, e1006627.
1883 doi:10.1371/journal.pgen.1006627
- 1884 Zhukovsky, M.A., Filograna, A., Luini, A., Corda, D., Valente, C., 2019. Protein amphipathic
1885 helix insertion: A mechanism to induce membrane fission. *Front. Cell Dev. Biol.* 7,
1886 291. doi:10.3389/fcell.2019.00291
- 1887

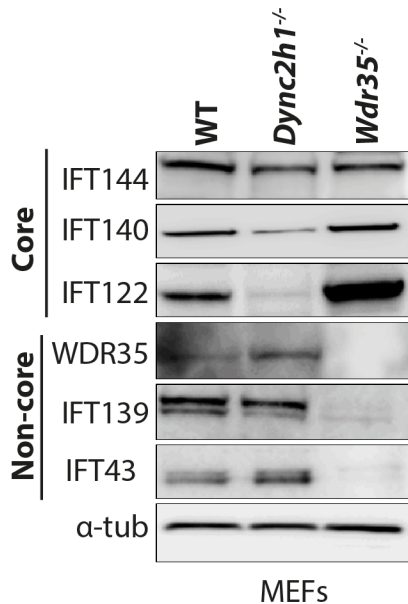
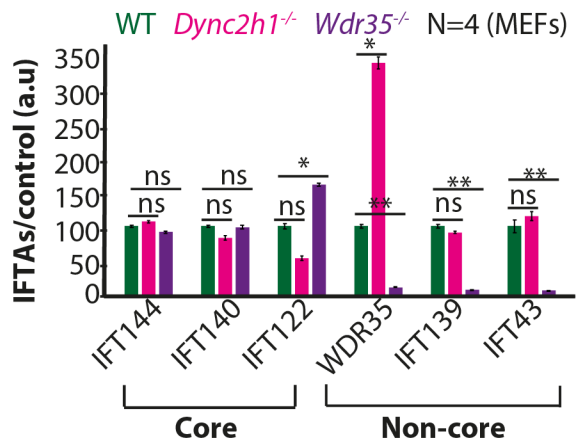
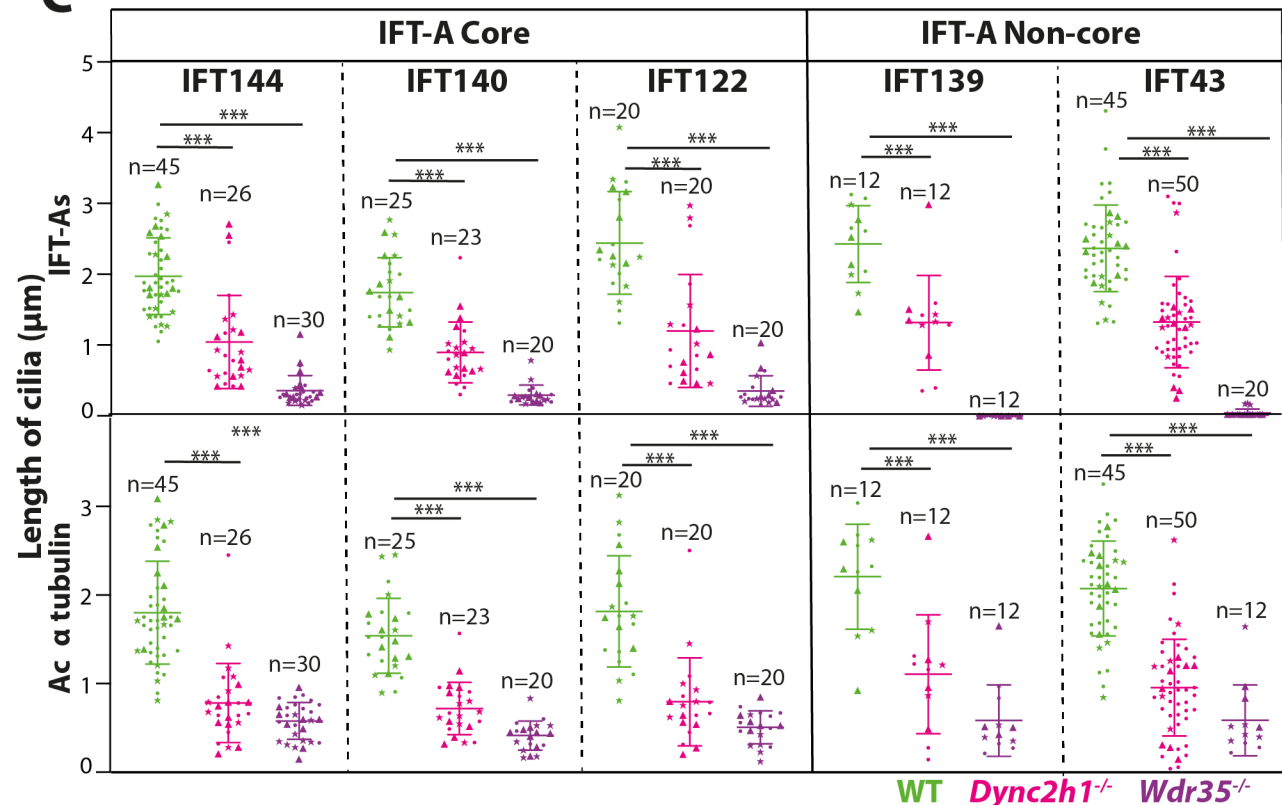


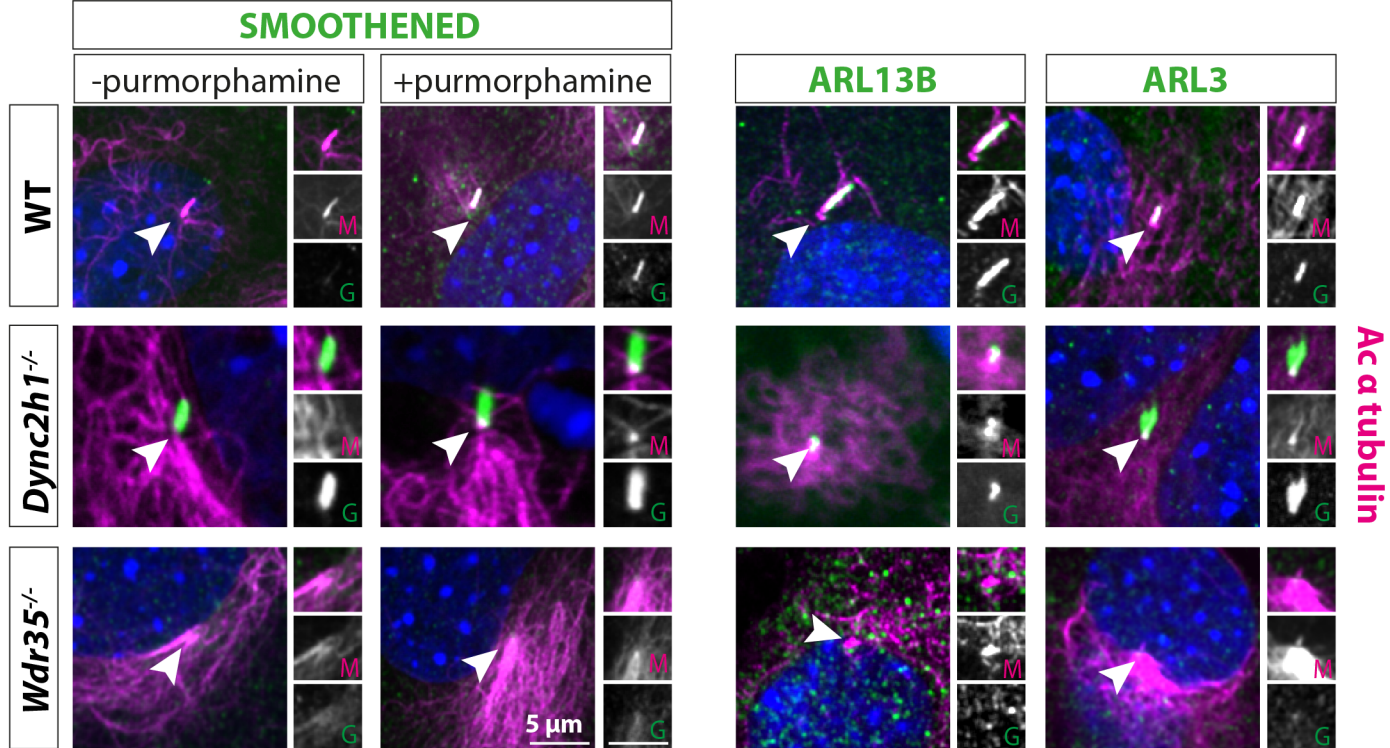
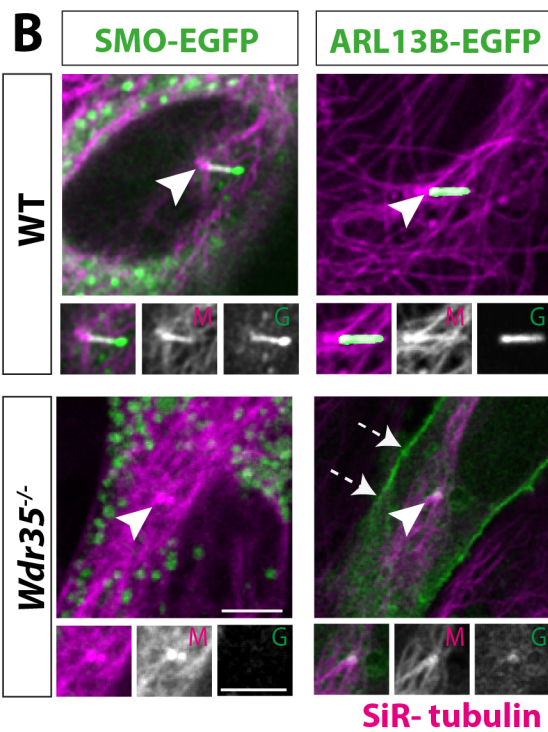
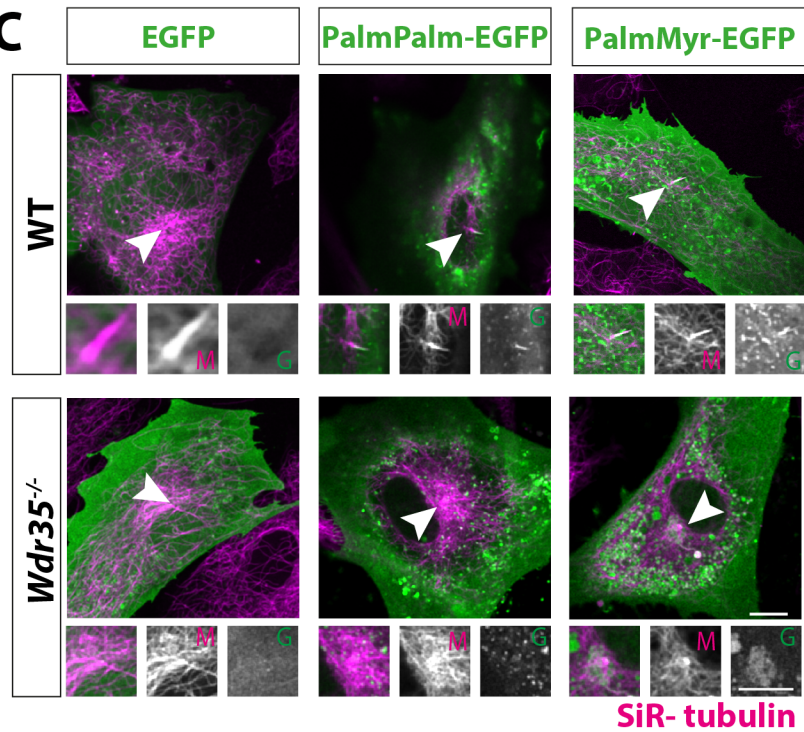
A**B****C**

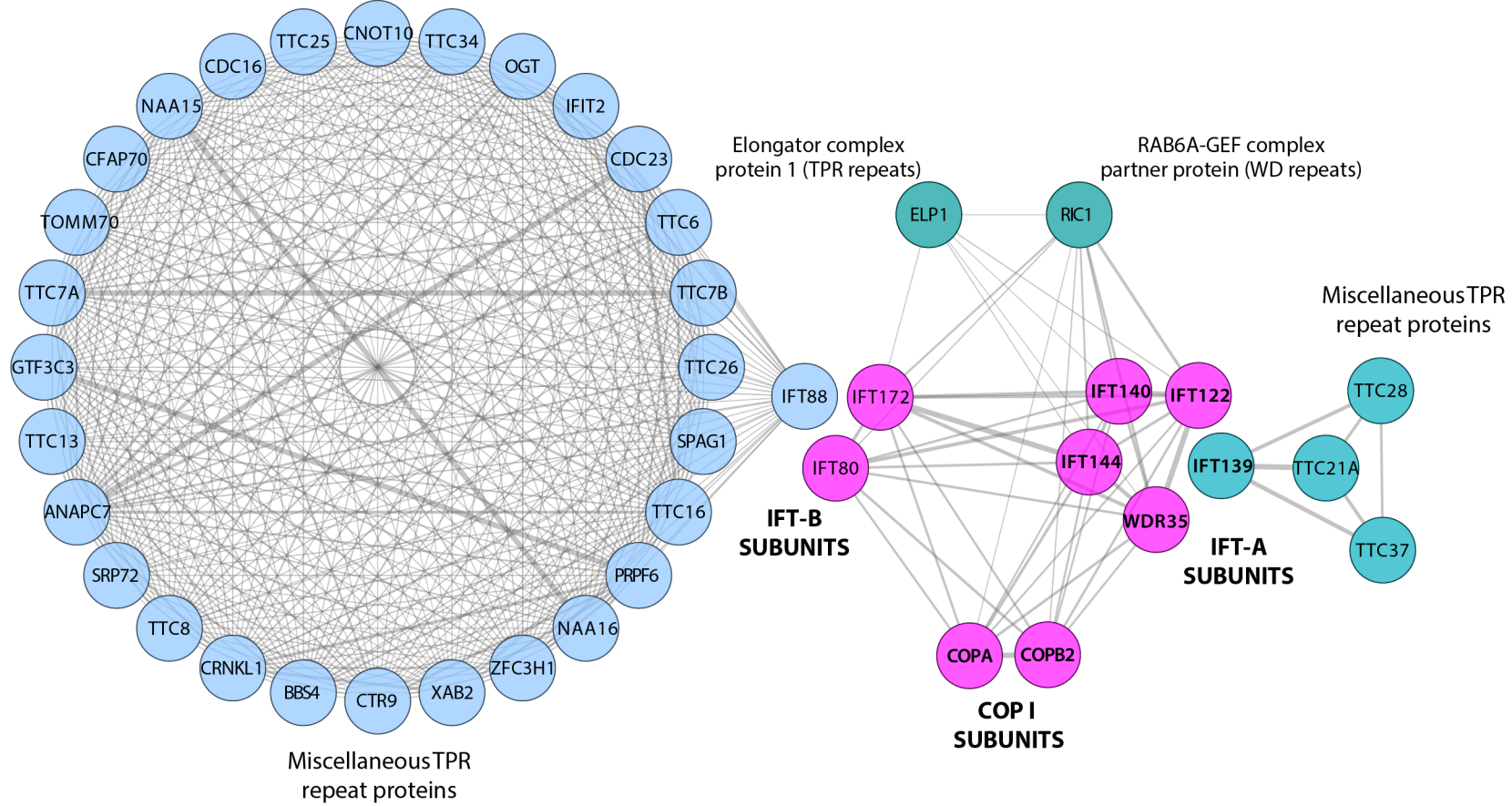
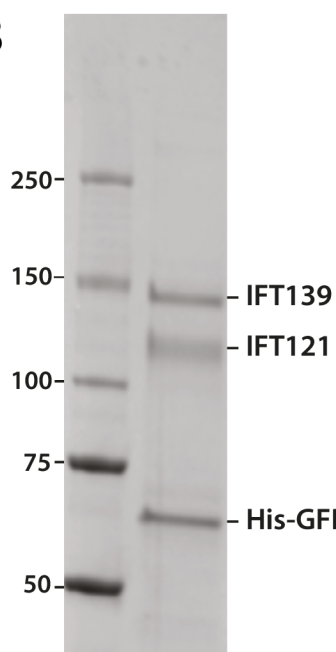
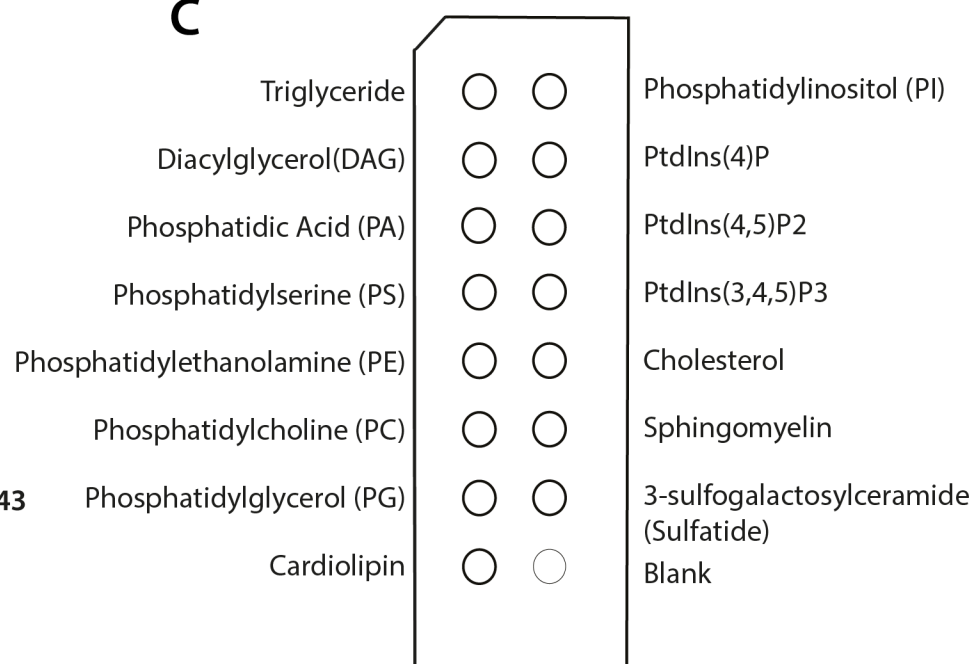
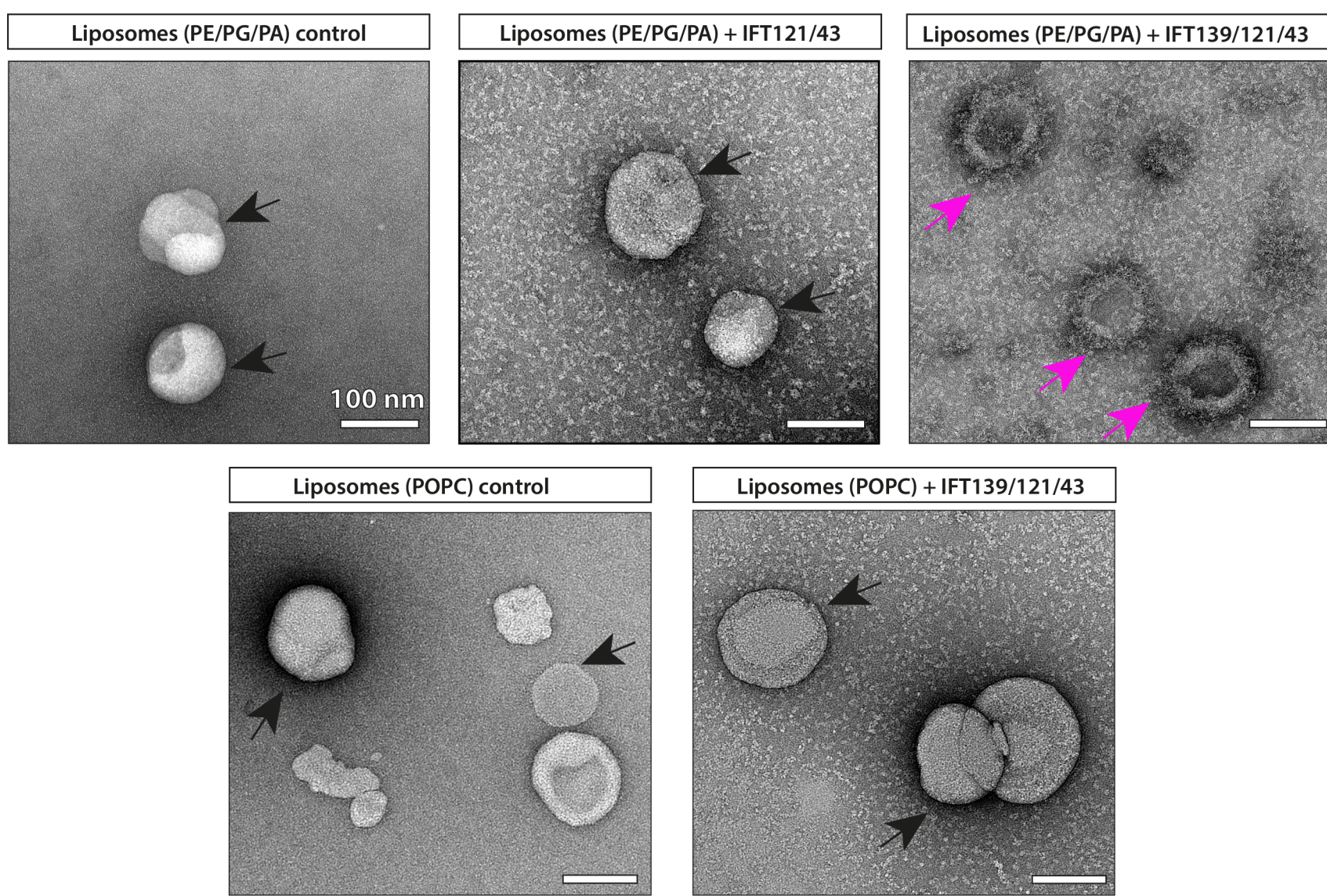
A**B****C****D**

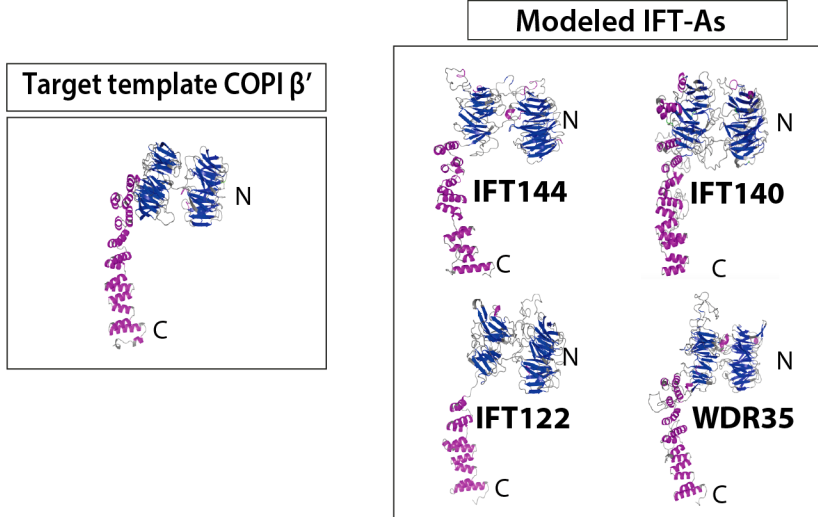
IFTBs	Peptides
IFT172	41
IFT80	9
IFT54	11
IFT20	6
IFT57	10
IFT38	10
IFT88	15
IFT52	5
IFT46	4
IFT22	5
IFT74	28
IFT81	29
IFT56	7
IFT27	3



A**B****C**

A**B****C**

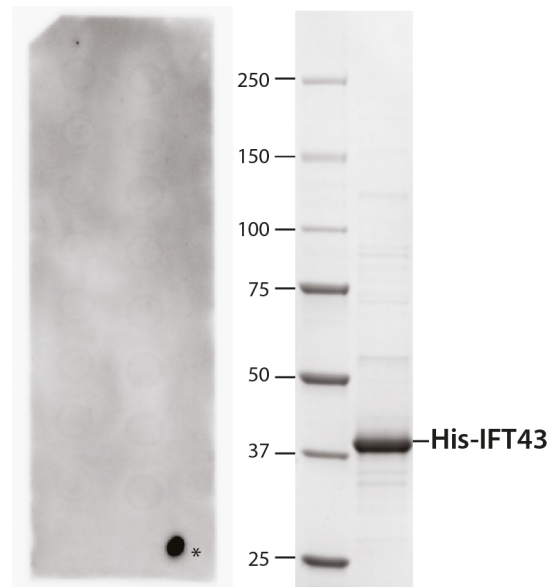
A**B****C****D**

A

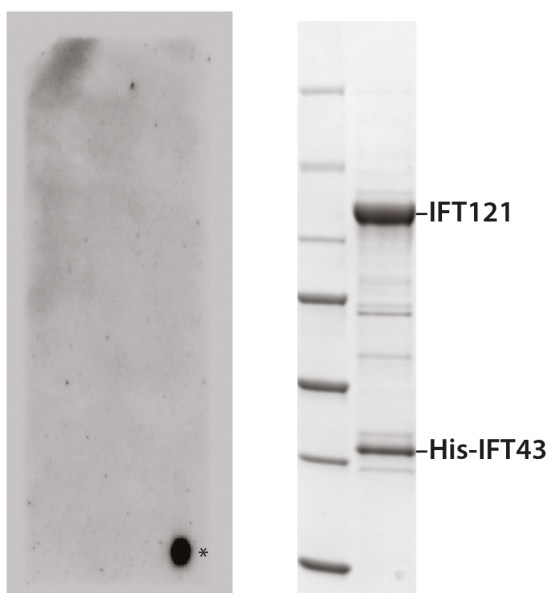
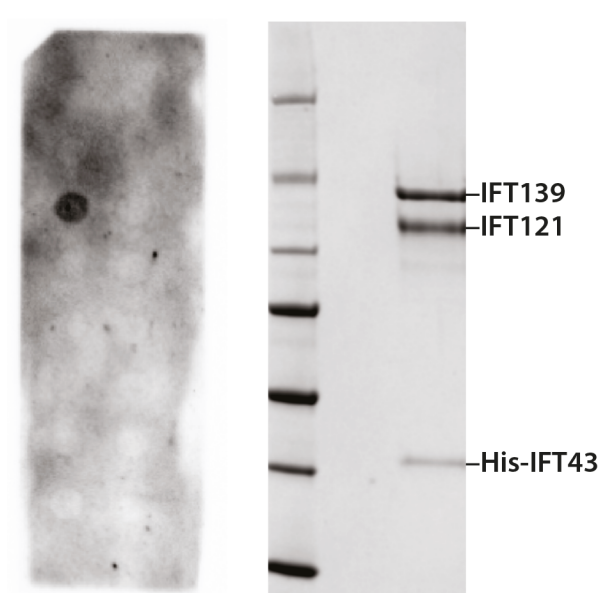
	IFT144	IFT140	IFT122	WDR35
%Sequence identity	14.58	13.38	14.11	12.11
% Sequence similarity	27	27	27	26
%Sequence coverage	51	47	52	60

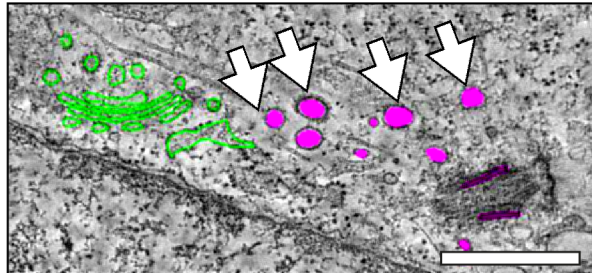
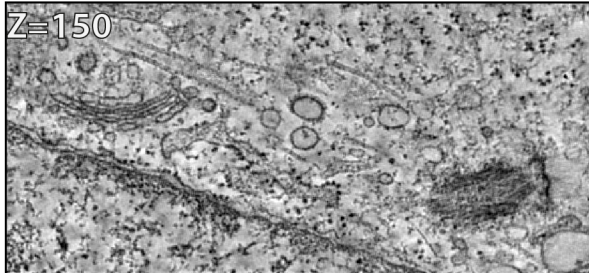
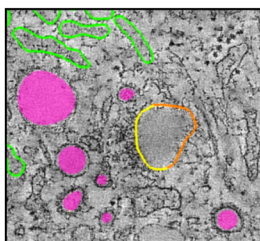
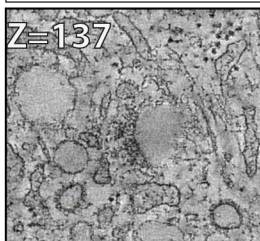
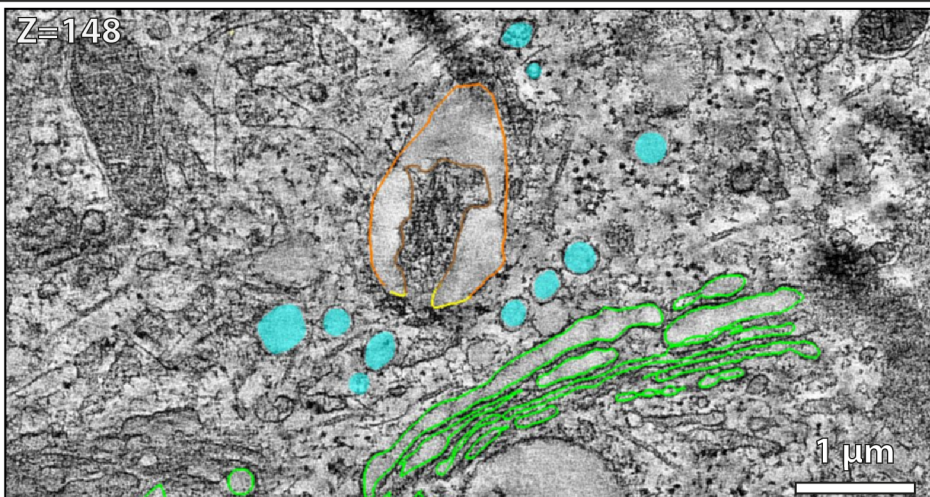
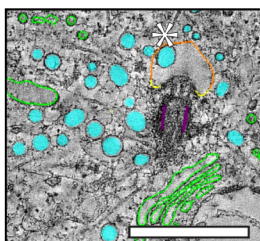
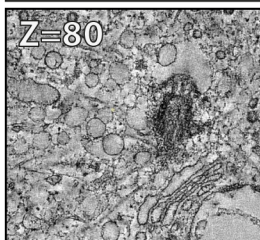
B

Triglyceride	<input type="radio"/>	<input type="radio"/>	Phosphatidylinositol (PI)
Diacylglycerol(DAG)	<input type="radio"/>	<input type="radio"/>	PtdIns(4)P
Phosphatidic Acid (PA)	<input type="radio"/>	<input type="radio"/>	PtdIns(4,5)P2
Phosphatidylserine (PS)	<input type="radio"/>	<input type="radio"/>	PtdIns(3,4,5)P3
Phosphatidylethanolamine (PE)	<input type="radio"/>	<input type="radio"/>	Cholesterol
Phosphatidylcholine (PC)	<input type="radio"/>	<input type="radio"/>	Sphingomyelin
Phosphatidylglycerol (PG)	<input type="radio"/>	<input type="radio"/>	3-sulfogalactosylceramide (Sulfatide)
Cardiolipin	<input type="radio"/>	<input type="radio"/>	Blank

His-IFT43

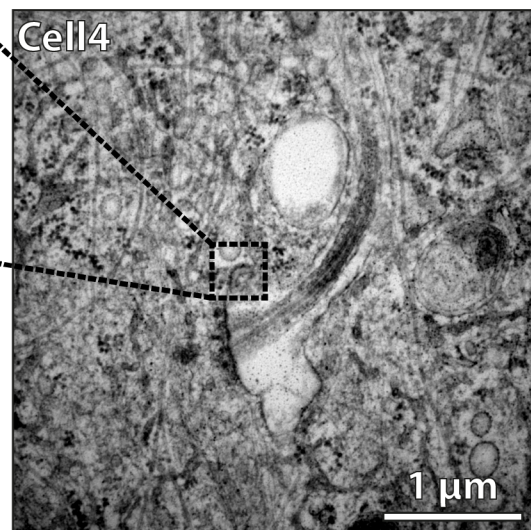
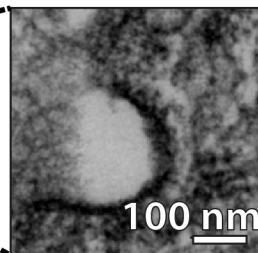
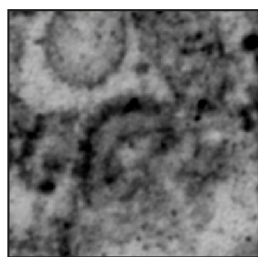
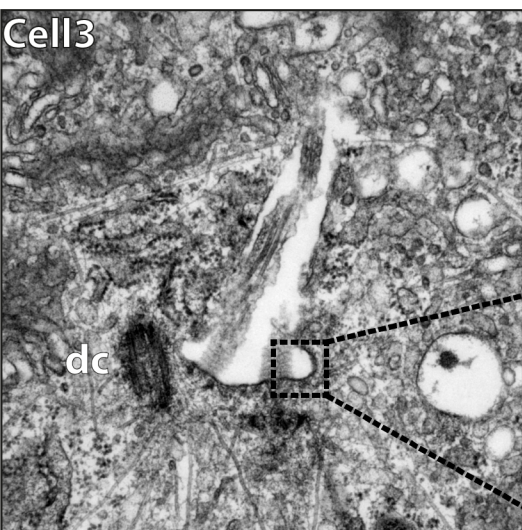
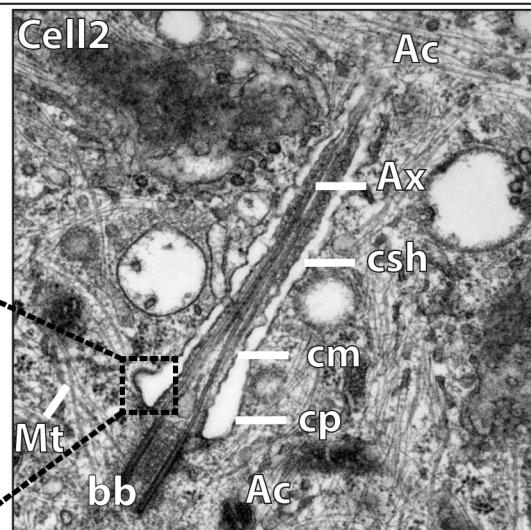
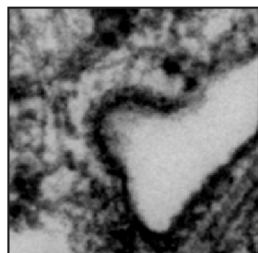
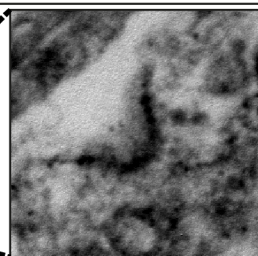
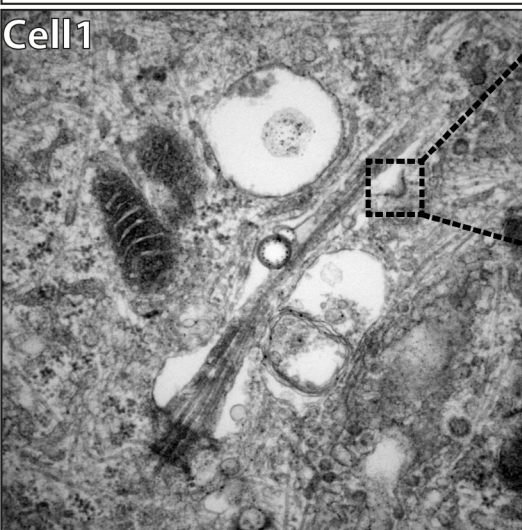
*: Pre-spotted His-IFT43 as positive control.

C**His-IFT43/121****D****His-IFT43/121/139**

A**WT****B****WT****C*****Wdr35*^{-/-}**

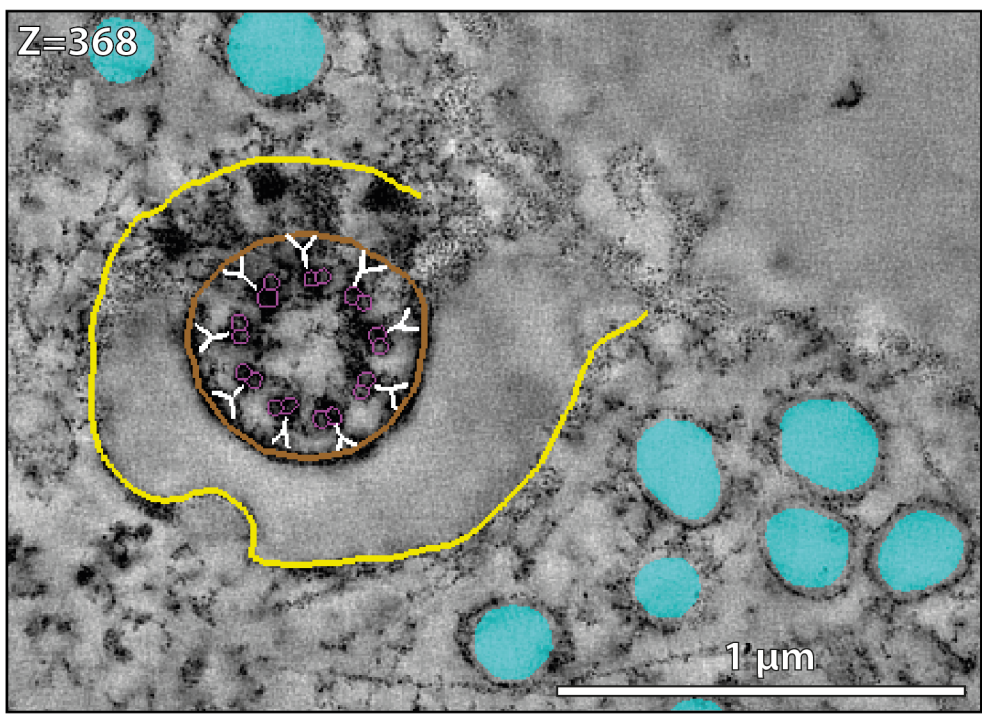
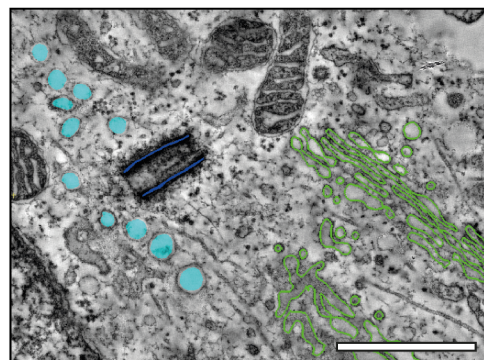
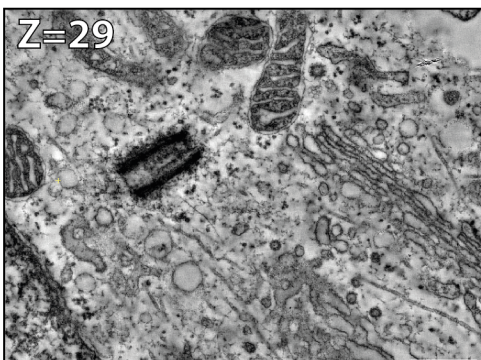
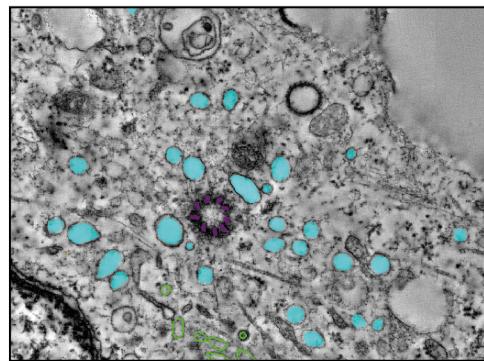
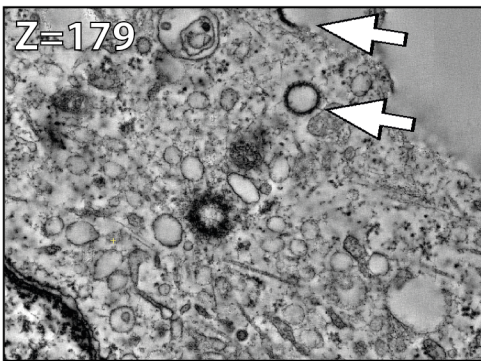
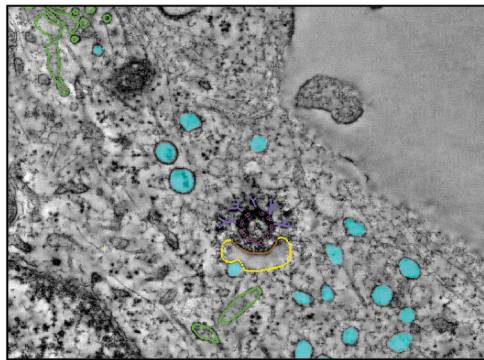
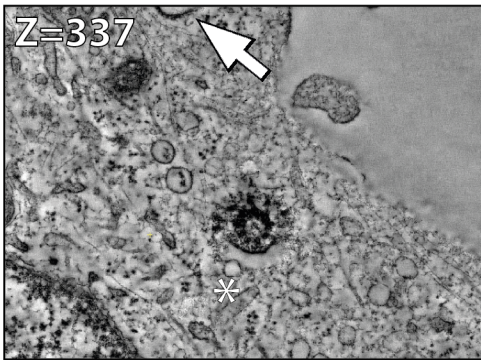
Ciliary membrane Ciliary sheath Ciliary pocket Basal body Golgi
Coated Vesicles Coatless Vesicles

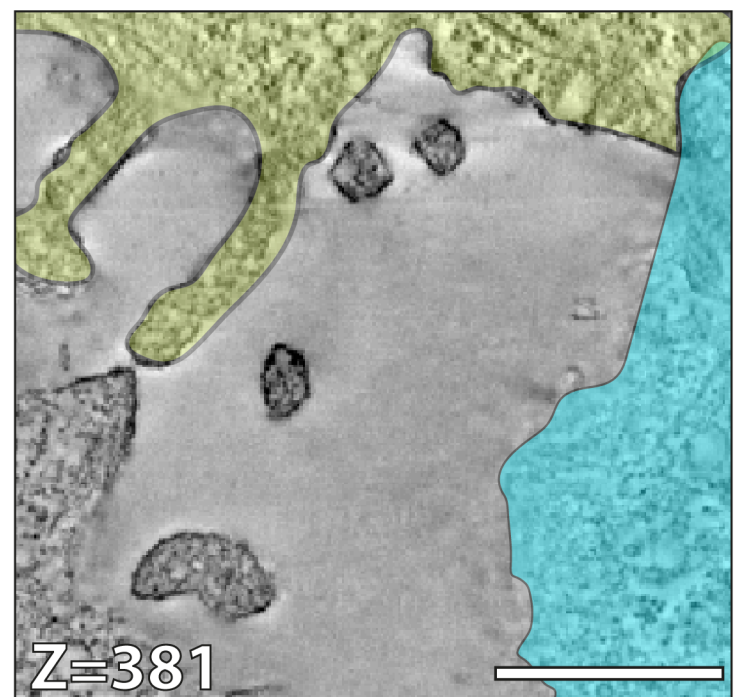
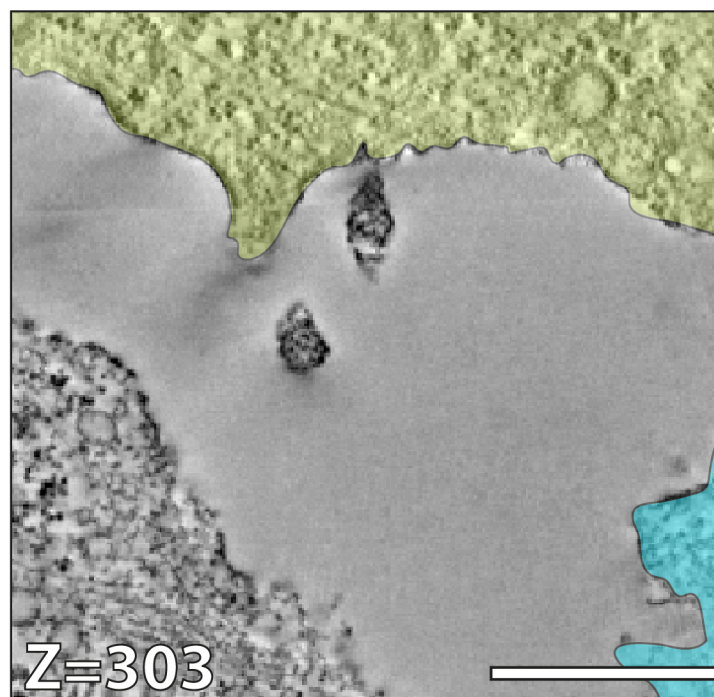
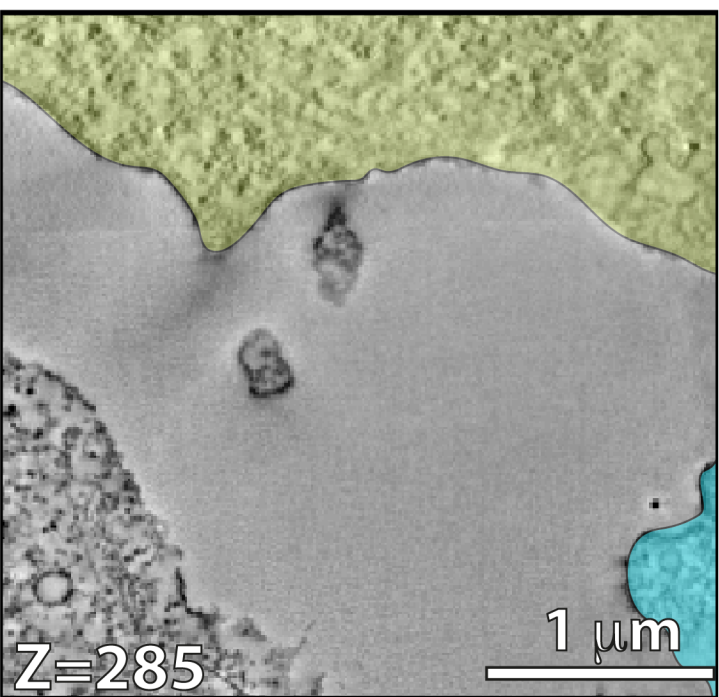
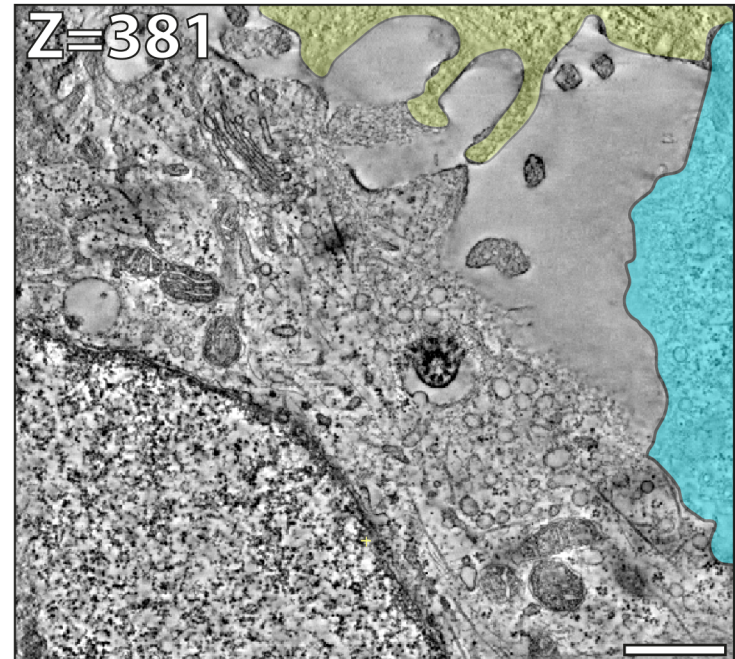
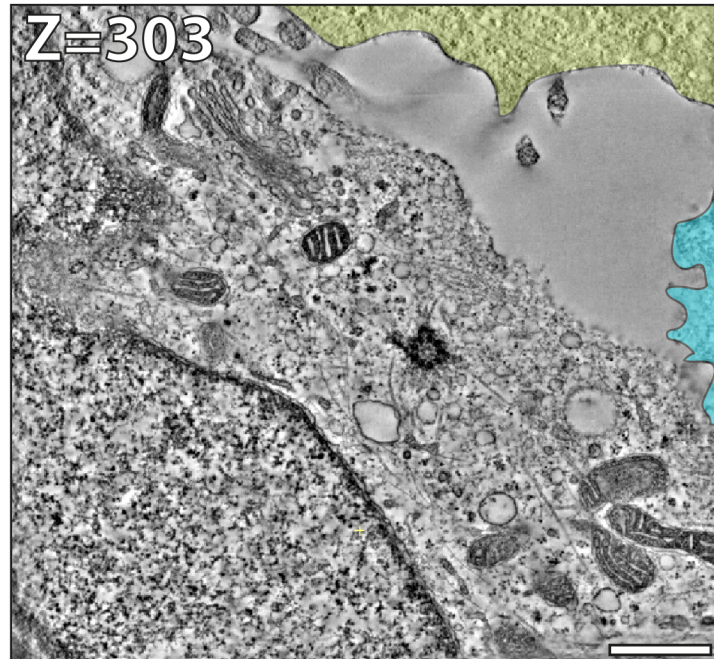
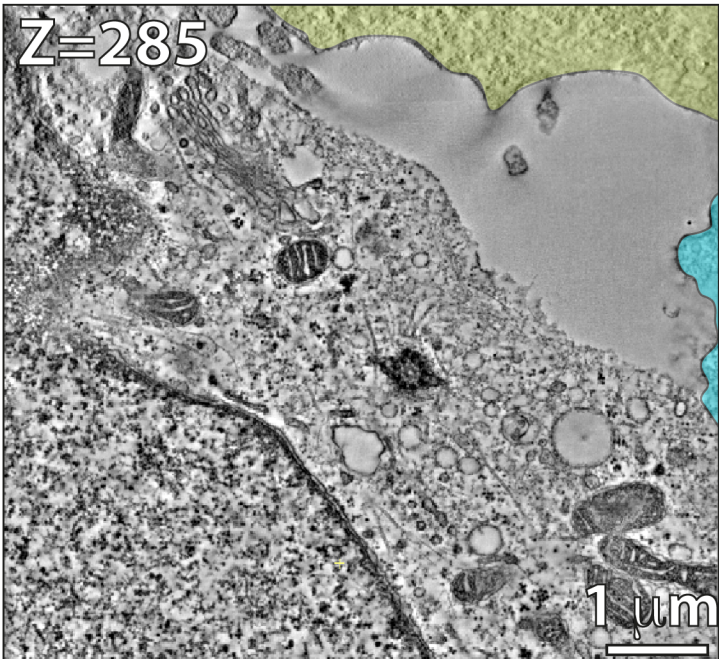
WT

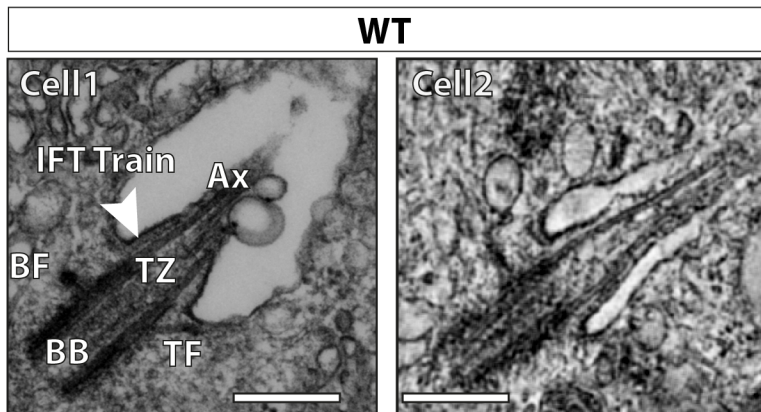
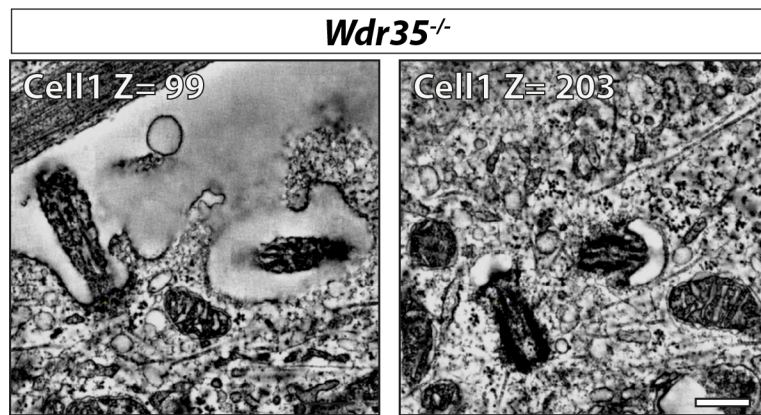
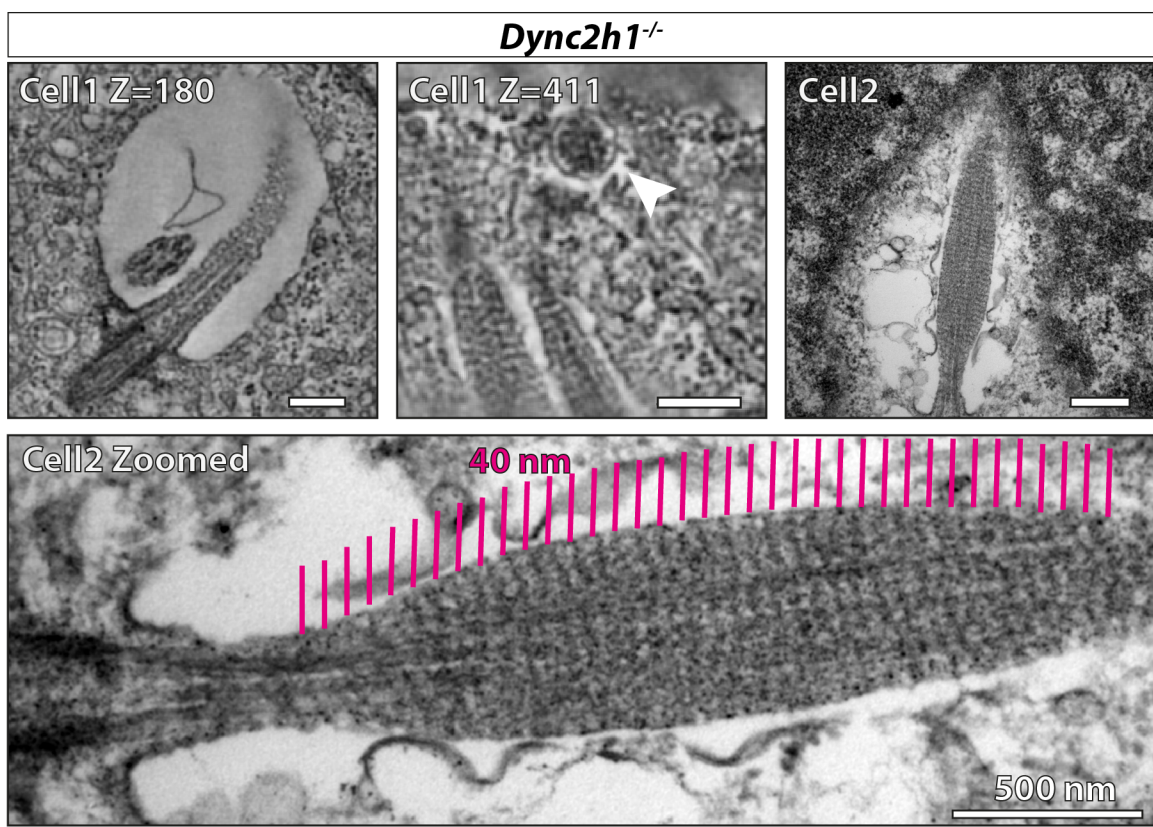


Daughter centriole Basal body Ciliary membrane Ciliary sheath Ciliary pocket
Basal foot Transition fibres Y-links Axoneme Golgi Vesicles lacking electron dense coat

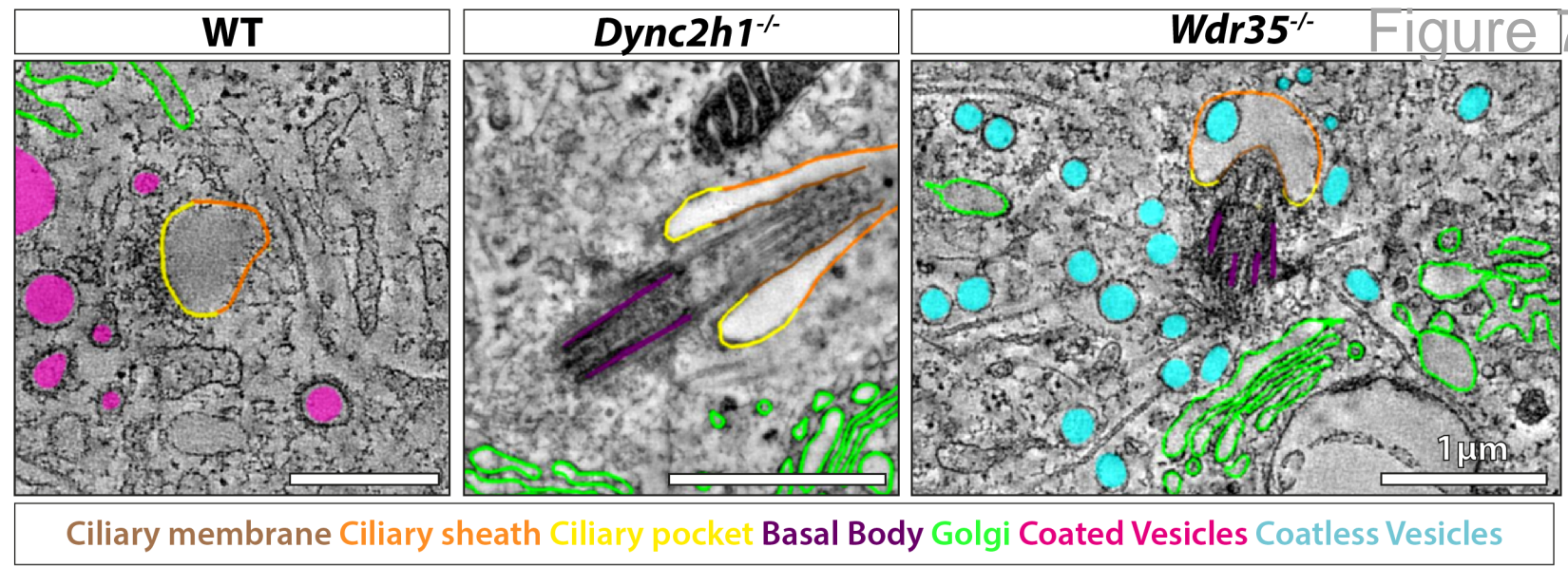
Wdr35^{-/-}



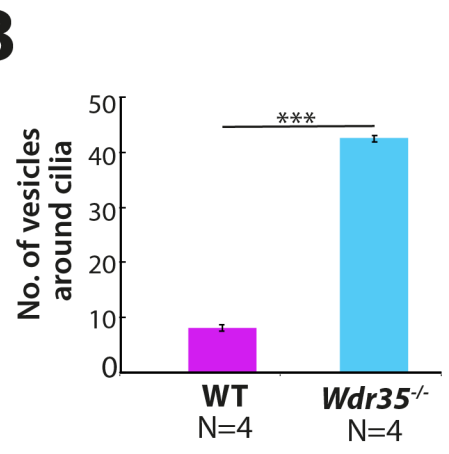


A**B****C**

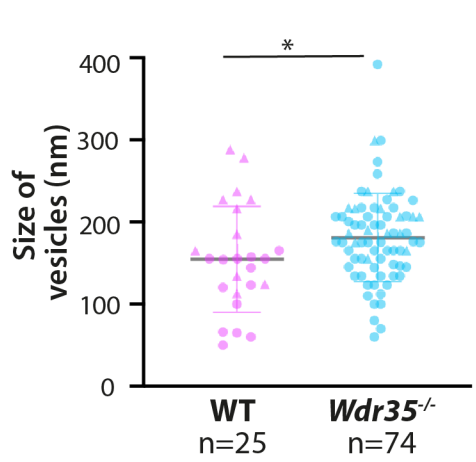
A



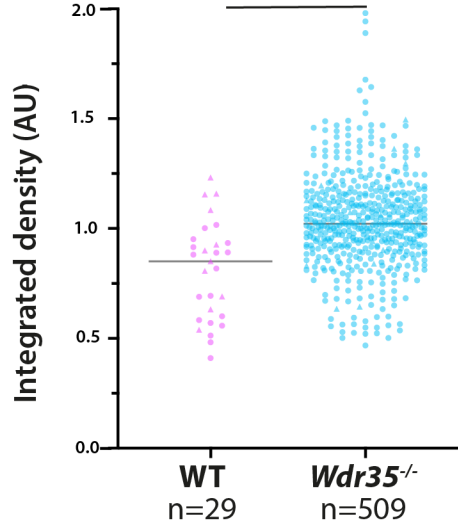
B



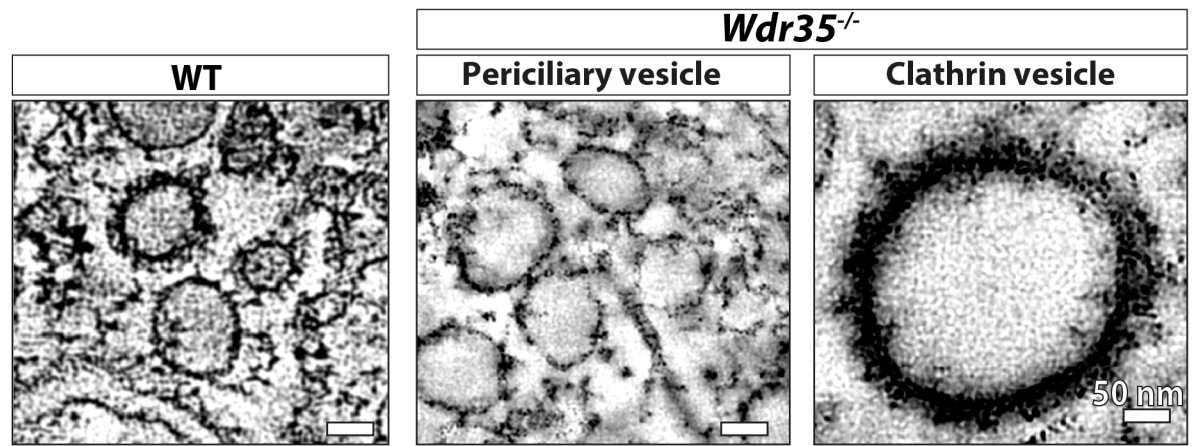
C

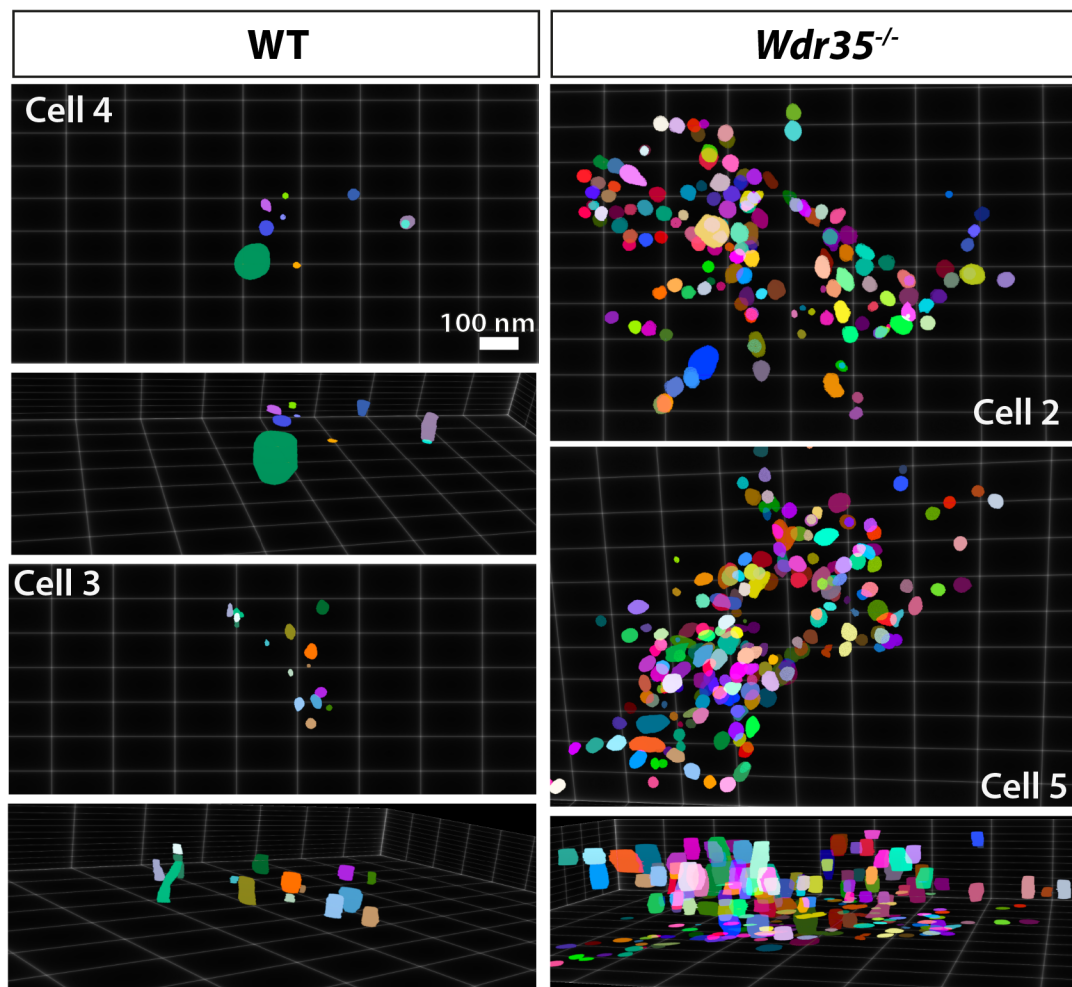
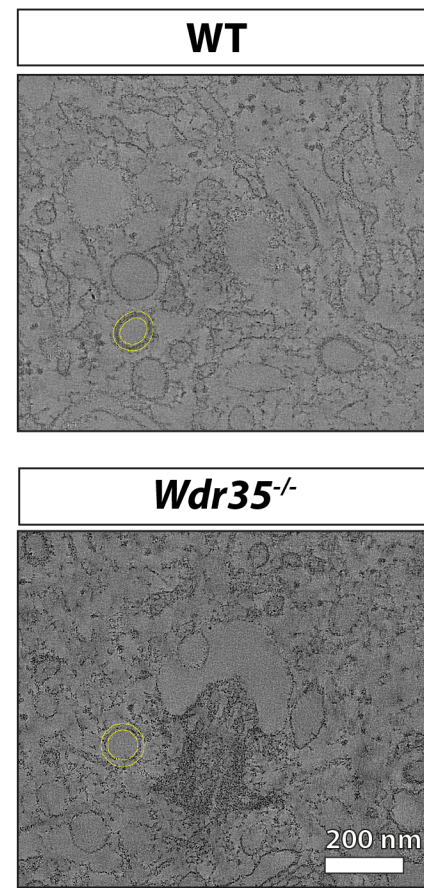
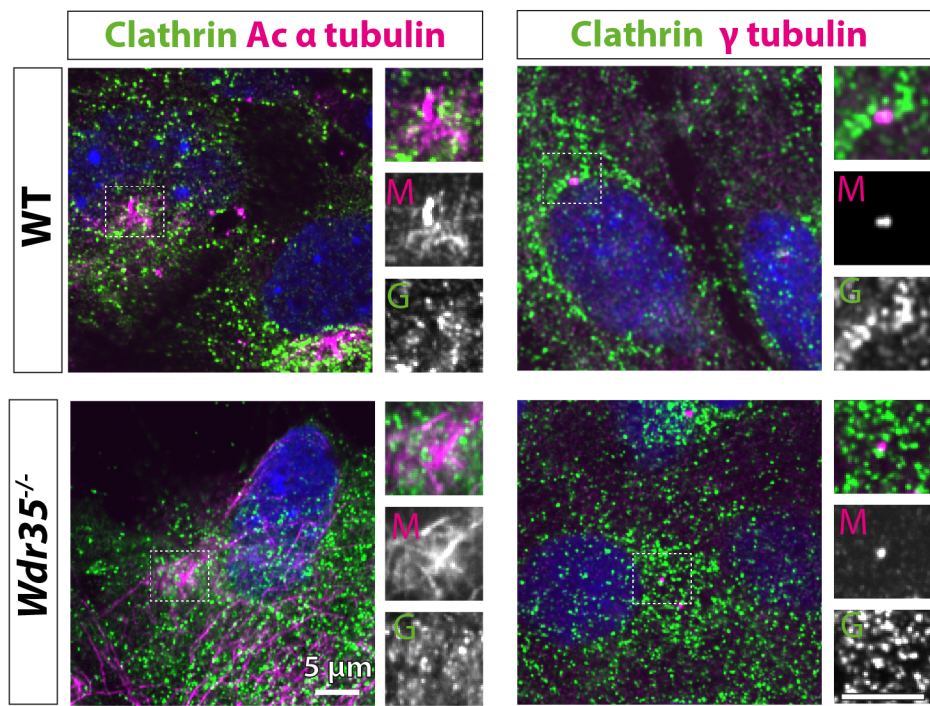
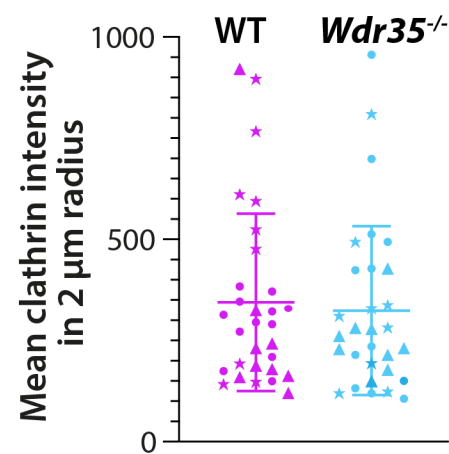


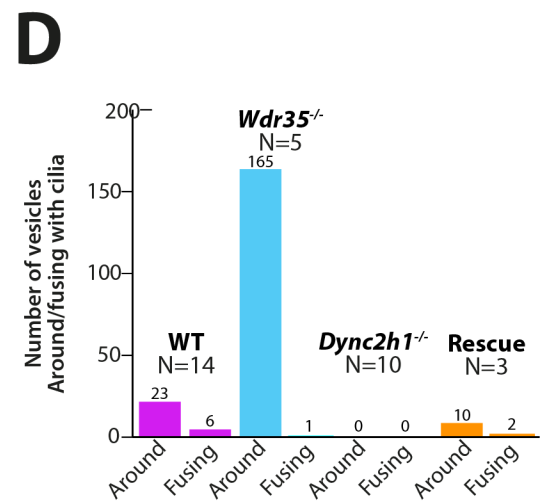
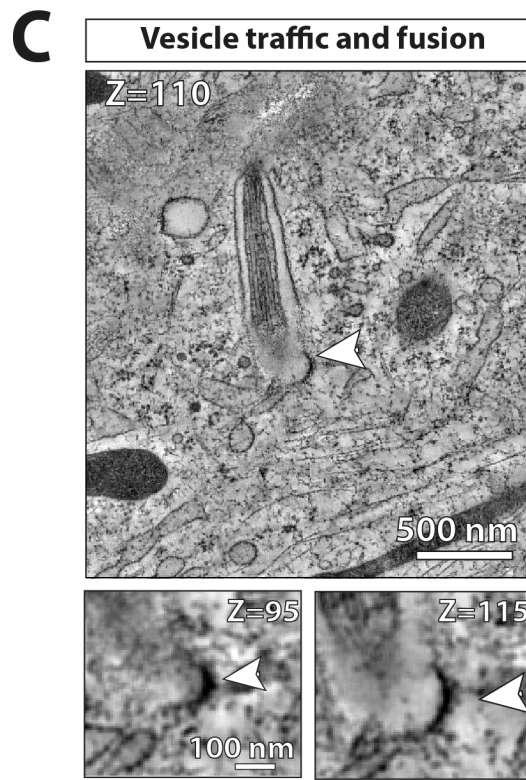
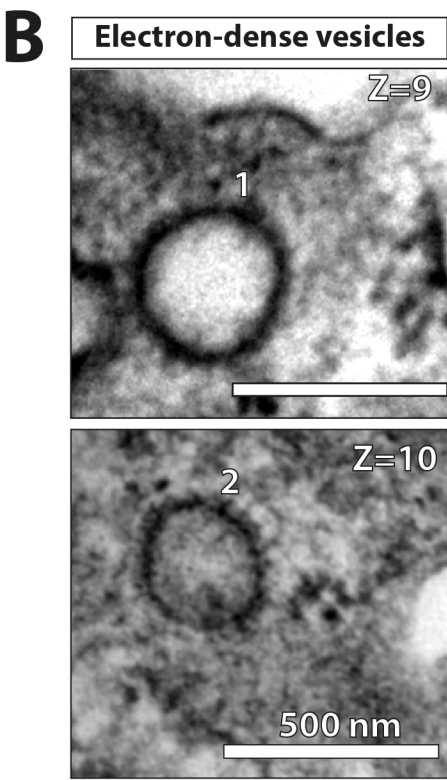
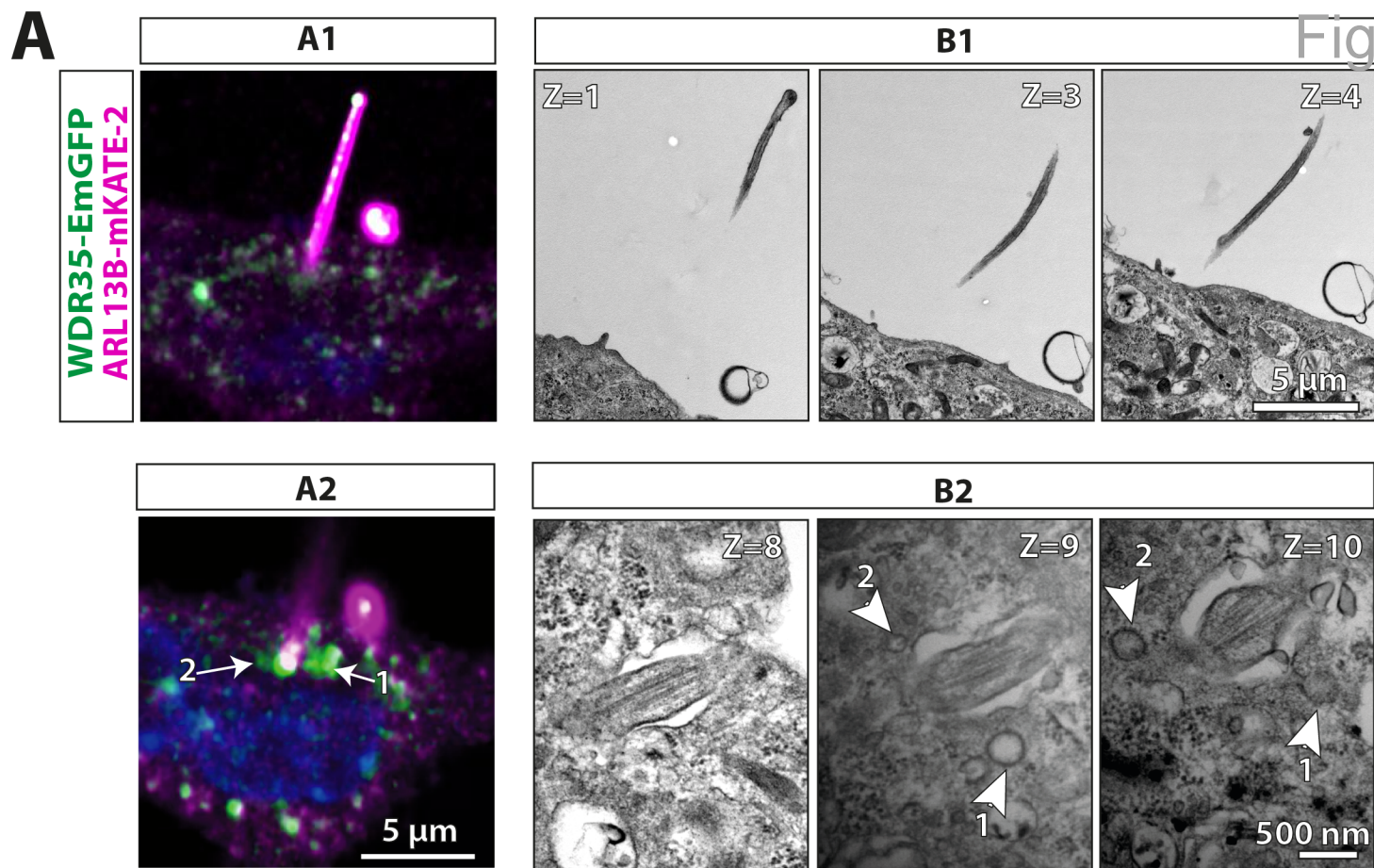
D

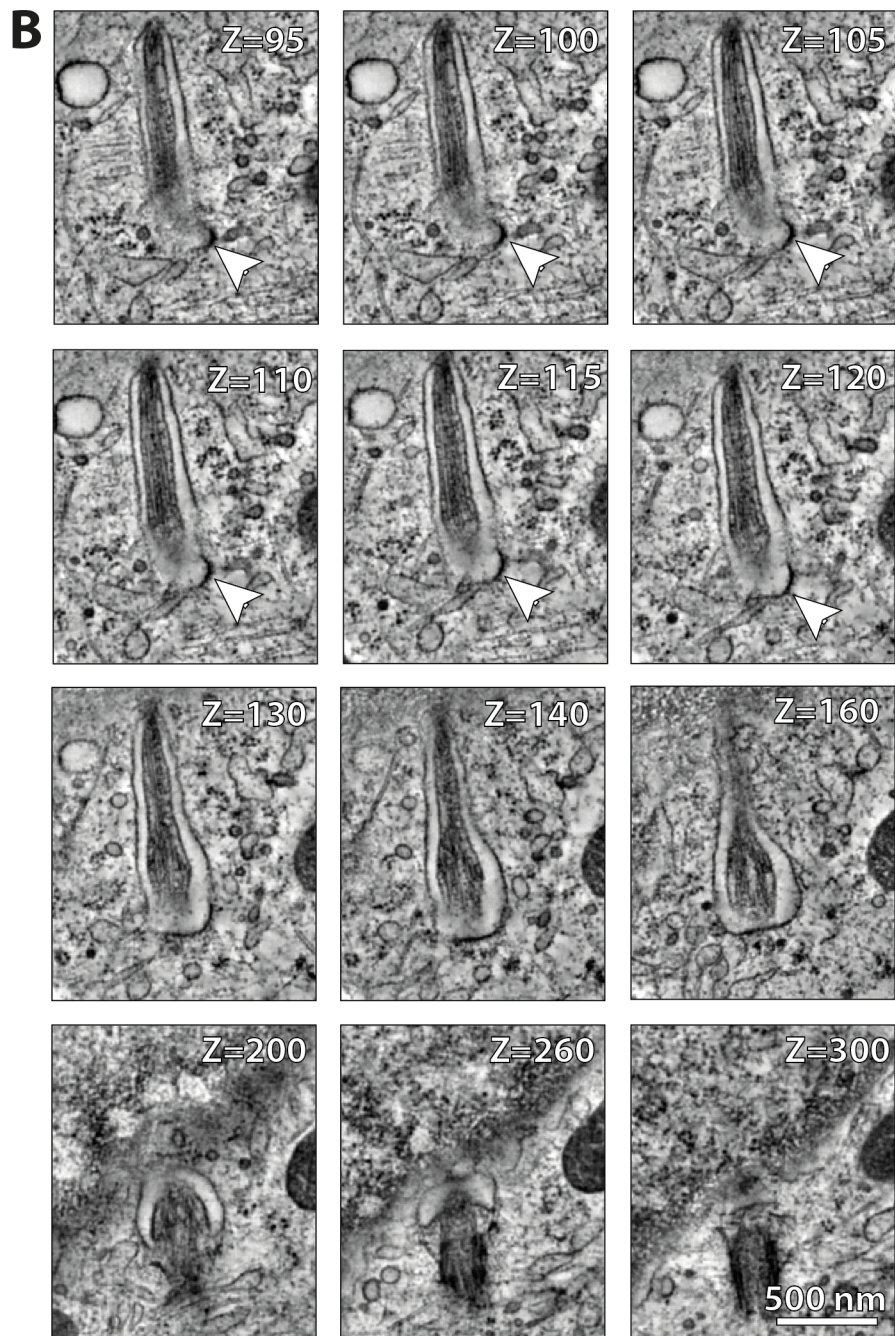
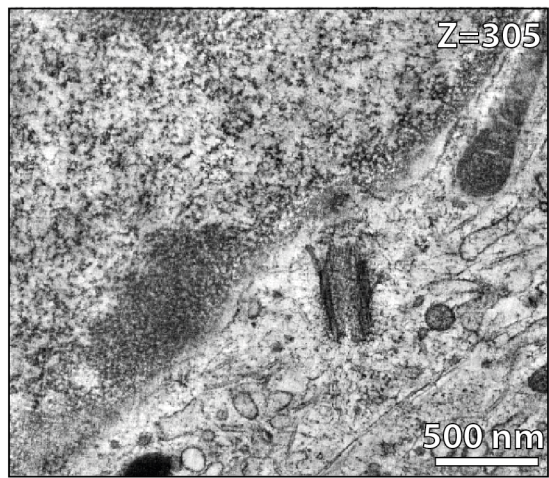
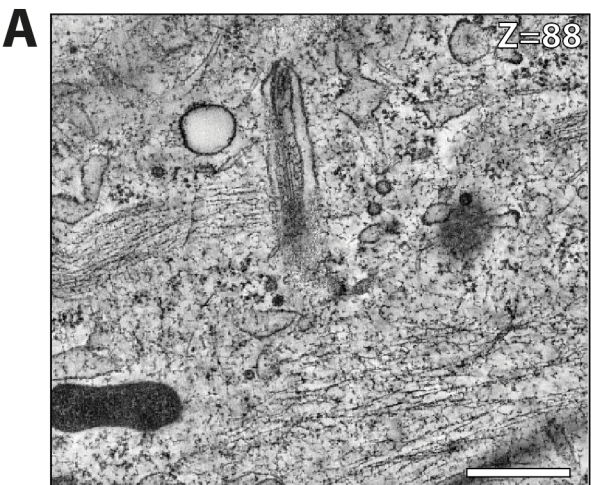


E

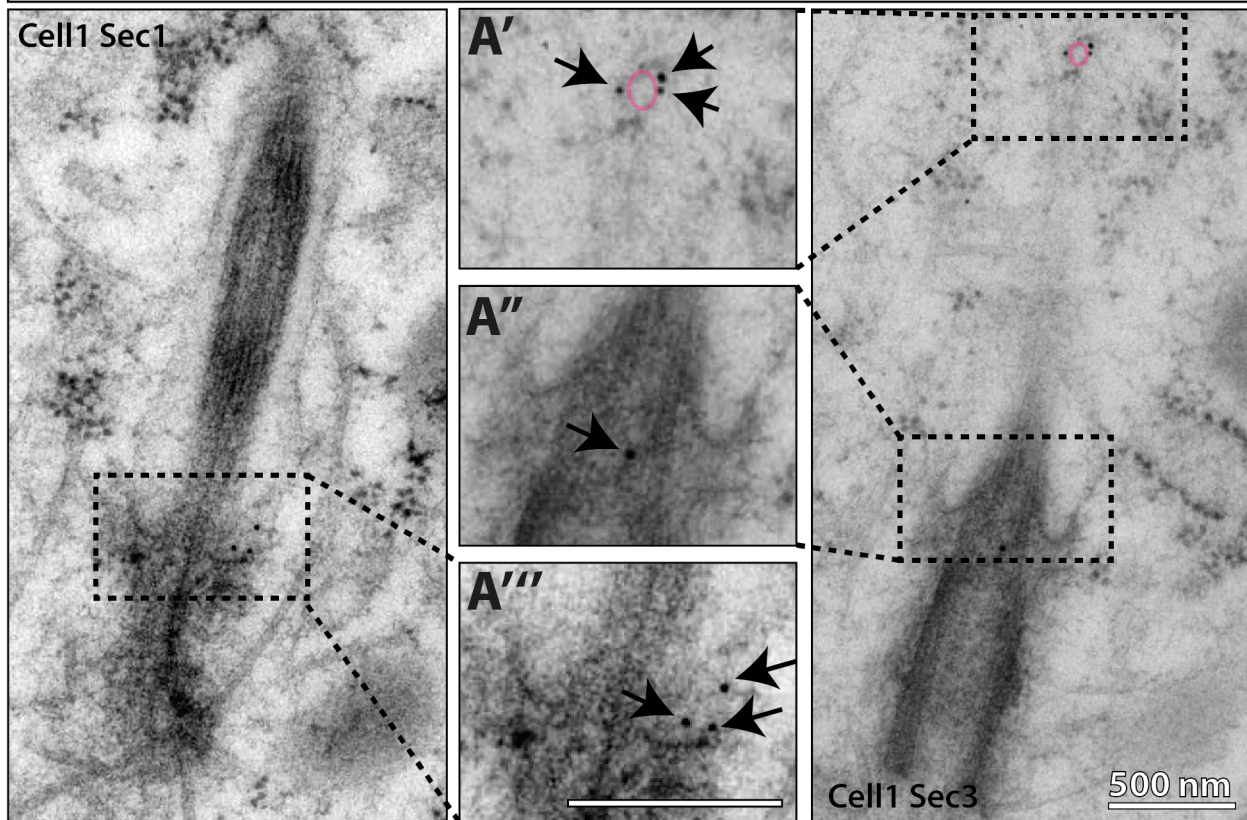


A**B****C****D**

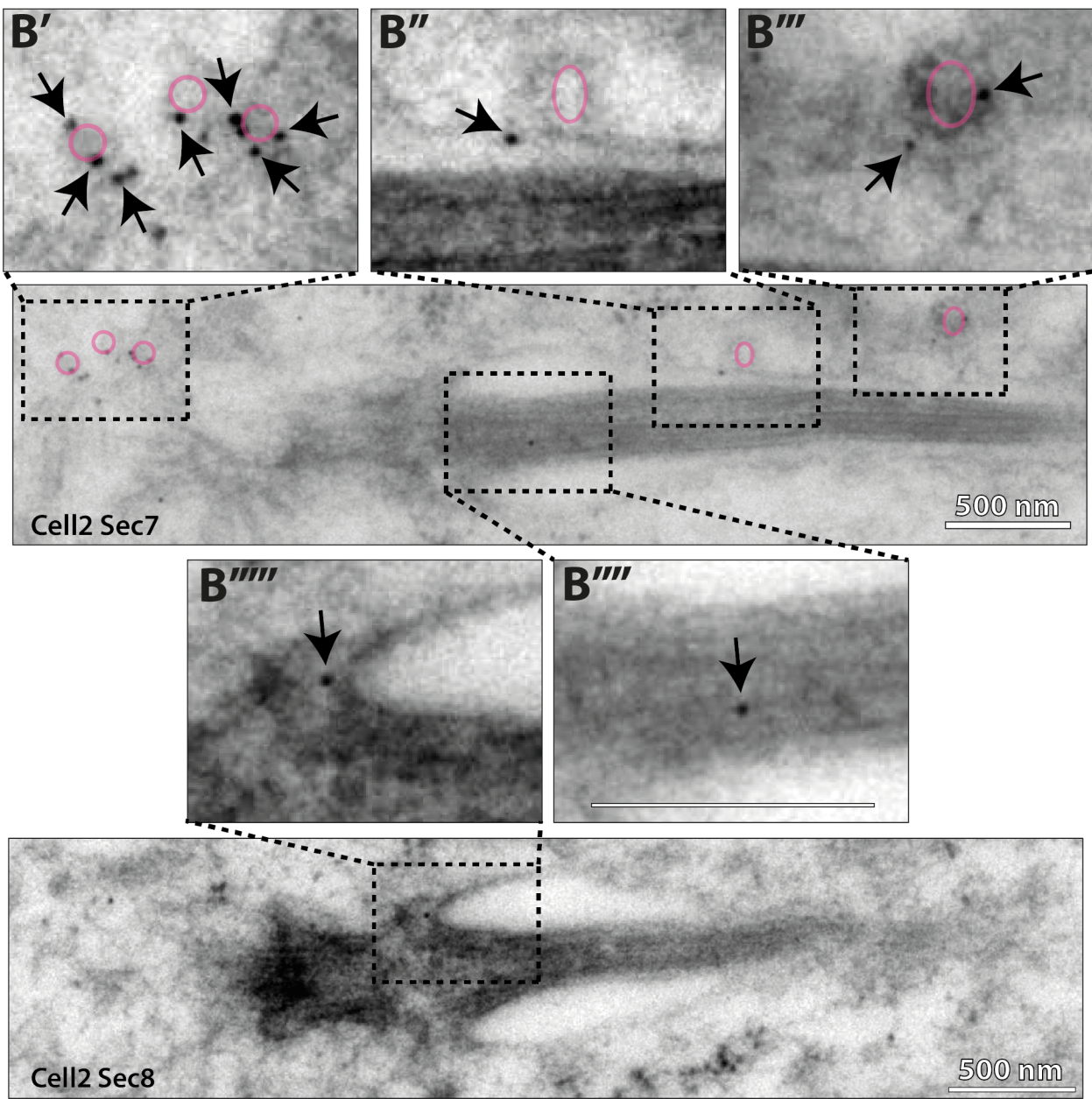


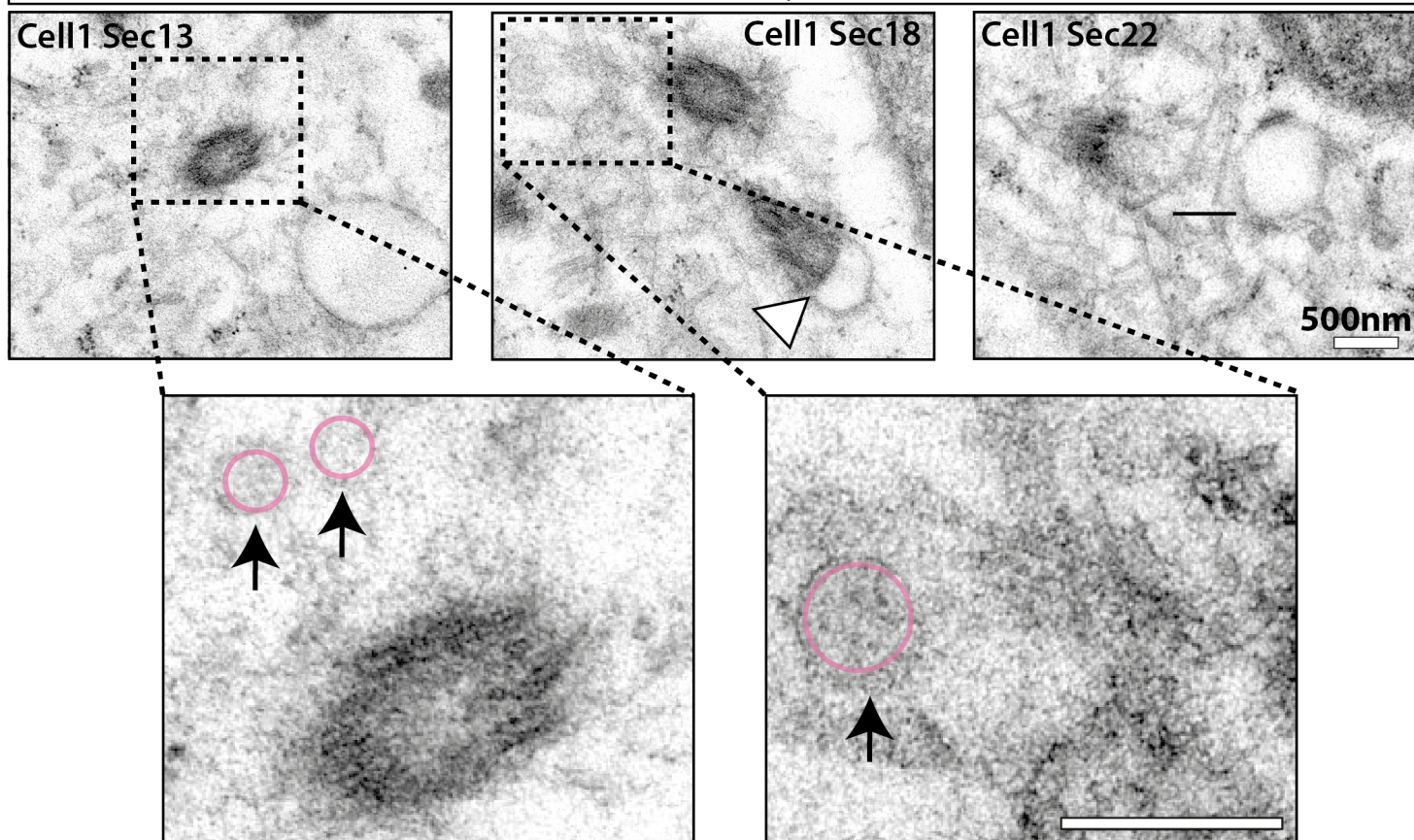
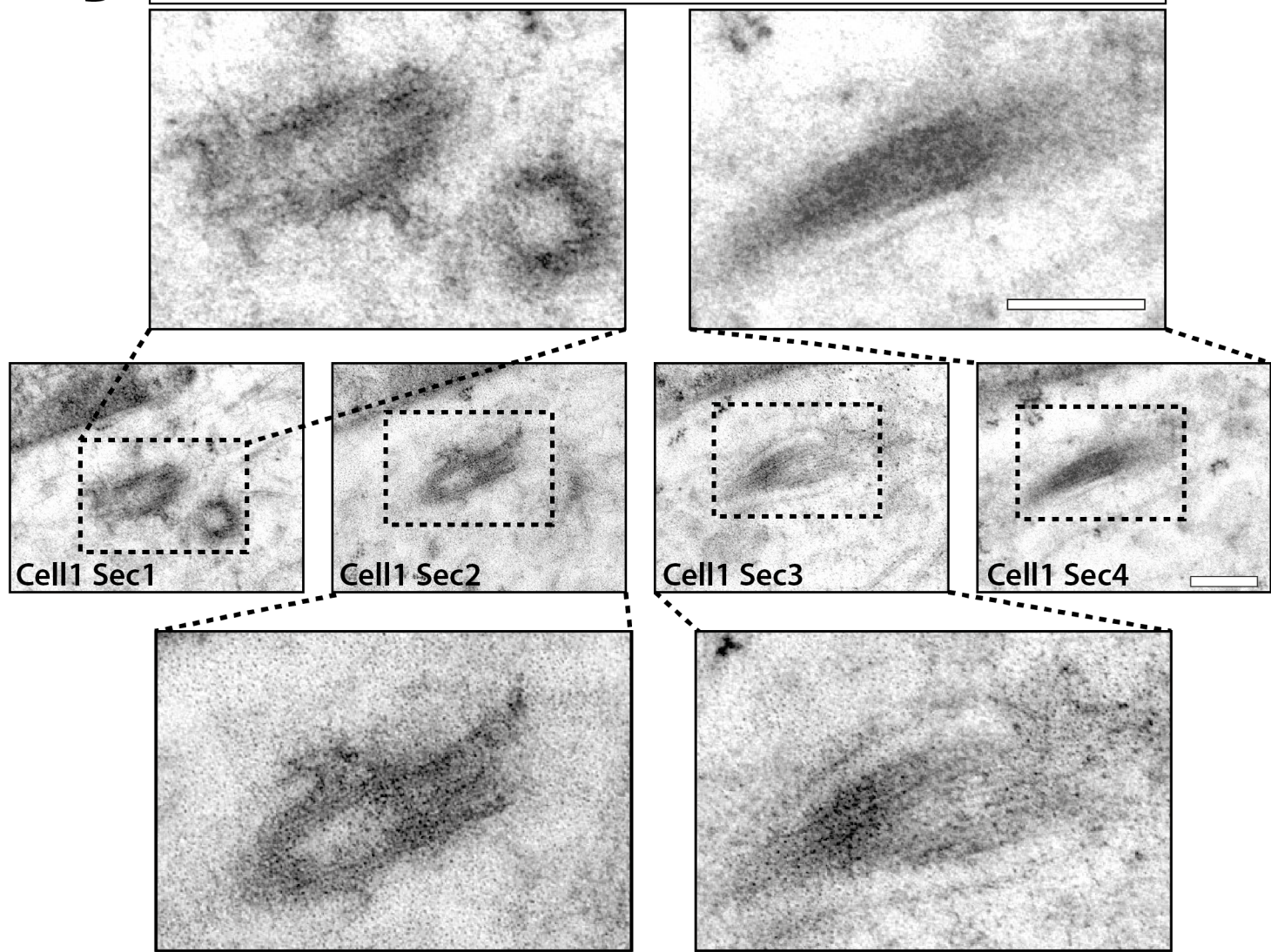


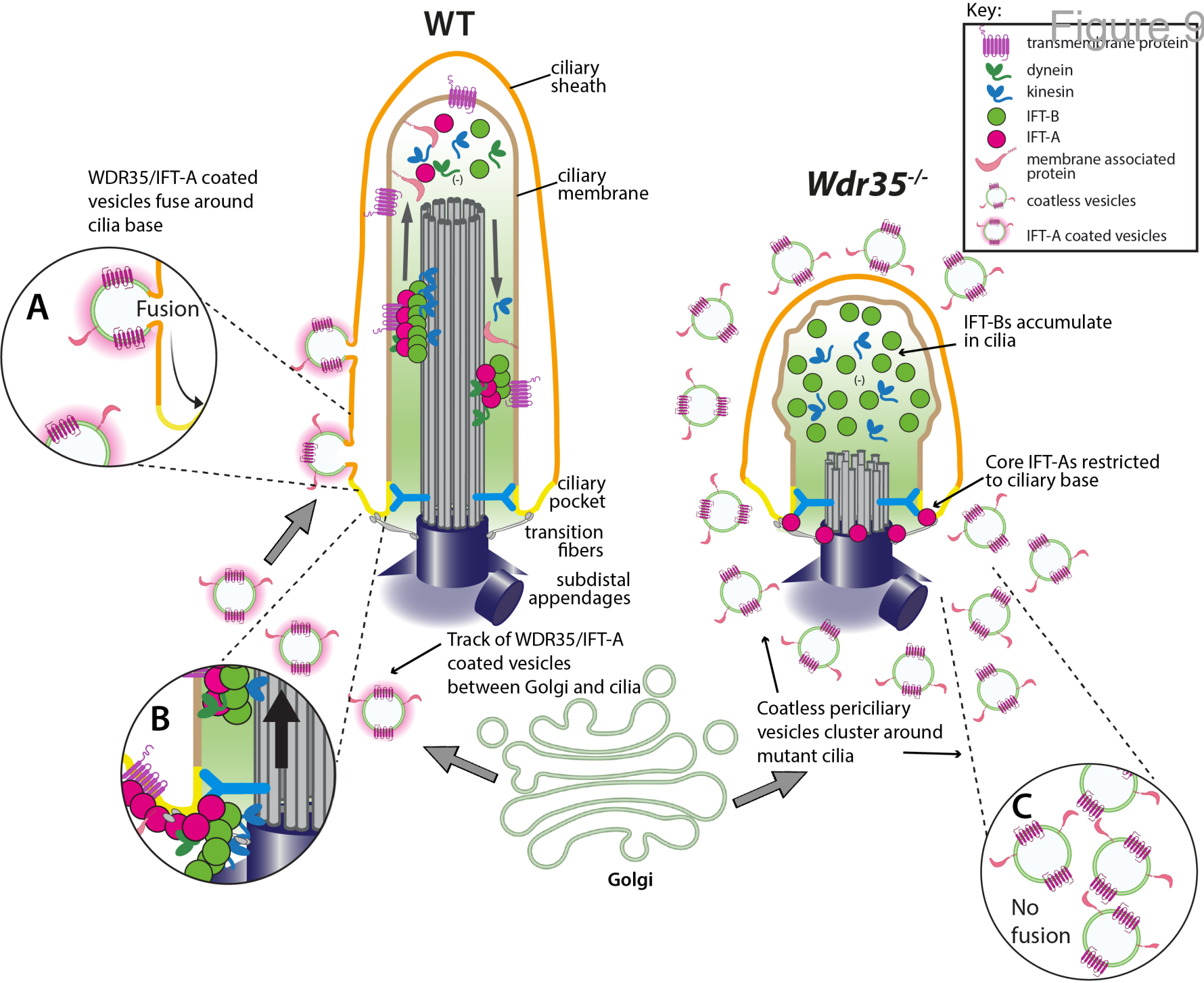
A



B



A*Wdr35*^{-/-} only**B**Secondary only control *Wdr35-EmGFP; Wdr35*^{-/-}



Key Resources Table				
Reagent type (species) or resource	Designation	Source or reference	Identifiers	Additional information
Gene (<i>M. musculus</i>)	<i>Wdr35</i>	Ensembl (GRCm39)	ENSMUSG00000066643 ; MGI:1921932	Also known as: <i>lft121</i> ; <i>4930459M12Rik</i>
Gene (<i>M. musculus</i>)	<i>Dync2h1</i>	Ensembl (GRCm39)	ENSMUSG00000047193 ; MGI:107736	Synonyms: <i>4432416O06Rik</i> , <i>D030010H02Rik</i> , <i>D330044F14Rik</i> , <i>DHC1b</i> , <i>DHC2</i> , <i>Dnchc2</i> , <i>b2b414Clo</i> , <i>m152Asp</i> , <i>m407Asp</i>
Strain, strain background (<i>M. musculus</i>)	C57BL/6J	JAX	664	
Genetic reagent (<i>M. musculus</i>)	<i>Wdr35^{yeti}</i>	(Mill et al. 2011)	MGI:5500169	Synonyms: <i>Wdr35⁻</i>
Genetic reagent (<i>M. musculus</i>)	<i>Dync2h1^{pol}</i>	(Caparrós-Martín et al. 2015)	MGI:6756365	Synonyms: <i>Dync2h1⁻</i>
Genetic reagent (<i>M. musculus</i>)	<i>Pcm1^{SNAP}</i>	This paper		Non-disruptive tagging of endogenous PCM1 with SNAP-tag
Antibody	anti-ARL3 (Rabbit polyclonal)	Proteintech	Cat# 10961-1-AP, RRID:AB_2274220	IF(1:100)

Antibody	anti-ARL13B (Rabbit polyclonal)	Proteintech	Cat# 17711-1-AP, RRID:AB_2060867	IF(1:100)
Antibody	anti-Acetylated α -tubulin (Mouse monoclonal)	Sigma	6-11B-1; Cat# T6793, RRID: AB_477585	IF(1:1000)
Antibody	anti-Acetylated α -tubulin (Rabbit monoclonal)	Abcam	Cat# ab179484, RRID:AB_2890906	IF(1:1000)
Antibody	anti- γ -tubulin (Mouse monoclonal)	Sigma	GTU-88; Cat# T6557, RRID:AB_477584	IF(1:100)
Antibody	anti- γ -tubulin (Rabbit polyclonal)	Abcam	Cat# ab11317, RRID:AB_297921	IF(1:100)
Antibody	anti-GFP (Mouse monoclonal)	Roche	Cat# ab6556, RRID:AB_390913	IF(1:1000) WB (1:1000)
Antibody	anti-GFP (Rabbit polyclonal)	Abcam	Cat# ab11317, RRID:AB_305564	IF(1:1000) WB(1:1000) ImEM (1:20)
Antibody	anti-GFP (Rabbit polyclonal)	Santa Cruz	Cat# sc-8334, RRID:AB_641123	WB(1:5000)
Antibody	anti-His (Mouse monoclonal)	GenScript	Cat# A00186, RRID:AB_914704	WB(1:2500), Strip binding assay

Antibody	anti- IFT43 (Rabbit polyclonal)	Custom made, Victor Ruiz-Perez, University of Madrid	(Caparrós-Martín et al. 2015)	WB(1:2000) IF(1:200)
Antibody	anti- IFT81 (Rabbit polyclonal)	Proteintech	Cat# 11744-1-AP, RRID:AB_2121966	WB(1:1000) IF(1:200)
Antibody	anti- IFT88 (Rabbit polyclonal)	Proteintech	Cat# 13967-1AP, RRID:AB_2121979	WB(1:1000) IF(1:200)
Antibody	anti- IFT121 (Rabbit polyclonal)	Custom made, Mill lab, Proteintech	This paper, RRID:AB_2893313	WB(1:50)
Antibody	anti- IFT122 (Rabbit polyclonal)	Proteintech	Cat# 19304-1-AP, RRID:AB_2714184	WB(1:1000) IF(1:200)
Antibody	anti- IFT122 (Rabbit polyclonal)	Aviva	Cat# 19304-1-AP, RRID:AB_1294343	WB(1:1000)
Antibody	anti- IFT139 (Rabbit polyclonal)	Novus	Cat# NBP1-90416, RRID:AB_11043797	WB(1:2000) IF(1:200)
Antibody	anti- IFT140 (Rabbit polyclonal)	Proteintech	Cat# 17460-1-AP, RRID:AB_2295648	WB(1:1000) IF(1:200)

Antibody	anti- IFT144 (Rabbit polyclonal)	Proteintech	Cat# 13647-1-AP, RRID:AB_10598484	WB(1:1000) IF(1:200)
Antibody	anti- MKS1 (Rabbit polyclonal)	Proteintech	Cat# 16206-1-AP, RRID:AB_10637856	IF(1:100)
Antibody	anti- NPHP1 (Rabbit polyclonal)	Custom made, Gift from Greg Pazour, University of Massachusetts	640	IF(1:100)
Antibody	anti- PCM1 (Rabbit polyclonal)	Proteintech	Cat# 19856-1-AP, RRID:AB_2878616	IF(1:100)
Antibody	anti- Rootletin (Goat polyclonal)	Santa Cruz	Cat# sc-67828, RRID:AB_2085505	IF(1:100)
Antibody	anti- SNAP (Rabbit polyclonal)	New England Biolabs	Cat# P9310S, RRID:AB_10631145	IF(1:300)
Antibody	anti- Mouse IgG, HRP-conjugated secondary antibody (Sheep polyclonal)	GE Healthcare	Cat# NA931-1ML, RRID:AB_772210	WB(1:10000)
Antibody	anti- Mouse IgG, HRP-conjugated secondary antibody (Rabbit polyclonal)	Dako	Cat# P0260, RRID:AB_2636929	WB(1:1000), Strip overlay assays

Antibody	anti- Rabbit IgG, HRP-conjugated secondary antibody (Goat polyclonal)	GE Healthcare	Cat# RPN4301, RRID:AB_2650489	WB(1:10000)
Antibody	anti- Rabbit Light-chain specific, HRP-conjugated secondary antibody (Mouse monoclonal)	Millipore	Cat# MAB201P, RRID:AB_827270	WB(1:10000)
Antibody	anti- Rabbit IgG, Light-chain specific secondary antibody (Mouse monoclonal)	Cell Signaling Technology	Cat# 3677, RRID:AB_1549610	WB(1:10000)
Antibody	anti- Goat IgG, Alexa488, 594, 647 connjugated secondary antibodies (Donkey polyclonal)	Molecular Probes	Cat# A-11055, RRID:AB_2534102 Cat# A-11058, RRID:AB_2534105 Cat# A-21447, RRID:AB_2535864	IF(1:500)
Antibody	anti- Mouse IgG, Alexa488, 594, 647 connjugated secondary antibodies (Donkey polyclonal)	Molecular Probes	Cat# A-21202, RRID:AB_141607 Cat# R37115, RRID:AB_2556543 Cat# A32787, RRID:AB_2762830	IF(1:500)
Antibody	anti- Rabbit IgG, Alexa488, 594, 647 connjugated secondary antibodies (Donkey polyclonal)	Molecular Probes	Cat# A-21206, RRID:AB_2535792 Cat# A-21207, RRID:AB_141637 Cat# A-31573, RRID:AB_2536183	IF(1:500)
Antibody	anti- Rabbit IgG, 10 nm gold conjugated (Goat	BBI Solutions	Cat# EM GAR10/0.25, RRID:AB_1769128	IF(1:500)

	polyclonal)			
Recombinant DNA reagent	pmKate2-Arl13b (plasmid)	(Diggle et al. 2014)		Mouse <i>Arl13b</i> cDNA with a C-terminal fusion of mKate2
Recombinant DNA reagent	ARL13B-EGFP (plasmid)	(Hori et al. 2008)		Human <i>ARL13B</i> cDNA with a C-terminal fusion of EGFP
Recombinant DNA reagent	pEGFP-N1 (plasmid)	Clontech 6085-1	(Hori et al. 2008)	EGFP expression vector as control
Recombinant DNA reagent	Ift122-EGFP (plasmid)	(Qin et al. 2011)		Mouse <i>Ift122</i> cDNA with a C-terminal EGFP tag
Recombinant DNA reagent	MyrPalm-GFP (plasmid)	(Williams et al. 2014)		Lipid-anchored GFP construct generated by annealing oligonucleotides encoding the 13 amino-terminal residues from Lyn kinase (MyrPalm), into the KpnI and AgeI sites of pEGFP-N1 (Clontech).
Recombinant DNA reagent	PalmPalm-GFP (plasmid)	(Williams et al. 2014)		Lipid-anchored GFP construct generated by annealing oligonucleotides encoding the 20 N-terminal residues from GAP43 (PalmPalm) into the KpnI and AgeI sites of pEGFP-N1 (Clontech).

Recombinant DNA reagent	pEGFP-mSmo (plasmid)	(Williams et al. 2014)	Addgene plasmid # 25395 ; http://n2t.net/addgene:25395 ; RRID:Addgene_25395	Mouse <i>Smo</i> cDNA with C-terminal EGFP fusion.
Recombinant DNA reagent	pcDNA 6.2C-EmGFP-TOPO/Wdr35 (plasmid)	(Mill et al. 2011)		Mouse <i>Ift121</i> cDNA with a C-terminal EmGFP fusion.
Recombinant DNA reagent	pACEBac1-CMV-His-eGFP-TEV-IFT43_pIDC-CMV-IFT121_pIDK-CMV-IFT139 (plasmid)	This paper		His-eGFP version of Cr_IFT-A noncore trimer construct for expression in mammalian cells
Recombinant DNA reagent	pFL-His-TEV-IFT43 (plasmid)	This paper		His-tagged version of Cr_IFT-43 construct for the expression in insect cells
Recombinant DNA reagent	pFL-His-TEV-IFT43_IFT121 (plasmid)	This paper		His-tagged version of Cr_IFT43/121 dimer construct for the expression in insect cells
Recombinant DNA reagent	pFL-IFT139 (plasmid)	This paper		Untagged version of Cr_IFT139 construct for the expression in insect cells
Other	SNAP-Cell® TMR-Star	New England BioLabs	S9105S	1:1500
Other	SiR-tubulin kit	Spirochrome	SC002	200 nmol
Other	Hoechst 344442	Thermo Fischer Scientific	H1399	

Other	POPC Liposomes	T&T Scientific Corp.		Liposomes of POPC at 2mg/ml with a size of 50 nm
Other	PE/PG/PA Liposomes	T&T Scientific Corp.		Liposomes of DOPE, DPPG and DSPA at 2mg/ml (total lipid) with a size of 50 nm
Other	Membrane Lipid Strips	Echelon Biosciences	P-6002	
Software, algorithm	LAS AF 3.0	Leica Microsystems(Schindelin et al. 2012)		
Software, algorithm	Fiji	(Schindelin et al. 2012)	PMID: 22743772	
Software, algorithm	Imaris V9.5	Oxford Instruments		
Software, algorithm	Fiji Macro for quantification of PCM1	(RadialIntensityFromCentrosomes.ijm)	https://github.com/IGMM-ImagingFacility/Quidwai2020_WDR35paper)	
Software, algorithm	Fiji Macro for quantification of clathrin	(3DMeanIntensityfromUserDirectedPoints.ijm)	https://github.com/IGMM-ImagingFacility/Quidwai2020_WDR35paper)	
Software, algorithm	IMSD PMID:8742726	(Kremer et al., 1996)	PMID:8742726	
Software, algorithm	SerialEM	(Mastronarde 2005)	PMID: 16182563	
Software, algorithm	SWISS-MODEL	(Waterhouse et al. 2018)	PMID: 29788355	
Software, algorithm	HHBlits	(Remmert et al. 2011)	PMID: 22198341	

Software, algorithm	Prism8	GraphPad		
Software, algorithm	MaxQuant	(Cox and Mann 2008)	PMID: 19029910	

2
3
4

5 Bibliography

- 6
- 7 Caparrós-Martín, J.A., De Luca, A., Cartault, F., et al. 2015. Specific variants in WDR35 cause a distinctive form
8 of Ellis-van Creveld syndrome by disrupting the recruitment of the EvC complex and SMO into the cilium.
9 *Human Molecular Genetics* 24(14), pp. 4126–4137.
- 10 Cox, J. and Mann, M. 2008. MaxQuant enables high peptide identification rates, individualized p.p.b.-range
11 mass accuracies and proteome-wide protein quantification. *Nature Biotechnology* 26(12), pp. 1367–1372.
- 12 Diggle, C.P., Moore, D.J., Mali, G., et al. 2014. HEATR2 plays a conserved role in assembly of the ciliary motile
13 apparatus. *PLoS Genetics* 10(9), p. e1004577.
- 14 Hori, Y., Kobayashi, T., Kikko, Y., Kontani, K. and Katada, T. 2008. Domain architecture of the atypical Arf-family
15 GTPase Arl13b involved in cilia formation. *Biochemical and Biophysical Research Communications* 373(1), pp.
16 119–124.
- 17 Mastronarde, D.N. 2005. Automated electron microscope tomography using robust prediction of specimen
18 movements. *Journal of Structural Biology* 152(1), pp. 36–51.
- 19 Mill, P., Lockhart, P.J., Fitzpatrick, E., et al. 2011. Human and mouse mutations in WDR35 cause short-rib
20 polydactyly syndromes due to abnormal ciliogenesis. *American Journal of Human Genetics* 88(4), pp. 508–515.
- 21 Qin, J., Lin, Y., Norman, R.X., Ko, H.W. and Eggenschwiler, J.T. 2011. Intraflagellar transport protein 122
22 antagonizes Sonic Hedgehog signaling and controls ciliary localization of pathway components. *Proceedings of
23 the National Academy of Sciences of the United States of America* 108(4), pp. 1456–1461.
- 24 Remmert, M., Biegert, A., Hauser, A. and Söding, J. 2011. HHblits: lightning-fast iterative protein sequence
25 searching by HMM-HMM alignment. *Nature Methods* 9(2), pp. 173–175.
- 26 Schindelin, J., Arganda-Carreras, I., Frise, E., et al. 2012. Fiji: an open-source platform for biological-image
27 analysis. *Nature Methods* 9(7), pp. 676–682.
- 28 Waterhouse, A., Bertoni, M., Bienert, S., et al. 2018. SWISS-MODEL: homology modelling of protein structures
29 and complexes. *Nucleic Acids Research* 46(W1), pp. W296–W303.
- 30 Williams, C.L., McIntyre, J.C., Norris, S.R., et al. 2014. Direct evidence for BBSome-associated intraflagellar
31 transport reveals distinct properties of native mammalian cilia. *Nature Communications* 5, p. 5813.
- 32